Control of Chemical Dynamics by IR and UV Laser Pulses

Thesis submitted in partial fulfilment
of the requirements for the degree of

Doctor of Philosophy

by

KRISHNA REDDY NANDIPATI
Reg. No. 11CHPH14
nkrishna88@gmail.com

School of Chemistry
University of Hyderabad
Hyderabad - 500 046, INDIA
August 2017

DECLARATION OF AUTHORSHIP

I, Krishna Reddy Nandipati, declare that the thesis proposal, titled "Control of Chemical Dynamics by IR and UV Laser pulses" and work presented in it are my own. I hereby confirm that this work was mainly done while in candidature for a research degree at this university.

Date	Signature of the candidate

School of Chemistry
University of Hyderabad
Hyderabad-500 046
India

CERTIFICATE

It is certified that the work contained in this thesis, titled "**Control of Chemical Dynamics by IR and UV Laser Pulses**" by **Krishna Reddy Nandipati (Reg.No. 11CHPH14)**, has been carried out under my supervision and is not submitted elsewhere for a degree.

This thesis is free from plagiarism and has not been submitted previously in part or in full to this or any other University or Institution for award of any degree or diploma.

Parts of this thesis have been published in the following publications:

1. K R Nandipati* and K A Kumar, Pramana-J Phys, **87**, 50 (2016), **Chap. 3**.
2. K R Nandipati, H Singh, S Nagaprasad Reddy, K A Kumar and S Mahapatra*, Eur. Phys. J. D **68**, 355 (2014), **Chap. 4**.
3. K R Nandipati, K A Kumar, Z Lan, H Singh and S Mahapatra*, Eur. Phys. J. D (In press), **Chap. 6**.
4. K R Nandipati, Z Lan, H singh and S Mahapatra*, J. Chem. Phys. **146**, 214304 (2017), **Chap. 7**.

and presented in following conferences :

1. ICTS-School on Frontiers in Light-Matter interactions (ICTSLMI-2014), 08-18 December, 2014, at Indian Association for the Cultivation of Science, Kolkata, India (International).
2. The First Indo-Taiwan Symposium on Recent Trends in Chemical Sciences (RTCS-2014), 17-18 November, 2014, at University of Hyderabad, Hyderabad, India (International).

3. Current Trends in Computational Natural Sciences (CTCNS-2016), 20 March, 2016, at International Institute of Information Technology, Hyderabad (National).

4. A Tributary Symposium on 100 Years of Chemical Bonding-2016, 4-5 August, 2016, at CSIR-Indian Institute of Chemical Technology, Hyderabad (National).

5. 15^{th} Indian Theoretical Chemistry Symposium (TCS-2016), 14-17 December, 2016, at University of Hyderabad, Hyderabad (National).

Further, the student has passed the following courses towards fulfilment of coursework requirement for Ph.D.

Course code	Name	Credits	Pass/Fail
1. CY-801	Research Proposal	3	Pass
2. CY-806	Instrumental Methods	3	Pass
3. PY-401	Mathematical Methods-I	3	Pass
4. PY-501	Quantum Mechanics-II	3	Pass

_____ _____

Date Advisor: Prof. Susanta Mahapatra

_____

Dean
School of Chemistry
University of Hyderabad

Acknowledgements

It is with immense pleasure and contentment that I take this platform to express the deep sense of gratitude to my Ph.D. supervisor Prof. Susantha Mahapatra for his constant encouragement, inspiration and timely guidance. I am indebted to him for the values he taught me in approaching a research problem and the work freedom which he has given me, which made me stronger and more independent. Of course not to mention the morning/evening walks with him that were cherished throughout.

At the same time, it is my responsibility and joy to equally thank Prof. Harjinder Singh, IIIT Hyderabad, who introduced me to the optimal control theory and its wide scope of applications. His great hospitality made me feel IIIT-H as my home instituition whenever I visited. Of late, it was my privilege to have been introduced to Prof. Zhengang Lan, Qingdao Institute of Bioenergy and Bioprocess Technology and his viewpoints, which taught me many significant details of photodissociation involving coupled electronic surfaces. These teachers have taught me not only how to approach a scientific problem, but also how to tackle it through hard work and sincere effort. Of course, I think it would be so unfair if I do not mention the friendly discussions and interrogations that I had with both my mentors which I treasure a lot, for that has given me strength and lot of life lessons to nurture throughout.

I thank the present and former Deans, School of Chemistry for their support and encouragement in creating a wonderful work environment throughout the years. I am equally grateful to the faculties of our department who have taught me and helped me at various stages of my M. Sc. and doctoral days. My DC members Prof M. Durgaprasad and Prof. T. P. Radhakrishnan are indeed my role-models and have inspired me in learning and appreciating the basic science. Teachers like Prof. A. K. Kapoor and Prof. S. Duttagupta, School of Physics and Prof. V. Balakrishnan, IIT-M were a great help in understanding and appreciating

the language that describes microscopic world, i.e., quantum mechanics in its full glory. I wouldnt have loved the field of research and kept going persistently without these great teachers. I am grateful to all the non-teaching staff, specially Durgesh and Chittibabu, for their help.

I am thankful to my labmates Suvendu, Sugata, Arun, Rudra, Abhishek, Sitansh Sharma, Arpita, Jayakrushna, Daradhi, Nikhil, Nitai, Dr. Karunamoy, Dr. Sundarayya, Dr. Satyendra Gupta, Dr. Rajagopala Reddy, Dr. Nagaprasad Reddy, Dr. Rajagopala Rao and Dr. Tanmoy Kumar Roy for maintaining a very supportive and friendly environment to work.

Financial support from the Council of Scientific and Industrial Research (CSIR), New Dlehi, is greatly acknowledged.

Friends are a great help and consolation when we are in a crisis and going through a bad phase of life. I am privileged to have my friends Anjibabu, Mahadev, Arun, Billa, Balakonda, Srinivas, Mohan, Shiva, Surendar, Nagamaih, Anif, Divya, Lasya, Sridharanna, Subratobhayya, Sarithakka, Sashanna, and Pawananna with whom I have shared wonderful moments to cherish in my life. A special thanks to Arun for his patience throughout in terms of scientific discussions.

My family mean the primary world to me and it is beyond words to express gratitude to my Nanna, Amma, Anji and Bujja who stood by me in all times of life; be it good or bad. Whatever I have achieved so far is all their love, sacrifice and endless support.

ABSTRACT

Control of quantum dynamics in molecules at their natural timescales (femtoseconds) using light has been at the forefront of chemical physics for the past few decades. Theoretical approaches in both time (Tannor-Rice scheme) and frequency (Brumer-Shapiro scheme) domain have been developed to model and to predict the experiments involving light-molecule interaction in the effort to manipulate the molecular behaviour. Both the above schemes can be treated as special cases of a more general framework of optimal control theory (OCT). The OCT encompasses both strong and weak field limits. Therefore it has emerged as a comprehensive tool for theoretical design of control laser pulses to achieve predefined dynamical goals.

In this work, our focus is in controlling the dynamics (both adiabatic and nonadiabatic) of selected molecular systems (such as HCl, Malonaldehyde and Pyrrole) by designing and applying shaped laser pulses using a combination of OCT, time-dependent quantum mechanics and vibronic coupling (VC) theory. The so designed optimal laser pulses are analysed in detail in terms of their amplitude profile in time and frequency spectrum. The associated control mechanisms are revealed by examining thouroughly the actions of the optimal pulses. On the other hand, the time propagation of the quantum mechanical system is achieved by split-operator technique together with Fast Fourier transforms (FFT) and grid based methods. Below, we mention briefly about the control of various processes (such as state-selective population transfer, isomerization and dissociation) carried out using OCT with reliable optimal fields.

We have designed laser fields that can control the population transfer for the fundamental and overtone transitions of a vibration for the diatomic molecule, HCl. We have also examined that the effect of variation of penalty factor on the control outcomes. The optimal pulses obtained are found to be simple in time and frequency domain and are experimentally quite feasible. The optimally

controlled vibrational states can also potentially be used as qubits in quantum computing.

We have studied, within the BO approximation, a controlled initiation of isomerization reaction (H-transfer) in the electronic ground state of malonaldehyde molecule, in one dimension. The optimal initiation of H-transfer between the two oxygen atoms in malonaldehyde is achieved by the application of strong and short optimal UV-laser pulses designed using OCT based on the simplest version of Tannor-Rice optimal pump-dump scheme. This control mechanism, where we used the excited electronic potential as a mediator to initiate H-transfer from one oxygen to the other in the ground electronic state of the malonaldehyde, achieves product configuration about 90%. The role of electronic excited state, a harmonic surface, is to provide positive momentum to the Franck-Condon wavepacket by virtue of its steepness. By the momentum gained from the electronic excited state, the wavepacket after a time-delayed dumping, moves toward the product well with associated spreading and dephasing in time.

In an effort to study the control of nonadiabatic molecular dynamics (beyond BO), we have carried out H-transfer control dynamics of malonaldehyde involving coupled electronic states in two dimensions using a tuning coordinate and a coupling coordinate. The objective here is, as above, to control isomerization reaction in the ground electronic state. For this purpose, we have designed optimal UV-laser pulse using OCT for maximizing the product isomer by its continuous effective pump followed by dump operation between the electronic states while there is nonadiabatic interaction between the excited states. The control mechanism operating here is quite different from the simple pump-dump scheme explored in one dimesnional case. But the idea of using excited electronic states as mediators to control isomerization in ground state remains same. Using the designed optimal pulse we have successfully achieved a

product isomer about 45% in this nonadiabatic scenario.

We have also studied the photodissociation dynamics of pyrrole occuring on a coupled electronic states in the presence of laser pulses in an effort to control it. In this respect, at first, we have performed the initial vibrational state dependent photodissociation dynamics of pyrrole, in the presence of UV-laser pulses (by OCT), via $^1\pi\sigma^*$ ($^1A_2$)/ S_0 conical Intersection (CI). The optimal laser pulses for effective photodissociation for various initial vibrational states of the system are designed and the associated control mechanism(s) is examined. This leads to mode-specific control of the photodissociation driven by $^1\pi\sigma^*$ state. Later, we have investigated an alternative route of $^1\pi\sigma^*$-photodissociation of pyrrole as compared to the conventional barrier crossing mechanism, with the aid of an optimally probe pulse, was suggested. This path opens up electronic transitions, under the influence of a continuous action of pump-dump laser pulse, efficiently populating both the upper and lower adiabatic dissociation channels. The control mechanism suggested is found out be robust. Excellent control outcomes are obtained in both the cases. Given the high experimental relevance of $^1\pi\sigma^*$-photochemistry in the recent past, the simple optimal pulses obtained by the use of genetic algorithm (GA) based optimization worth an experimental implementation.

List of Abbreviations

BS	Brumer-Shapiro
BO	Born-Oppenheimer
CDA	Constant Dipole Approximation
CI	Conical Intersection
CG	Conjugate Gradient
DFT	Discrete Fourier Transform
DVR	Discrete Variable Representation
FC	Franck-Condon
FFT	Fast Fourier Transform
FGH	Fourier Grid Hamiltonian
GA	Genetic Algorithm
GP	Geometric Phase
HT	Hydrogen Transfer
IVR	Intramolecular Vibrational Redistribution/Relaxation
KE	Kinetic Energy
OCT	Optimal Control Theory
PES	Potential Energy Surface
PE	Potential Energy
RHS	Right Hand Side
SO	Split Operator
STIRAP	Stimulated Raman Adiabatic Passage
TDM	Transition Dipole Moment
TDSE	Time-Dependent Schrödinger Equation
TISE	Time-Independent Schrödinger Equation
TDWP	Time-Dependent Wavepacket Propagation
TMF	Transition Moment Function
TRK	Tannor, Rice and Kosloff
VC	Vibronic Coupling
WP	Wavepacket

Contents

List of Figures

List of Tables

Chapter 1

Introduction

Chemistry involves study of structure and dynamics of atoms and molecules and their reactions. The latter involve breaking and making of chemical bonds on a femtosecond (10^{-15} sec) time scale. Often, it is possible to have multiple end-products from a reactant(s) in a reaction. Therefore it becomes the central theme of chemistry to find ways to control the selection of products of a chemical reaction. The traditional control methods involve exploitation of incoherent collisions between reactant molecules. This so-called macroscopic control, wherein parameters like the temperature and pressure are control knobs, is not adequately satisfying. This is because the energy supplied gets statistically distributed over many internal degrees of freedom of reactant molecules at the reaction time scale. In such strategies, the experimenter has no control over the molecular evolution once the reaction is initiated. Typically, a lot of energy is wasted and unwanted by-products are produced. Therefore, there is a great need to find efficient control strategies for regulating the energy flow with time in order to perform a selective and clean chemistry. In this regard, laser appears to be a promising tool for controlling chemical reactions.

1.1 Control using lasers

Ever since the invention of laser in 1960, chemists have explored the unique properties of laser radiation viz., monochromaticity, high intensity and phase coherence in order to perform selective, clean and energetically efficient photochemistry [1, 2]. The laser radiation can deposit the energy in a molecule in a very nonstatistical fashion. Moreover, the parameters regulating its unique properties can be completely and actively controlled. Therefore the laser light can be used as an effective tool to steer the molecular system that it interacts with, to a desired quantum state or physical configuration. The initial attempts to control bond selective chemistry [4–8] were mainly based either on small spectral bandwidth or on short duration and high intensity of the laser pulses. In the former case the underlying concept is to avoid generating different products by localizing the energy, on the reaction time scales, in a smaller number of rovibrational modes of a reactant molecules that span the spectrum; and in the latter case it is the excitation of a high overtone of a particular vibration (to break the bond associated with it) in a short time. The underlying assumption on which these approaches are based is that the rate of bond breakage in a given time duration increases and it circumvents the rate of intramolecular vibrational redistribution (IVR) [9, 10]. Except in a very few simple systems [11–14], both these methods fail. The main cause of the failure is attributed to the preassumption that a specific reaction pathway is associated with a particular degree of freedom, without accounting for the influence and effects of radiation on the rest of the molecular degrees of freedom which can also undergo simultaneous excitation [15–18]. Therefore, for a successful control over the product selectivity one need not focus on the time dependence of IVR with a local mode (i.e., single bond) excitation. Since the local mode is not an eigenstate of the system hamiltonian and is strongly coupled to other bonds, the excitation of this mode produces a highly diffused wavepacket (WP) indicating excitation of many bonds,

leading to IVR.

An alternative approach of controlling chemical reactions relies completely on quantum mechanical interference effects between all possible paths that connect reactants and products on a potential energy surface(s) (PES). This idea is based upon the path integral formulation of quantum mechanics. An interaction with a laser pulse can generate multiple quantum paths by exciting to a number of intermediate states of the system between initial reactant and final product states. These intermediate states that span the frequency spectrum of the pulse define the dynamical pathways that connect the reactants and products. Simply, this can be understood in terms of coherent WP picture. As shown in Fig. 1.1, for instance an ultrashort laser pulse excites a diatomic molecule to an electronically excited state preparing a WP which is a coherent superposition of eigenstates of the electronic ground state promoted to the excited state. In doing so the laser pulse imprints both its magnitude and phase information onto the individual eigenstates evolving on the excited state. Thereby the amplitude associated with each state (or a dynamical path corresponding to it) can interfere either constructively or destructively that leads to an enhancement or a suppression of a particular product formation, respectively. This enables the manipulation of the quantum interference between the amplitudes associated with various paths so that the desired target product is achieved, by actively tuning the laser pulse parameters. This is a more natural way of full utilization of properties of the eigenstates and complete PES(s) of the molecular system. In this way one can avoid associating a specific reaction pathway to a particular degree of freedom, the main presumption in the mode selective chemistry [1, 9, 10]. The advances in laser technology [19, 20, 22–25, 131] and their use in spectroscopy [26–29] have provided good knowledge of the molecular electronic, vibrational and rotational dynamics at their natural time scales [31–36]. The key advance in this regard is tailoring the ultrashort laser pulses and their application for manipulating the ultrafast

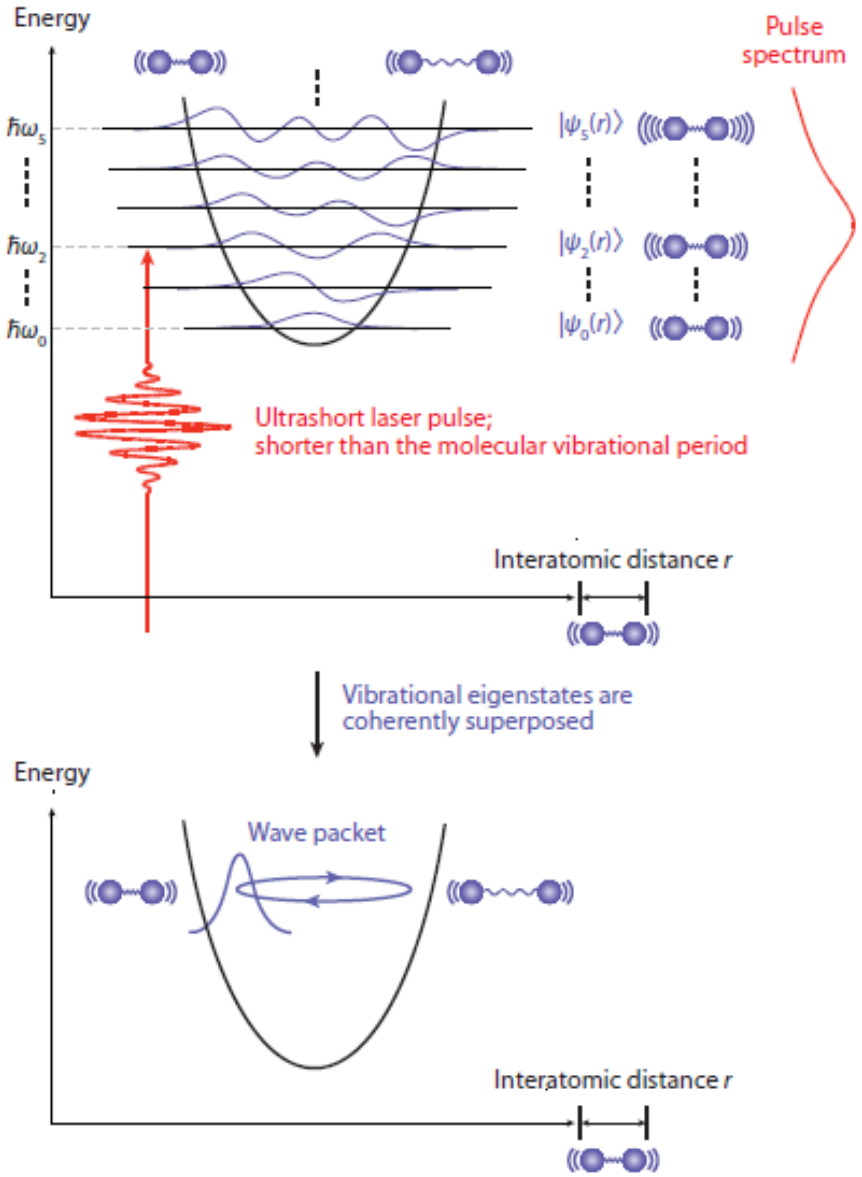

Figure 1.1: Schematic representation of the generation of an electronically excited coherent vibrational WP subjecting a diatomic molecule to an ultrashort laser pulse. If the pulse duration is shorter compared to the vibrational period of the molecule, its bandwidth is broad enough to superpose multiple vibrational eigenstates. The superposed eigenstates undergo interference with each other for creating a spatially localized wavefunction referred to as a WP. [K. Ohmori, Ann. Rev. Phys. Chem. **60**, 487 (2009)].

molecular processes mentioned above. In the recent past, the control of molecular dynamics via shaped laser pulses has seen promising developments in terms of successful experimental implementation of theoretical concepts [9, 10, 37–42]. Theoretically, the question of finding the best (optimal) shape of laser pulse or pulse sequences for successfully carrying out controlled molecular dynamics, is developed within the mathematical formalism of optimal control theory (OCT). In the next section, we briefly describe various strategies developed that rely on quantum mechanical interference effects for controlling molecular dynamics. Then we introduce the general methodology that encompasses all those quantum control strategies as special cases, the OCT.

1.2 Theoretical developments in quantum control

The quantum control strategies considered here differ fundamentally from both the traditional methods of controlling product formation used in synthetic chemistry and, the initial attempts of controlling bond-selective chemistry exploiting the intensity and/or frequency resolution offered by the laser technology. The common central theme of these quantum control approaches involve exploitation of light-controlled quantum interferences to manipulate the dynamics in molecules [43]. Hence they are also referred to as "coherent control" techniques. Below we present the overview of such techniques.

1.2.1 Single parameter control schemes

In the 1980s, two approaches were proposed to create and manipulate coherences for achieving control in molecules by utilizing coherent properties of laser light, one in the time domain, by Tannor, Rice and Kosloff (TRK) [44, 45] and the other in frequency domain, by Brumer and Shapiro (BS) [46–49]. The former scheme, in its simplest version, utilizes ultrashort light pulses to prepare coherent WP from

molecular eigenstates. A pump pulse prepares the coherent vibrational WP on an electronically excited potential energy surface (PES). The WP is then allowed to evolve freely on the excited PES during which several nuclear configurations of the molecule are screened [50]. After a free evolution, a suitable dump pulse de-excites the system to the desired channel in the ground PES. This pump-dump approach is represented schematically in Fig. 1.2(a). By tuning the time delay between the pump and dump pulses and their amplitudes one can achieve control over product formation. On the other hand, the BS scheme utilizes the interference between independent pathways of excitation by light between the same initial and final state of the molecule [51–53] [cf., Fig. 1.2(b)]. In this scheme, two coherent light sources of frequencies ω_m and ω_n are used to prepare a superposition of continuum eigenstates correlating asymptotically to different sets of products. The excitation of reactants follows absorption of 'n' photons of the first color and 'm' photons of the second, such that $n\omega_m = m\omega_n$. The interference associated with these two excitation pathways is modulated mainly by tuning the relative phase of two light sources. It is the wavefunctions produced by the light waves that strongly interfere and not the light waves themselves as they have very different amplitudes and wavelengths. But by tuning the phase and amplitude of light sources one can alter the product distribution.

Both these methodologies involve varying a single parameter as a control knob e.g., the parameters "time delay (Δt)" in TRK scheme and the "relative phase ($\Delta\phi$)" in BS scheme, between the light fields are controllers. The experimental implementation of both these schemes have been applied successfully in controlling a number of molecular phenomena such as control of selective population transfer [54–57] and photochemical reactions [58–73] and etc. However, there exist limitations to the practical applicability of these schemes. The TRK scheme is limited due to the usage of transform limited laser pulses having frequency independent spectral phase. Whereas, among other

technical problems, the limitation of BS scheme lies in the practical difficulty of simultaneous excitation of two reaction pathways and the problem of locking of phase and amplitude of light fields in optically dense media [74].

Apart from the above mentioned control schemes, there exists another robust control scheme for complete population transfer in a Λ type system (wherein the energy level structure follows a shape of Greek letter Λ), known as stimulated Raman adiabatic passage (STIRAP) [75–78], proposed by Bergmann and co-workers. In STIRAP the population transfer is achieved adiabatically to final state from initial state with negligible intermediate state population in a Λ system by applying two time-delayed counterintuitive strong pulses. The two pulses are referred to as pump pulse and Stokes pulse. The former connects the initial and intermediate states while the latter couples the intermediate and final states (Fig. 1.2(c)). Not only does Stokes pulse precede pump pulse with extremely stable relative phase between them, they also should overlap partially for the STIRAP scheme to work for complete population transfer. As in TRK control scheme, the time-delay (Δt) between the pump and Stokes pulse acts as a controller to keep the transient population in the intermediate state almost zero. Under this circumstance, losses due to radiative decay can be avoided. This method also exploits the quantum mechanical interference between excitation pathways created by pump and Stokes pulse. Successful demonstrations of STIRAP include applications for small molecules [78–80]. In large polyatomic molecules the adiabatic passage is challenging because of increase in density of states [78, 81]. All the control approaches discussed above are based on tuning the single parameter of a laser field, and can be effective for small systems. However, due to the complexity in the PESs of polyatomic molecules, these methods may have to be revised. Therefore it is useful to have a pulse shaping approach which is more flexible, robust and that can provide optimally designed laser fields to achieve control over dynamics involving specific bonds of a molecular system.

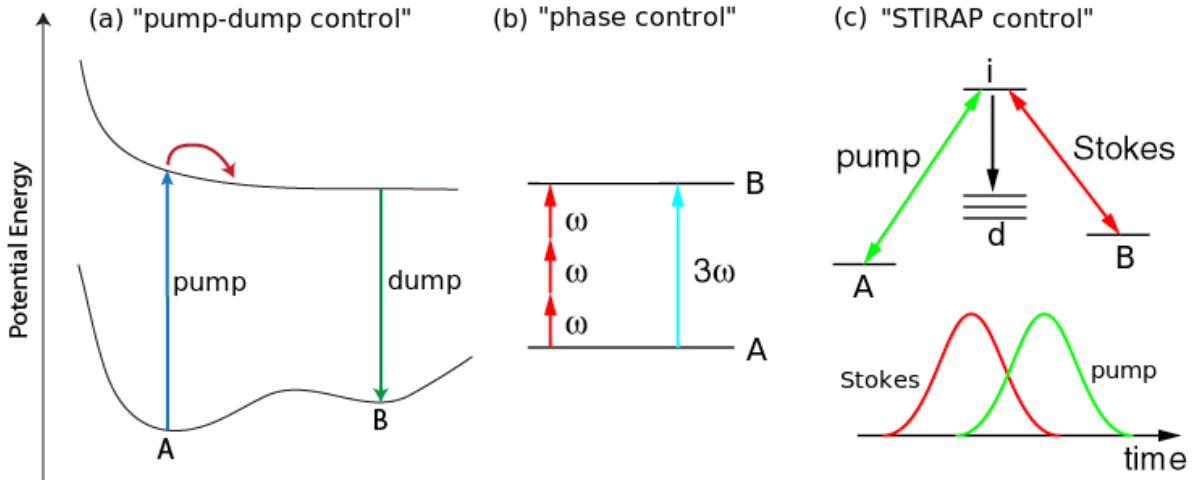

Figure 1.2: Schematic representation of single parameter quantum control schemes: (a) The TRK pump-dump scheme. (b) The BS phase control scheme. (c) The STIRAP control scheme. 'A' is the initial state; 'B' is the desired target state; 'i' is the intermediate state; 'd' refers to the decay states [T. Brixner and G. Gerber, Chem. Phys. Chem. **4**, 418 (2003)].

Below we present one such method, namely the optimal control theory, that exhibits control over system dynamics taking multiple parameters of a laser pulse into account.

1.2.2 Optimal control theory and its experimental implementation

In the context of coherent control of product formation using a laser pulse, the TRK pump-dump scheme suggests an easy implementation to achieve control. It is necessary to have a WP evolving on the excited state PES be sufficiently compact (coherent), over the product channel on the ground state PES, so that a large fraction of it can be dumped to generate that specific product by a time-delayed dump pulse. Typically, the WP spreads and gives rise to a very complicated distribution of amplitude on excited surface. Hence, a simple dump pulse may not be efficient to transfer population to the product channel on the

the ground state surface. This has led to the quest for a pulse of temporally and spectrally shaped field that can continuously transfer WP amplitude back and forth between the two electronic states as WPs move on these surfaces so that maximum yield of the product is achieved. The question of finding the optimal pulse shape is addressed using calculus of variations, as proposed by Tannor and Rice [44, 82]. The application of variational calculus to design optimal pulses was further extended by Rabitz *et al.* [83–86], and others [87, 88].

1.2.2.1 Optimal control theory

The mathematical framework of optimal control theory (OCT) provides the prescription for calculating the best (optimal) shape of a pulse. The theory relies on the application of variational calculus to problems involving differential equation as a constraint. In the case of quantum systems, such a constraint is the time-dependent Schrödinger equation (TDSE) describing the dynamics in the presence of a control field interacting with its permanent and/or transition dipole moment (TDM). The application of general principles of control theory to microscopic equations of motion in the form of OCT is conceptually novel with potential applications in technology. In this scheme, one seeks the best solution to a given problem under stated goals, circumstances, and/or other system constraints (the formal considerations are given in Chapter 2).

In OCT, a "cost functional" of an electric field, $\epsilon(t)$, is constructed that typically involves an objective term and some constraint terms. The objective term is a measure of degree to which the desired target is reached under a driving laser field, $\epsilon(t)$. The constraint terms typically include imposition of penalty on the norm of the electric field of the laser pulse and ensuring that the quantum system follows the dynamical equation of motion (i.e., Schrödinger equation). Applying variational calculus, one tries to find an extremum of the objective functional with respect to all the independent variables leading to a set of equations to design a field, $\epsilon(t)$. Numerically, these equations are solved

iteratively to find the optimal laser field that achieves desired target state at the final time $t = T$ from an initial state at time $t = 0$, successfully. In order to solve this variational problem, the TDSE for evolution of the system is employed in combination with an optimization algorithm.

In the recent past, OCT has emerged as a promising tool for theoretical design of pulses for controlling molecular motion. Within the framework of OCT both the strong and weak field limits can be treated. OCT allows the optimization of multiple parameters of laser pulse such as amplitude, frequency and phases, simultaneously. Therefore, the single parameter control schemes mentioned above such as TRK and BS can be subsumed as special cases in the general OCT methodology. The OCT uses effects of interference that arise out of excitation of different quantum pathways by optimized laser field, to efficiently achieve the desired molecular dynamics. The technique has been successfully applied in the manipulation of variety of molecular processes such as state selective population transfer [89–95], orientation and alignment control of molecules [96, 97], isomerization control [98–102], control of electron currents in aromatic rings [103, 104], controlled separation of isotopes [105], and design of quantum logic gates [106–111], etc.

1.2.2.2 Optimal control experiments

The direct implementation of optimal laser pulses designed by OCT suffers from a number of problems when tested in the laboratory, the foremost reason being the use of approximate Hamiltonian in computations. Except for the smallest molecules, one inevitably uses approximations for the Hamiltonian to circumvent formidable task of computations in multiple dimensions. Second, the laser pulses are associated with certain amount of noise, as well as uncertainty in phase and amplitude, leading to failure of control. Finally, the effects due to neglect of additional PESs, spin-orbit coupling, finite temperature and so forth in model calculation can also lead to the failure of computed optimal pulse to

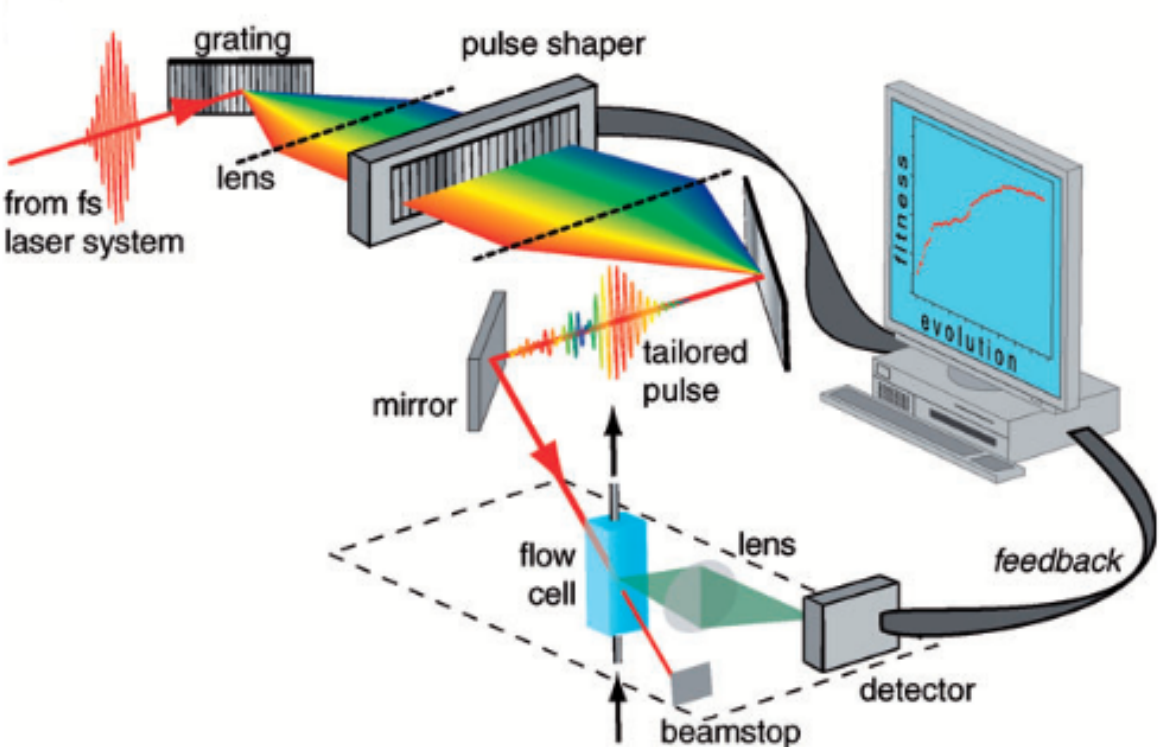

Figure 1.3: Schematic representation of the experimental adaptive feedback control for teaching lasers to achieve optimal control over the quantum system. [G. Gerber *et al.*, Phys. Chem. Chem. Phys., **9**, 2470 (2007)].

perform when applied to real molecules. Given the problems associated with experimental implementation, it is desirable to devise a control scheme that circumvents them. Rabitz and coworkers have suggested the use of "feedback" or "adaptive" control strategies in a "closed loop" [112] experiment. The idea behind these experiments is as follows. To start with, the molecule in interaction with laser pulse evolves with its own Schrödinger equation which naturally includes all PESs, laser uncertainties, propagation effects in thick samples and so on. An input-output feedback loop is then set up in such a way that a given input produces a certain output, which is fed back into a computer. The merit of the input is evaluated based on the degree to which a desired target is reached. Based on the merit, the input is then modified in the next cycle. The schematic

diagram showing the closed loop control experiment is presented in Fig. 1.3. An initial guess laser field through a pulse shaper is applied to the molecular system of interest. The resulting signal (for example in the experiment referred to in Fig. 1.3, the fluorescence emission of a solvated molecule) is detected. These results are then transferred to a computer which has a learning algorithm (e.g., genetic algorithm, GA) running in order to find an improved laser pulse shape. Employing this control pulse the cycle of events is repeated to find improved shape of the pulse for the next iteration. The cycle of events is carried out iteratively, with the help of algorithm to modify the field further until the desired objective is satisfactorily achieved. In the closed loop feedback control the new field in each iteration requires action on a new molecular sample prepared identically to the original system. Hence this strategy is also called as "adaptive feedback control (AFC)".

The AFC has been used successfully for controlling a number of molecular processes since its first realization as an experimental quantum control tool [113]. The control processes for example include tuning the fluorescence, chemical branching ratios and energy transfer in a light harvesting complex. The advantage of AFC in experiments is two fold a) no knowledge of the Hamiltonian, PESs of the system and the reaction mechanism needed a priori, and b) it is extremely fast and robust. The AFC technique is used by Gerber *et al.* in a landmark set of experiments for controlling photodissociation of $CpFe(CO)_2Cl$ to CpFeCOCl vs FeCl [114]. Later, several groups demonstrated AFC as an effective experimental tool in controlling various chemical, physical and biological processes [115–134].

Given the remarkable success of AFC experiments in teaching laser pulses to achieve best control over quantum systems, it is natural to think about the relevance and necessity of theoretical design of control pulses in reality. The theoretically calculated pulses (even with an approximate Hamiltonian and ignoring noise and system-environment effects, etc.) not only help us to provide

insights of the nature of molecular dynamics and the principles governing the control mechanism, they also act as excellent initial guess fields for AFC. A control field calculated *ab initio* can provide a preliminary idea about the feasibility of achieving control in a particular system, without doing the expensive full scale experiment. Moreover, the above mentioned theoretical approaches and experimental implementations as testing tools pave a way for understanding complex molecular dynamics with further hand in hand developments in both fronts.

1.3 Plan of work

The present work is about designing optimal laser pulses and examining the associated mechanisms for controlling state selective population transfer, isomerization and photodissociation involving electronic ground states as well as electronic excited states. The control dynamics studied here include both within the Born-Oppenheimer (BO) approximation (adiabatic) and beyond BO (nonadiabatic) [1]. The molecular systems of interest considered in this work for the control tasks range from simple diatomic to relatively complex polyatomic molecules. The dynamics of the molecular system during its control is treated with time-dependent Schrödinger equation (TDSE) within the semiclassical dipole approximation [86, 92]. This dynamical evolution taken as a constraint is combined with the numerical pulse shaping technique, OCT. Moreover, the treatment of nonadiabatic quantum dynamics is done using a diabatic representation. Split-operator technique together with fast Fourier transform (FFT) is used for time propagation of laser-driven quantum mechanical system. The theoretical methods used in the present studies are discussed in **Chap. 2**.

In quantum computing the use of quantum states as qubits [135] is inevitable. This suggests the importance of preparation of coherent quantum states, for instance using laser pulses. We have designed infrared laser pulses using

OCT in combination with conjugate gradient method. The optimal pulses are designed to perform coherent excitation that lead to selective population transfer between vibrational states of the diatomic molecule, HCl. Specifically, the control of fundamental and overtone transitions of a vibration are considered. We also examined the effect of variation of penalty factor on the control outcomes. The optimal pulses obtained are found to be simple in time and frequency domain and are highly experimentally feasible. The optimally controlled vibrational states could be used as qubits and the pulses as logic gates. Moreover, the insights of the control studies of HCl are useful as it acts as a prototype for other halides that participate in H-abstraction reactions which are plenty, in chemistry. The results of these control studies are presented and discussed in detail in **Chap. 3**.

We have applied OCT for controlling chemical reactions that occur in electronic ground state with the aid of excited states as mediators. The idea behind involving excited states is to surmount any barrier obstructing the desired reaction from occurring in the ground state. This can be achieved using pumping and a time-delayed dumping between the two electronic states. Within the BO approximation, a controlled initiation of isomerization reaction (H-transfer, HT) in the electronic ground state of malonaldehyde molecule is considered for the study. The optimal initiation of HT between the two oxygen atoms in malonaldehyde is achieved by the application of strong and short optimal UV-laser pulses designed using OCT based on the simplest version of TRK optimal pump-dump scheme. This control mechanism, where we used the excited electronic potential as a mediator to initiate H-transfer from one oxygen to the other in the ground electronic state of the malonaldehyde, achieves product configuration of 90%. The role of electronic excited state, a harmonic surface, is to provide positive momentum to the Franck-Condon WP by virtue of its steepness. By the momentum gained from the electronic excited state, the WP after a time-delayed dumping, moves toward the product well with associated spreading

and dephasing in time. A comparative account of the dynamical outcomes using the Condon approximation for the transition dipole moment and using a more realistic value calculated *ab initio* are investigated and a good agreement is found between the two. These results are discussed in detail in **Chap. 4**.

In an effort to study the control of nonadiabatic molecular dynamics (beyond BO), we have also applied OCT with GA optimization to design optimal UV-laser pulses for controlling H-transfer of malonaldehyde involving coupled electronic states in two dimensions (involving a tuning coordinate and a coupling coordinate). The objective here is, as above, to control isomerization reaction in the ground electronic state. For this purpose, we have designed optimal UV-laser pulse using OCT for maximizing the product isomer by its continuous effective pump followed by dump operation between the electronic states while there is nonadiabatic interaction due to the conical intersection (CI) between the excited states. The control mechanism operating here is quite different from the simple pump-dump scheme explored in one dimensional case. But the idea of using excited electronic states as mediators to control isomerization in ground state remains same. Using the designed optimal pulse we have successfully achieved a product isomer about 45% in this nonadiabatic scenario. These results are discussed in detail in **Chap. 5**.

Another nonadiabatic control dynamics that we have studied is the phothodissociation of pyrrole on coupled S_0 and $^1\pi\sigma^*$ ($^1A_2$) electronic states. We have applied OCT to design optimal UV-laser pulses for to bring about effective photodissociation (N-H dissociation). Specifically, the initial vibrational state dependent photodissociation dynamics of pyrrole in the presence of UV-laser pulses is studied. The variation in the branching ratio between the two asymptotic channels for various initial conditions of the system is observed implicitly. The associated control mechanism(s) is examined. This leads to mode-specific control of the photodissociation on $^1\pi\sigma^*$ state. These results are discussed in detail in

Chap. 6.

Having observed the mode-specific mechanism of photodissociation on $^1\pi\sigma^*$ state, we have investigated an alternative mechanistic route for the same with the aid of a control pulse. For this, we have performed a first principles quantum dynamics study of N-H photodissociation of pyrrole on the S_0 and $^1\pi\sigma^*$ ($^1A_2$) coupled electronic states with optimally designed UV-laser probe pulse. A new route of photodissociation of pyrrole as compared to conventional barrier crossing mechanism, based on electronically coupled states was suggested. This path opens up electronic transitions, under the influence of a continuous action of pump-dump laser pulse, efficiently populating both the upper and lower adiabatic dissociation channels. These results are discussed in detail in **Chap. 7**.

Finally, in **Chap. 8** we summarize our findings and discuss the future directions of our research.

Bibliography

[1] D. J. Tannor, *Introduction to Quantum Mechanics : A Time-Dependent Perspective*,University Science Books, USA (2007).

[2] R. J. Gordon and S. A. Rice, Annu. Rev. Phys. Chem. **48**, 601 (1997).

[3] A. H. Zewail (Ed.), *Advances in Laser Spectroscopy* I, SPIE, Bellingham (1977).

[4] V. S. Letokhov, Phys. Today **30**, 23 (1977).

[5] N. Bloembergen and A. H. Zewail, Phys. Today **31**, 23 (1978).

[6] A. H. Zewail, Phys. Today **33**, 27 (1980).

[7] F. F. Crim, Ann. Rev. Phys. Chem. **35**, 657 (1984).

[8] F. F. Crim, Ann. Rev. Phys. Chem. **44**, 397 (1993).

[9] S. Rice and M. Zhao, *Optical Control of Molecular Dynamics*, John Wiley and Sons, New York, (2000).

[10] M. Shapiro and P. Brumer, *Principles of the Quantum Control of Molecular Processes*, John Wiley and Sons, New York, (2002).

[11] T. M. Ticich, M. D. Likar, H. R. Dübal, L. J. Butler, and F. F. Crim, J. Chem. Phys. **87**, 5820 (1987).

[12] T. Arusi-Parpar, R. P. Schmid, R. J. Li, I. Bar, and S. Rosenwaks, Chem. Phys. Lett. **268**, 163 (1997).

[13] I. Bar, Y. Cohen, D. David, S. Rosenwaks, and J. J. Valentini, J. Chem. Phys. **93**, 2146 (1990).

[14] F. F. Crim, Science **249**, 1387 (1990).

[15] N. Bloembergen and A. H. Zewail, J. Phys. Chem. **88**, 5459 (1984).

[16] T. Elsaesser and W. Kaiser, Annu. Rev. Phys. Chem. **42**, 83 (1991).

[17] A. H. Zewail, J. Phys. Chem. **100**, 12701 (1996).

[18] M. Gruebele and R. Bigwood, Int. Rev. Phys. Chem. **17**, 91 (1998).

[19] A. M. Weiner, D. E. Leaird, J. S. Patel, and J. R. Wullert, Opt. Lett. **15**, 326 (1990).

[20] M. M. Wefers and K. A. Nelson, Opt. Lett. **18**, 2032 (1993).

[21] A. M. Weiner, Rev. Sci. Instrum. **71**, 1929 (2000).

[22] R. A. Kaindl, M. Wurm, K. Reimann, P. Hamm, A. M. Weiner, and M. Woerner, J. Opt. Soc. Am. B **17**, 2086 (2000).

[23] T. Brixner and G. Gerber, Opt. Lett. **26**, 557 (2001).

[24] D. Goswami, Phys. Rep. **374**, 385 (2003).

[25] C. Rulliére (Ed.), *Femtosecond Laser Pulses: Principles and Experiments (Second Edition)*, Springer, New York, (2005).

[26] A. H. Zewail (Ed.), *Photochemistry and Photobiology*, Harwood Academic, London, (1983).

[27] E. R. Menzel, *Laser Spectroscopy: Techniques and Applications*, Marcel Dekker, Inc., New York, (1995).

[28] P. Hannaford (Ed.), *Femtosecond Laser Spectroscopy*, Springer, New York, (2005).

[29] V. S. Letokhov, *Laser Control of Atoms and molecules*, Oxford University press, (2007).

[30] A. H. Zewail, Eng. Sci. **43**, 8 (1980).

[31] E. Schreiber, *Femtosecond real-time spectroscopy of small molecules and cluster*, Springer, New York, (1998).

[32] J. Manz and L. Wöste (Eds.), *Femtosecond Chemistry*, VCH Publishers, Inc., New York, (1995).

[33] P. Gaspard and I. Burghardt (Eds.), *Chemical reactions and their control on the femtosecond time scale*, Adv. Chem. Phys. **101**, Wiley, New York, (1997).

[34] V. Sundström (Ed.), *Femtochemistry and Femtobiology*, World Scientific, Singapore, (1997).

[35] A. H. Zewail, J. Phys. Chem. A **104**, 5660 (2000).

[36] S. Mukamel, *Principles of Nonliner Optics and Spectroscopy*, Oxford University Press, (1995).

[37] *Coherent control of photochemical and photobiological systems* (2006), J. Photochem. Photobiol. A, Volume 180, issue 3, pages 225-334.

[38] *Coherent control with femtosecond laser pulses* (2001), Eur. Phys. J. D, Volume 14, issue 2.

[39] A. Bandrauk, *Molecules in Laser Fields*, Nato ASI series C Mathematical and Physical Sciences, Kluwer Academic Publishers, (1995).

[40] N. P. Moore, G. M. Menkir, A. N. Markewitch, and P. G. R. J. Levis, in *Laser control and manipulation of molecules*, edited by R. J. Gordon (American Chemical Society: Washington, DC, 2001), ACS Symposium Series in Chemistry.

[41] *Focus on quantum control* (2009), New J. Phys., Volume 11, pages 105031-105053.

[42] R. Chakrabarti and H. Rabitz, Int. Rev. Phys. Chem. **26**, 671 (2007).

[43] R. J. Gordon and S. A. Rice, Ann. Rev. Phys. Chem. **48**, 601 (1997)

[44] D. J. Tannor and S. A. Rice, J. Chem. Phys. **83**, 5013 (1985).

[45] D. J. Tannor, R. Kosloff and S. A. Rice, J. Chem. Phys. **85**, 5805 (1986).

[46] P. Brumer and M. Shapiro, Chem. Phys. Lett. **126**, 541 (1986).

[47] M. Shapiro, J. W. Hepburn and P. Brumer, Chem. Phys. Lett. **149**, 451 (1988).

[48] M. Shapiro and P. Brumer, Acc. Chem. Res. **22**, 407 (1989).

[49] P. Brumer and M. Shapiro, Annu. Rev. Phys. Chem. **43**, 257 (1992).

[50] B. M. Garraway, K. -A. Suominen, Rep. Prog. Phys. **58**, 265 (1995).

[51] C. K. Chan, P. Brumer, and M. Shapiro, J. Chem. Phys. **94**, 2688 (1991).

[52] Z. Chen, P. Brumer, and M. Shapiro, J. Chem. Phys. **98**, 6843 (1993).

[53] S. Lee, J. Chem. Phys. **107**, 2734 (1997).

[54] C. Cheng, Y. Y. Yin, and D. S. Elliott, Phys. Rev. Lett. **64**, 507 (1990).

[55] S. M. Park, S. P. Lu, and R. J. Gordon, J. Chem. Phys. **94**, 8622 (1991).

[56] S. P. Lu, S. M. Park, Y. Xie, and R. J. Gordon, J. Chem. Phys. **96**, 6613 (1992).

[57] X. Wang, R. Bersohn, K. Takahashi, M. Kawasakai, and H. L. Kim, J. Chem. Phys. **105**, 2992 (1996).

[58] T. Baumert, M. Grosser, R. Thalweiser, and G. Gerber, Phys. Rev. Lett. **67**, 3753 (1991).

[59] T. Baumert, B. Bühler, M. Grosser, R. Thalweiser, V. Weiss, E. Wiedenmann, and G. Gerber, J. Phys. Chem. **95**, 8103 (1991).

[60] E. D. Potter, J. L. Herek, S. Pedersen, Q. Liu, and A. H. Zewail, Nature **355**, 66 (1992).

[61] T. Baumert and G. Gerber, Isr. J. Chem. **34**, 103 (1994).

[62] J. L. Herek, A. Materny, and A. H. Zewail, Chem. Phys. Lett. **228**, 15 (1994).

[63] T. Baumert, J. Helbing, and G. Gerber, Adv. Chem. Phys. **101**, 47 (1997).

[64] F. Gai, J. C. McDonald, and P. A. Anfinrud, J. Am. Chem. Soc. **119**, 6201 (1997).

[65] S. L. Logunov, V. V. Volkov, M. Braun, and A. M. El-Sayed, Proc. Natl. Acad. Sci. USA **98**, 8475 (2001).

[66] D. S. Larsen, M. Vengris, I. H. Van Stokkum, M. A. van der Horst, F. L. de Weerd, K. J. Hellingwerf, and R. van Grondelle, Biophys. J. **86** 2538 (2004).

[67] M. Vengris, D. S. Larsen, M. A. van der Horst, O. F. A. Larsen, K. J. Hellingwef, and R. van Grondelle, J. Phys. Chem. B **109**, 4197 (2005).

[68] D. S. Larsen and R. van Grondelle, Chem. Phys. Chem. **6**, 828 (2005).

[69] D. W. Schumacher, F. Weihe, H. G. Muller, and P. H. Bucksbaum, Phys. Rev. Lett. **73**, 1344 (1994).

[70] Y. Y. Yin, D. S. Elliott, R. Shehadeh, and R. E. Grant, Chem. Phys. Lett. **241**, 591 (1995).

[71] B. Sheehy, B. Walker, and L. F. DiMauro, Phys. Rev. Lett. **74**, 4799 (1995).

[72] V. D. Kleiman, L. Zhu, J. Allen, and R. J. Gordon, J. Chem. Phys. **103**, 10800 (1995).

[73] L. Zhu, V. D. Kleiman, X. Li, S. P. Lu, K. Trentelman, and R. J. Gordon, Science **270**, 77 (1995).

[74] C. Chen and D. S. Elliott, Phys. Rev. A **53**, 272 (1996).

[75] U. Gaubatz, P. Rudecki, M. Becker, S. Schiemann, M. Klz, and K. Bergmann, Chem. Phys. Lett. **149**,463 (1988).

[76] U. Gaubatz, P. Rudecki, S. Schiemann, and K. Bergmann, J. Chem. Phys. **92**, 92, 5363 (1990).

[77] G. W. Coulston and K. Bergmann, J. Chem. Phys. **96**, 3467 (1992).

[78] K. Bergmann, H. Theuer, and B. W. Shore, Rev. Mod. Phys. **70**, 1003 (1998).

[79] T. Halfmann and K. Bergmann, J. Chem. Phys. **104**, 7068 (1996).

[80] T. Halfmann, L. P. Yatsenko, M. Shapiro, B. W. Shore, and K. Bergmann, Phys. Rev. A **58**, 46 (1998).

[81] N. V. Vitanov, T. Halfmann, B. W. Shore, and K. Bergmann, Ann. Rev. Phys. Chem. **52**, 763 (2001).

[82] D. J. Tannor and S. A. Rice, Adv. Chem. Phys. **70**, 441 (1988).

[83] A. P. Peirce, M. A. Dahleh, and H. Rabitz, Phys. Rev. A **37**, 4950 (1988).

[84] S. Shi, A. Woody, and H. Rabitz, J. Chem. Phys. **88**, 6870 (1988).

[85] S. Shi and H. Rabitz, Chem. Phys. **139**, 185 (1989).

[86] S. Shi and H. Rabitz, J. Chem. Phys. **92**, 364 (1990).

[87] R. Kosloff, S. A. Rice, P. Gaspard, S. Tersigni, and D. J. Tannor, Chem. Phys. **139**, 201 (1989).

[88] W. Jakubetz, J. Manz, and H. J. Schreier, Chem. Phys. Lett. **165**, 100, (1990).

[89] M. V. Korolkov, Y. A. Logvin, and G. K. Paramonov, J. Phys. Chem. **100**, 8070 (1996).

[90] M. V. Korolkov, J. Manz, and G. K. Paramonov, Chem. Phys. **217**, 341 (1997).

[91] W. Zhu, J. Botina, and H. Rabitz, J. Chem. Phys. **108**, 1953 (1998).

[92] K. Sundermann and R. de Vivie-Riedle, J. Chem. Phys. **110**, 1896 (1999).

[93] T. Hornung and R. de Vivie-Riedle, Europhys. Lett. **64**, 703 (2003).

[94] G. G. Balint-Kurti, F. Manby, Q. Ren, M. Artamonov, T. S. Ho, and H. Rabitz, J. Chem. Phys. **122**, 084110 (2005).

[95] Q. Ren, G. G. Balint-Kurti, F. R. Manby, M. Artamonov, T. S. Ho, and H. Rabitz, J. Chem. Phys. **124**, 014111 (2006).

[96] S. Zou, G. G. Balint-Kurti, and F. R. Manby, J. Chem. Phys. **127**, 044107 (2007).

[97] K. Nakagami, Y. Mizumoto, and Y. Ohtsuki, J. Chem. Phys. **129**, 194103 (2008).

[98] H. Umeda, M. Takagi, S. Yamada, S. Koseki, and Y. Fujimura, J. Am. Chem. Soc. **124**, 9265 (2002).

[99] F. Großmann, L. Feng, G. Schmidt,T. Kunert, and R. Schmidt, Europhys. Lett. **60**, 201 (2002).

[100] M. Artamonov, T. S. Ho, and H. Rabitz, Chem. Phys. **305**, 213 (2002).

[101] K. Hokia, S. Kosekib, T. Matsushitab, R. Sahnounc, and Y. Fujimura, J. Photochem. Photobiol. A: Chemistry **178**, 258 (2006).

[102] Y. Kurosaki, M. Artamonov, T. S. Ho, and H. Rabitz, J. Chem. Phys. **131**, 044306 (2009).

[103] I. Barth, J. Manz, Y. Shigeta, and K. Yagi, J. Am. Chem. Soc. **128**, 7043 (2006).

[104] M. Yamaki, S. -I. Nakayama, K. Hoki, H. Kono, and Y. Fujimara, Phys. Chem. Chem. Phys. **11**, 1662 (2009).

[105] Y. Kurosaki, K. Yokoyama, and A. Yokoyama, J. Chem. Phys. **131**, 144305 (2009).

[106] C. M. Tesch and R. de Vivie-Riedle, Phys. Rev. Lett. **89**, 157901 (2002).

[107] C. M. Tesch and R. de Vivie-Riedle, J. Chem. Phys. **121**. 12158 (2004).

[108] D. Babikov, J. Chem. Phys. **121**, 7577 (2004).

[109] S. Suzuki, K. Mishima, and K. Yamashita, Chem. Phys. Lett. **410**, 358 (2005).

[110] M. Tsubouchi and T. Momose, Phys. Rev. A **77**, 052326 (2008).

[111] M. Schröder and A. Brown, J. Chem. Phys. **131**, 034101 (2009).

[112] R. S. Judson and H. Rabitz, Phys. Rev. Lett. **68**, 1500 (1992).

[113] C. J. Bardeen, V. V. Yakovlev, K. R. Wilson, S. D. Carpenter, P. M. Weber, and W. S. Warren, Chem. Phys. Lett. **280**, 151 (1997).

[114] A. Assion, T. Baumert, M. Bergt, T. Brixmer, B. Kiefer, V. Seyfried, M. Strehle, and G. Gerber, Science **282**, 919 (1998).

[115] D. Yelin, D. Meshulach, and Y. Silberberg, Opt. Lett. **22**, 1793 (1997).

[116] D. Meshulach and Y. Silberberg, Nature **396**, 239 (1998).

[117] V. D. Kleimann. S. M. Arrivo, J. S. Melinger, and E. J. Heilweil, Chem. Phys. **233**, 207 (1998).

[118] T. C. Weinacht, J. Ahn, and P. H. Bucksbaum, Nature **397**, 233 (1999).

[119] D. J. Tannor, R. Kosloff, and A. Bartana, Faraday Discuss. **113**, 365 (1999).

[120] T. Hornung, R. Meier, and M. Motzkus, Chem.Phys. Lett. **326**, 445 (2000).

[121] R. Bartels, S. Backus, E. Zeek, L. Misoguti, G. Vdovin, I. P. Christov, M. M. Murnane and H. C. Kapteyn, Nature **406**, 164 (2000).

[122] R. J. Levis, G. M. Menkir, and H. Rabitz, Science **292**, 709 (2001).

[123] J. Herek, W. Wohllehen, R. Cogdell, D. Zeidler, and M. Motzkus, Nature **417**, 533 (2002).

[124] J. Savolainen, R. Fanciulli, N. Dijkhuizen, A. L. Moore, J. Hauer, T. Buckup, M. Motzkus, and J. L. Herek, Proc. Natl. Acad. Sci. USA **105**, 7641 (2008).

[125] V. I. Prokhorenko, A. M. Nagy, S. A. Waschuk, L. S. Brown, R. R. Birge, and R. J. D. Miller, Science **313**, 1257 (2006).

[126] V. I. Prokhorenko, A. M. Nagy, L. S. Brown, and R. J. D. Miller, Chem. Phys. **341**, 296 (2007).

[127] D. G. Kuroda, C. P. Singh, Z. Peng and V. D. Kleiman, Science **326**, 263 (2009).

[128] T. Brixner, M. Strehle, and G. Gerber, Appl. Phys. B **68**, 281 (1999).

[129] T. Brixner and G. Gerber, Chem. Phys. Chem. **4**, 418 (2003).

[130] C. Ventalon, J. M. Fraser, M. H. Vos, A. Alexandrou, J. -L. Martin, and M. Joffre, Proc. Natl. Acad. Sci. USA **101**, 13216 (2004).

[131] A. M. Weiner, Rev. Sci. Instrum. **71**, 1929 (2000).

[132] M. Dantus and V. V. Lozovoy, Chem. Rev. **104**, 1813 (2004).

[133] P. Nuernberger, G. Vogt, T. Brixner, and G. Gerber, Phys. Chem. Chem. Phys. **9**, 2470 (2007).

[134] H. Kawashima, M. W. Wefers, and K. A. Nelson, Ann. Rev. Phys. Chem. **46**, 627 (1995).

[135] R. de Vivie-Riedle and U. Troppmann, Chem. Rev. **107**, 5082 (2007).

Chapter 2

Theory

The control of chemical dynamics by designing optimally controlled laser pulses (IR and UV) constitutes the main theme of this thesis. The design of optimal pulse is carried out within the framework of optimal control theory (OCT) and the system dynamics along with the optimized pulse is followed from the first principles by numerically solving the time-dependent Schrödinger equation (TDSE). It is clear from the brief description given above that the complete task is quite involved both from the view points of the theoretical and numerical implementation. In this chapter the basic working equations and numerical strategies to solve them are enumerated.

2.1 Light-matter interaction

As mentioned above, we have studied the evolution of a system subject to light fields, using principles of time-dependent quantum mechanics. The principles governing the interaction, especially in the perturbative regime, of light with matter are fairly well understood. In this section, we will discuss some of the basic concepts for understanding how light interacts with matter. To start with, let us consider the interaction between pulsed laser light and the classical charged particles. The dynamics of the electric field, $\mathbf{E}(\mathbf{r}, t)$, and magnetic field, $\mathbf{B}(\mathbf{r}, t)$,

as well as the particles is determined by Maxwell's equations for the fields [1]

$$\begin{aligned}
\nabla \cdot \mathbf{E}(\mathbf{r},t) &= \frac{1}{\epsilon_0}\rho(\mathbf{r},t), && (2.1)\\
\nabla \cdot \mathbf{B}(\mathbf{r},t) &= 0, && (2.2)\\
\nabla \times \mathbf{E}(\mathbf{r},t) &= -\frac{1}{c}\frac{\partial}{\partial t}\mathbf{B}(\mathbf{r},t), && (2.3)\\
\nabla \times \mathbf{B}(\mathbf{r},t) &= \frac{1}{c}\frac{\partial}{\partial t}\mathbf{E}(\mathbf{r},t) + \frac{1}{\epsilon_0 c}\mathbf{j}(\mathbf{r},t), && (2.4)
\end{aligned}$$

in combination with the Lorentz's equation for the charged particles moving in an electromagnetic field:

$$m_i\frac{d\mathbf{v_i}}{dt} = F(\mathbf{r}_i,t) = q_i\left[\mathbf{E}(\mathbf{r_i},t) + \frac{\mathbf{v_i}}{c}\times\mathbf{B}(\mathbf{r_i},t)\right]. \quad (2.5)$$

In the above equations m_i, q_i, $\mathbf{r}_i$ and $\mathbf{v}_i$ are the mass, charge, position and velocity of ith particle, respectively. The density ρ and current $\mathbf{j}$ [cf., Eqs. (2.1) & (2.4)] of classical charged particles are defined by

$$\begin{aligned}
\rho(\mathbf{r},t) &= \sum_i q_i\delta[\mathbf{r}-\mathbf{r}_i(t)], && (2.6)\\
\mathbf{j}(\mathbf{r},t) &= \sum_i q_i v_i\delta[\mathbf{r}-\mathbf{r}_i(t)]. && (2.7)
\end{aligned}$$

The symbols ϵ_0 and c in Eqs. (2.1)-(2.4) denote the permitivity of free space and speed of light, respectively.

In order to solve for $\mathbf{E}(\mathbf{r},t)$ and $\mathbf{B}(\mathbf{r},t)$ from Maxwell's equations [cf., Eqs. (2.1)-(2.4)] it is convenient to express both these fields in terms of auxiliary quantities $\mathbf{A}(\mathbf{r},t)$, vector potential and $\Phi(r,t)$, scalar potential as (hereafter we drop the coordinate and time dependence for simplicity)

$$\begin{aligned}
\mathbf{B} &= \boldsymbol{\nabla}\times\mathbf{A}, && (2.8)\\
\mathbf{E} &= -\frac{1}{c}\frac{\partial\mathbf{A}}{\partial t} - \boldsymbol{\nabla}\Phi. && (2.9)
\end{aligned}$$

The choice of these vector and scalar potentials is not unique. That is different forms of these quantities (the so-called gauges) give the same electric

and magnetic fields. Therefore, it follows from Eqs. (2.8) & (2.9) that other potentials such as $\mathbf{A}'$ and Φ' can be constructed as

$$\mathbf{A}' = \mathbf{A} + \boldsymbol{\nabla}\varphi, \tag{2.10}$$

$$\Phi' = \Phi - \frac{1}{c}\frac{\partial\varphi}{\partial t}, \tag{2.11}$$

where φ is an arbitrarily chosen scalar field. The choice often made for φ is the so called Coulomb gauge. In this gauge, it is chosen such that, $\nabla^2\varphi = -\boldsymbol{\nabla}\cdot\mathbf{A}$, which implies from Eq. (2.11) that

$$\nabla\cdot\mathbf{A}' = 0. \tag{2.12}$$

It is hereby mentioned that different choices of φ that satisfy $\nabla^2\varphi = 0$ will also satisfy Eq. (2.12). This freedom is exploited in the discussion later in the text.

The classical Hamiltonian H (i.e., total energy) of the combined system of the particles and the fields is given by

$$\begin{aligned} H &= \sum_i \frac{1}{2}m_i\left(\frac{d\mathbf{r}_i}{dt}\right)^2 + \sum_i q_i\Phi_{\rm i}(\mathbf{r}_i) + \frac{\epsilon_0}{2}\int[\mathbf{E}^2(\mathbf{r},t) + \mathbf{B}^2(\mathbf{r},t)]d^3r, \\ &\equiv \sum_i \frac{1}{2}m_i\left(\frac{d\mathbf{r}_i}{dt}\right)^2 + V_C + H_R., \end{aligned} \tag{2.13}$$

Where the three terms in the right hand side of the above equation successively are the sum of the KE of the particles, the Coulomb potential (V_C) and the energy of the electromagnetic field (H_R). Where 'R' refers to radiation. And, the electric potential, $\Phi_i(\mathbf{r}_i)$, is defined as

$$\Phi_{\rm i}(\mathbf{r}) = \frac{1}{4\pi\epsilon_0}\sum_{j<i}\frac{q_j}{|\mathbf{r}-\mathbf{r}_j|}. \tag{2.14}$$

Now, let us consider the dynamics of particles whose variables are quantized under the influence of classical light fields. This leads to the concept of semiclassical theory of light interacting with quantized particles. The first step for quantization of particle dynamics is to express its velocity [cf., Eq. (2.13)] in

terms of canonical momenta ($\mathbf{p_i}$) in the presence of electromagnetic fields, which is defined as [2]

$$\mathbf{p}_i = m_i \frac{d\mathbf{r}_i}{dt} + \frac{q_i}{c}\mathbf{A}(\mathbf{r}, t). \tag{2.15}$$

From Eqs. (2.13) & (2.15), the Hamiltonian H is expressed as

$$H = \sum_i \frac{1}{2m_i}\left[\mathbf{p}_i - \frac{q_i}{c}\mathbf{A}(\mathbf{r}, t)\right]^2 + V_C + H_R. \tag{2.16}$$

The quantized Hamiltonian is obtained by replacing the canonical momentum by its operator form in the coordinate representation:

$$\mathbf{p}_j \rightarrow -i\hbar\boldsymbol{\nabla}_j, \tag{2.17}$$

$$H = \sum_j \frac{1}{2m_j}\left[-i\hbar\boldsymbol{\nabla}_j - \frac{q_j}{c}\mathbf{A}(\mathbf{r}_j, t)\right]^2 + V_C + H_R = H_M + H'(t) + H_R, \tag{2.18}$$

where the material Hamiltonian, H_M, given by

$$H_M = \sum_j \frac{-\hbar^2}{2m_j}\nabla_j^2 + V_C, \tag{2.19}$$

and the interaction Hamiltonian, $H'(t)$, is

$$H'(t) = \sum_j \frac{iq_j\hbar}{m_j c}\boldsymbol{\nabla}_j \cdot \mathbf{A}(\mathbf{r}_j, t) + \frac{q_j^2}{2m_j c^2}A^2(\mathbf{r}_j, t). \tag{2.20}$$

Given the quantized Hamiltonian of Eq.(2.18), the TDSE for the particles whose wavefunction is $\Psi(\mathbf{r}, t)$ (where $\mathbf{r}$=$\{\mathbf{r}_j, j = 1, 2..N\}$), is written as

$$i\hbar\frac{\partial\Psi(\mathbf{r}, t)}{\partial t} = \left\{\sum_j \frac{1}{2m_j}[-i\hbar\boldsymbol{\nabla}_j - \frac{q_j}{c}\mathbf{A}(\mathbf{r}_j, t)]^2 + V_C\right\}\Psi(\mathbf{r}, t). \tag{2.21}$$

The dynamics of the particles in the presence of field can be obtained by solving the above TDSE. The contribution of the H_R term in TDSE for particles is absent because it is a function of only the field variables [cf., Eq. (2.13)].

Further, Eq. (2.21) can be simplified on the grounds that the spatial variation of $\mathbf{A}$ corresponding to the particle displacements $\mathbf{r_j}$ in a molecule is

small. This is because the wavelength of the field typically vary in the order of 10^3 Å, while the displacements in molecules vary between 1 to 10 Å . It is therefore a reasonable approximation to replace all the $\mathbf{r_j}$ dependence in $\mathbf{A}$ by the center-of-mass position of the molecule, usually the z-projection of it is relevant if the field as a plane wave (or its superposition) is considered.

$$\mathbf{A}(\mathbf{r}_j, t) \approx \mathbf{A}(z_j, t) \tag{2.22}$$

This is called the "semiclassical dipole approximation" for the reasons that will become clear below.

Exploiting the gauge freedom and choosing φ as

$$\varphi = -\sum_i \mathbf{r}_i \cdot \mathbf{A}(z, t), \tag{2.23}$$

to satisfy Eq. (2.12) since $\nabla^2\varphi = 0$. Here the satisfaction of Eq. (2.12) is clearly due to the neglect of $\mathbf{r_i}$ dependence in $\mathbf{A}$ [cf., Eq. (2.22)].

The TDSE [cf., (2.21)] can now be written using the definition of V_C [cf., Eq. (2.13)] and φ [cf., Eq. (2.22)] and noting that $\boldsymbol{\nabla}\varphi = -\mathbf{A}$, as

$$i\hbar\frac{\partial\Psi(\mathbf{r}, t)}{\partial t} = \sum_j \left[\frac{-\hbar^2}{2m_j}\nabla_j^2 + q_j\Phi_j\mathbf{r}_j + \frac{q_j}{c}\mathbf{r}_j \cdot \frac{\partial\mathbf{A}(z, t)}{\partial t}\right]\Psi(\mathbf{r}, t). \tag{2.24}$$

The last term of the above equation can be simplified further using Eq. (2.9) and now the TDSE reads as

$$i\hbar\frac{\partial\Psi(\mathbf{r}, t)}{\partial t} = \sum_j \left[\frac{-\hbar^2}{2m_j}\nabla_j^2 + q_j\Phi_j\mathbf{r}_j - q_j\mathbf{r}_j \cdot \mathbf{E}(z, t)\right]\Psi(\mathbf{r}, t). \tag{2.25}$$

The simplicity of this equation results from the disappearance of both the vector potential and the gradient operator. Additionally, there is a scalar potential as a product of the electric field and the position vector of each particle. This product simply adds to the Coulomb potential.

More concisely, Eq. (2.24) can be written as

$$i\hbar\frac{\partial\Psi(t)}{\partial t} = [H_M + H_{MR}(t)]\Psi(t), \tag{2.26}$$

where H_M is the material Hamiltonian and H_{MR} represents the matter-radiation interaction term in the dipole approximation,

$$H_{MR} = -\mu \cdot \mathbf{E}(z,t), \tag{2.27}$$

where μ is the molecular transition dipole moment, given by

$$\mu \equiv \sum_j q_j \mathbf{r}_j. \tag{2.28}$$

It is possible to consider multipole interaction with the field whenever dipole approximation is not valid, i.e., spatial variations of the field as a function of $\mathbf{r}_j$ cannot be neglected [3]. However, in all the works considered in this thesis the dipole approximation is found to suffice and hence we describe light-matter interaction using Eqs. (2.26)-(2.28).

2.2 Theory of coupled electronic surfaces

2.2.1 Nonadiabatic coupling

Before we present discussion on nonadiabatic coupling between electronic surfaces, we briefly review some of the underlying basic concepts. One of such basic and central concept is the Born-Oppenheimer (BO) approximation [4].

2.2.1.1 The BO approximation

The starting point for this would be the full molecular Hamiltonian, written as

$$\hat{H} = \sum_i -\frac{\hbar^2 \nabla^2_{e,i}}{2\mathrm{m}} + \sum_{j>i} \frac{e^2}{|r_{e,i} - r_{e,j}|} + \sum_i -\frac{\hbar^2 \nabla^2_{N,i}}{2\mathrm{M}_i} + \sum_{j>i} \frac{Z_i Z_j e^2}{|R_{N,i} - R_{N,j}|} - \sum_{ij} \frac{Z_j e^2}{|r_{e,i} - R_{N,j}|}, \tag{2.29}$$

where we denote the electron and nuclear coordinates and momenta as $\{r, \nabla_e\}$ and $\{R, \nabla_N\}$, respectively. Z_i represents the nuclear charge on nucleus i and m and M_i denote the masses of the electron and nuclei, respectively. In short the above equation is equivalently represented as

$$\hat{H} \equiv \hat{T}_e + \hat{V}_e + \hat{T}_N + \hat{V}_N + \hat{V}_{eN}. \tag{2.30}$$

The five terms namely are, electron KE, electron-electron PE, nuclear KE, nuclear-nuclear PE and electron-nuclear PE. Now let us consider the time-independent TISE in full molecular coordinate space (for notational simplicity we drop the subscripts of the r_e and R_N hereafter),

$$\hat{H}(r,R)\Psi(r,R) = E\Psi(r,R), \tag{2.31}$$

where $\Psi(r,R)$ is an energy eigenfunction and E is the associated energy eigenvalue.

In order to find an approximate solution of the Eq. (2.31), it is convenient to treat the electron and nuclear motions separately based on the large difference in their masses. This implies that electrons can readjust instantaneously to a changing nuclear degrees of freedom. Based on this fact let us now consider the TISE for the electrons only at a given nuclear configuration as

$$\hat{H}_e\psi(r;R) = E_e(R)\psi(r;R), \tag{2.32}$$

where, $\hat{H}_e = \hat{T}_e + \hat{V}_e + \hat{V}_{eN}$. Now the full molecular wavefunction, $\Psi(r,R)$, can be written as

$$\Psi(r,R) = \psi(r;R)\phi(R). \tag{2.33}$$

Substituting Eq. (2.33) back into Eq. (2.31) and using Eq. (2.32) we obtain

$$\hat{H}(r,R)\{\psi(r;R)\phi(R)\} = (E_e(R) + V_N)\{\psi(r;R)\phi(R)\}$$

$$+\sum_i \frac{-\hbar^2}{2M_i}\left(\psi(r;R)\nabla^2\phi(R) + 2\boldsymbol{\nabla}\psi(r;R)\cdot\boldsymbol{\nabla}\phi(R) + \nabla^2\psi(r;R)\phi(R)\right) \tag{2.34}$$

$$= E\psi(r;R)\phi(R), \tag{2.35}$$

where $\boldsymbol{\nabla}$ refers to $\boldsymbol{\nabla_N}$, here and henceforth.

The last two terms in the summation of the Eq. (2.35) involve differentiation of the electronic wavefunction with respect to nuclear coordinates. The most significant of these two terms is the first term which is referred to as derivative coupling, a vector quantity. The second term is a scalar coupling term and it

contributes less significantly to the overall nonadiabatic correction. It can be shown that these two terms are proportional to the ratio of mass of electrons to that of nuclei to a power of 1/4 [4], and hence are way smaller when compared to the other terms. Therefore, these terms can be neglected and the following approximated TISE for the nuclei is obtained as:

$$\hat{H}(r,R)\phi(R) = (\hat{T}_N + E_e(R) + V_N(R))\phi(R) = E\phi(R). \tag{2.36}$$

The effective potential, $(E_e(R) + V_N)$, in the above equation is given by the Eq.(2.32) for a fixed nuclear configuration. Here the V_N simply becomes an additive constant at a given nuclear framework. The neglect of the two terms in Eq. (2.34) is known as BO approximation. The Eq. (2.36) implies that for every value of R, the TISE for electrons [i.e., Eq.(2.32)] should be solved. Given that the eigenvalue spectrum is a function of R, connecting these values while preserving the ordering of levels gives rise to adiabatic electronic potential (eigenvalue) curves. These potentials along with the addition of V_N provides an effective potential in Eq. (2.36) under which the nuclei move and the potentials are called as adiabatic potentials.

When these adiabatic electronic states exhibit avoided crossings the terms involving $\boldsymbol{\nabla}\psi(r;R)$ can become significant leading to failure of the BO approximation. This is because in the region of avoided crossings the adiabatic electronic states change their physical character dramatically and hence the derivatives of electronic wavefunction with respect to nuclear coordinates can be quite large. Also, the derivative coupling elements diverge at the point of degeneracy if the two adiabatic states are degenerate (from Hellmann-Feynman theorem). Then solving Eq. (2.36) becomes difficult. In order to avoid this difficulty it is more convenient to consider diabatic electronic states. These states retain their physical character and they smoothly cross each other, making the size of the derivative couplings as small as possible. In order to find solution of the Schrödinger equation in situations where the BO approximation fails, two

representations namely, adiabatic and diabatic, are used. Below we present a brief review on them.

2.2.1.2 Adiabatic representation

Let us write the total molecular wavefunction in Eq. (2.31) in an adiabatic basis as:

$$\Psi(r;R) = \sum_{n=0}^{\infty} \psi_n(r;R)\phi_n(R). \tag{2.37}$$

Substituting the Eq. (2.37) in Eq. (2.34) and projecting onto $\psi_m(r;R)$ gives rise to the following set of coupled equations:

$$\begin{aligned} \sum_n H_{mn}(R)\phi_n(R) &= \sum_n \{(\hat{T_N} + E_{e,n}(R) + V_N(R))\delta_{mn} + 2T^{(1)}_{mn}(R)\cdot\boldsymbol{\nabla} \\ &\quad + T^{(2)}_{mn}(R)\}\phi_n(R), \\ &= E\phi_m(R), \end{aligned} \tag{2.38}$$

where

$$T^{(1)}_{mn} = \langle\psi_m|\boldsymbol{\nabla}\psi_n\rangle, \tag{2.39}$$

$$T^{(2)}_{mn} = \langle\psi_m|\nabla^2\psi_n\rangle. \tag{2.40}$$

Here the $T^{(1)}_{mn}$ is a vector and $T^{(2)}_{mn}$ is a scalar. The $\boldsymbol{\nabla}$ is a derivative with respect to mass-weighted nuclear coordinates. And, the Dirac notation indicates integration over electronic coordinates only.

The normalization condition for electronic wavefunctions over entire nuclear space is defined as

$$\langle\psi_m|\psi_n\rangle = \delta_{nm}. \tag{2.41}$$

This implies the matrix $T^{(1)}_{mn}$ is anti-Hermitian, i.e.,

$$T^{(1)}_{mn} = -T^{(1)*}_{nm}. \tag{2.42}$$

This implies further, for a real-valued electronic wavefunctions the diagonal matrix elements of $T^{(1)}_{mn}$ become zero:

$$T^{(1)}_{nn}(R) = 0. \tag{2.43}$$

Therefore, keeping only the diagonal terms in Eq. (2.38) the TISE Eq. (2.38) for the nuclei with additional non-vanishingly small contribution from $T^2_{nn}(R)$, becomes

$$(\hat{T}_N + E_{e,n}(R) + V_N(R) + T^{(2)}_{nn}(R))\phi_n(R) = E\phi_n(R). \tag{2.44}$$

As discussed above the derivative terms present in Eqs. (2.34), (2.38) and (2.44) can be quite large near the degeneracy of electronic states or at avoided crossings and it is difficult to calculate them. To avoid such a difficulty below we introduce a representation that uses diabatic basis alternative to the adiabatic basis used here.

2.2.1.3 Diabatic representation

As mentioned above, in order to make the derivative coupling terms as small as possible diabatic basis is a convenient choice. A diabatic basis is defined as a set of electronic wavefunctions at a suitably chosen nuclear framework and hence is independent of nuclear coordinates. In practice, since it is impossible to make the derivative coupling terms vanish to zero there exists no "strict diabatic" basis. Sometimes, a diabatic basis is also referred to as "crude adiabatic" basis as it is independent of nuclear coordinates.

The total molecular wavefunction in the crude adiabatic basis is written as

$$\Psi(r; R) = \sum_n \psi_n(r; R_0)\phi^{(0)}_n(R), \tag{2.45}$$

where R_0 represents a reference nuclear geometry and $\psi_n(r; R_0)$ are the solutions of TISE at this geometry.

The TISE for these solutions is given as

$$\hat{H}_e(r; R_0)\psi_n(r; R_0) = \{\hat{T}_e + \hat{V}(r; R_0)\}\psi_n(r; R_0) = E_{e,n}(R_0)\psi_n(r; R_0). \tag{2.46}$$

where $\hat{V}(r, R_0)$ contains $\hat{V}_e$ and $\hat{V}_{eN}$. Substituting Eq. (2.45) into Eq. (2.31) we get

$$\sum_{n=0}^{\infty} \psi_n(r; R_0)(\hat{T}_N + \hat{V}_N)\phi_n^{(0)}(R) + \sum_{n=0}^{\infty} \phi_n^0(R)\hat{H}_e\psi_n(r; R_0) = \sum_{n=0}^{\infty} E\psi_n(r; R_0)\phi_n^{(0)}(R) \tag{2.47}$$

It should be noted that the nuclear KE operator, $\hat{T}_N$, does not act on the electronic wavefunctions $\psi_n(r; R_0)$ as they are defined at fixed nuclear geometry R_0.

Upon projection onto $\psi_m(r; R)$ and using Eq. (2.46) we obtain a set of coupled equations:

$$\sum_{n=0}^{\infty}[(\hat{T}_N + \hat{V}_N)\delta_{mn} + H_{e,mn}]\phi_n^{(0)}(R) = E\phi_m^{(0)}(R), \tag{2.48}$$

where

$$H_{e,mn} = \langle\psi_m(R_0)|\hat{H}_e(r; R)|\psi_n(R_0)\rangle. \tag{2.49}$$

Let us rewrite $\hat{H}_e(r; R)$ using $\hat{V} \equiv \hat{V}_e + \hat{V}_{eN}$ as (we also follow here the explicit coordinate dependence of electronic KE operator in the expressions below for clarity)

$$\hat{H}_e(r; R) = \hat{T}_e(r) + \hat{V}(r; R) = \hat{H}_e(r; R_0) - \hat{V}(r; R_0) + \hat{V}(r; R), \tag{2.50}$$

since

$$\hat{H}_e(r; R_0) - \hat{V}(r; R_0) = \hat{T}_e(r) + \hat{V}_e(r) + \hat{V}_{eN}(r; R_0) - [\hat{V}_e(r) + \hat{V}_{eN}(r; R_0)] = \hat{T}_e(r). \tag{2.51}$$

And we also note that

$$\hat{T}_e(r; R_0) = \hat{T}_e(r)$$
$$\hat{V}_e(r; R_0) = \hat{V}_e(r)$$

Now let us simplify the $H_{e,mn}$ using Eq. (2.50) and Eq. (2.46):

$$H_{e,mn} \quad = \quad \langle\psi_m(r; R_0)|\hat{H}_e(r; R_0) - \hat{V}(r; R_0) + \hat{V}(r; R)|\psi_n(r; R_0)\rangle$$

$$= \quad E_{e,n}(R_0)\delta_{mn} + \langle\psi_m(r;R_0)|\hat{V}(r,R) - \hat{V}(r,R_0)|\psi_n(r;R_0)\rangle$$

Using Eq. (2.52) the set of coupled equations in Eq. (2.48) can be simplified as

$$\sum_n \{T_{nn}\delta_{nm} + U_{mn}\}\phi_n^{(0)} = E\phi_m^{(0)}, \tag{2.52}$$

where

$$U_{mn} = \langle\psi_m(R_0)|\hat{V}(r,R) - \hat{V}(r,R_0)|\psi_n(R_0)\rangle. \tag{2.53}$$

Here also the integration is over electronic coordinates only. And we note that $\hat{T}_{nn} = \hat{T}_N + \hat{V}_N + E_n^{el}(R_0)$.

It is easy to see the simplicity of Eq. (2.53) compared to Eq. (2.38) obtained by switching to a diabatic basis. In the diabatic representation, the coupling between the electronic states is coordinate dependent, $U_{mn}(R)$, and does not involve any derivative terms. The diagonal elements of U-matrix are the diabatic potentials which are smooth functions of nuclear coordinates and the transitions between them are caused by the off-diagonal elements of U-matrix. The time-dependent version of Eq. (2.52) for the nuclei is generally solved by the time propagation techniques already discussed above, which is carried out in this thesis.

2.2.1.4 Adiabatic to diabatic transformation

The transformation of electronic basis, $\boldsymbol{\psi}(r,R)$, from adiabatic to diabatic representation can be carried out by an unitary matrix $\mathbf{A}^\dagger(R)$ as

$$\boldsymbol{\psi}^{\mathbf{a}}(r,R) = \mathbf{A}^{\dagger}(R)\boldsymbol{\psi}^{\mathbf{d}}(r,R). \tag{2.54}$$

where **a** and **d** indicate adiabatic and diabatic, respectively.

The adjoint matrix, $\mathbf{A}(R)$, can transform the nuclear basis $\boldsymbol{\phi}(R)$ between the two representations:

$$\boldsymbol{\phi}^{\mathbf{a}}(R) = \mathbf{A}(R)\boldsymbol{\phi}^{\mathbf{d}}(R). \tag{2.55}$$

The transformation matrix $\mathbf{A}(R)$ obeys the following equation [5, 6] (we drop R dependence for notational simplicity hereafter):

$$\boldsymbol{\nabla}\mathbf{A} + \mathbf{T^{(1)}}\mathbf{A} = 0, \tag{2.56}$$

then

$$\nabla^2\mathbf{A} + 2\mathbf{T^{(1)}} \cdot \boldsymbol{\nabla}\mathbf{A} + \mathbf{T^{(2)}}\mathbf{A} = 0. \tag{2.57}$$

where $\boldsymbol{T^{(1)}}$ and $\boldsymbol{T^{(2)}}$ are defined earlier in Eqs. (2.39) and (2.40), respectively. Using Eqs. (2.56) and (2.57), after some algebra, the simplified Schrödinger equation for the nuclei in the diabatic representation is written as

$$\nabla^2\boldsymbol{\phi}^{\mathbf{d}} - \frac{2\mu}{\hbar^2}(\mathbf{U} - E)\boldsymbol{\phi}^{\mathbf{d}} = 0, \tag{2.58}$$

and is consistent with Eq. (2.59). Where $\mathbf{U}$ is the potential in the diabatic representation [5, 6], given by

$$\mathbf{U} \equiv \mathbf{A}^{\dagger}\mathbf{V}\mathbf{A}, \tag{2.59}$$

and the adiabatic potentials, $\mathbf{V}$, are obtained as eigenvalues by diagonalizing the diabatic potential matrix $\mathbf{U}$:

$$\mathbf{V} = \mathbf{A}\mathbf{U}\mathbf{A}^{\dagger}. \tag{2.60}$$

The necessary condition for Eq. (2.56) to always have a solution is to satisfy the following "curl condition" [6–8]

$$\boldsymbol{\nabla} \times \mathbf{T^{(1)}}\mathbf{A} = 0. \tag{2.61}$$

This equation can be trivially satisfied in case of diatomics as $\mathbf{T^{(1)}}$ has only one component. However, in polyatomics the $\mathbf{T^{(1)}}$ has multiple components and to satisfy Eq. (2.61), the size of the matrix $\mathbf{A}$ become large (as the size of the adiabatic basis), the task becomes computationally demanding. If it is so, the purpose of the diabatic basis (which provides a compact representation in the presence of degeneracy or avoided crossings), is defeated. Therefore, in practice,

there exists only an approximate diabatic basis that minimizes the derivative coupling terms as much as possible. In what follows we present a discussion on the intersections between PESs as a natural extension to the adiabatic and diabatic representations.

2.2.1.5 Conical intersections and geometric phase

Let us consider two adiabatic potentials $V_{\pm}$ as functions of nuclear seperation R in a diatomic and the possibility of their intersection. As already mentioned, in the diabatic representation there occurs a residual potential coupling between the diabatic potentials. Hence we consider the PE matrix $\mathbf{U}$ in this representation in order to facilitate the following derivation.

$$\mathbf{U} = \begin{pmatrix} U_{11} & U_{12} \\ U_{21} & U_{22} \end{pmatrix}. \tag{2.62}$$

The two adiabatic potentials, $V_{\pm}$, as eigenvalues are obtained by diagonalizing the matrix $\mathbf{U}$ and they are

$$V_{\pm} = \frac{U_{11} + U_{22}}{2} \pm \frac{1}{2}\sqrt{(U_{11} - U_{22})^2 + 4|U_{12}|^2}. \tag{2.63}$$

Now, consider the seperation between the two potentials:

$$\Delta V = V_{+} - V_{-} = \sqrt{(U_{11} - U_{22})^2 + 4|U_{12}|^2}. \tag{2.64}$$

This difference becomes zero when

$$U_{11}(R) = U_{22}(R), \tag{2.65}$$

and

$$U_{12}(R) = 0. \tag{2.66}$$

Here the two equations Eq. (2.65) and Eq. (2.66) are to be satisfied by one parameter R. In general, there is no reason that why a single unknown should satisfy any two equations. Hence, in one dimension the potentials cannot cross.

This is called non-crossing rule. When stated more clearly for diatomics that has only one degree of freedom, in general, two adiabatic PE curves with the same symmetry cannot cross each other but exhibit avoided crossing [9]. However, in polyatomics, there exist many nuclear degrees of freedom and hence the electronic states can become degenerate [10].

In two dimensions, there occurs generally a set of isolated points where the potential energy surfaces (PESs) can touch. These points are referred as "conical intersections" (CIs). This is because the eigenvalues of a diabatic PE matrix $\mathbf{U}$ in two (multi) dimension(s) form a double cone with its vertex as the point of degeneracy [10, 11]. If the number of dimensions (N) are greater than two, the space in which all the intersections that form CIs lie is N-2 dimensional space, with Eqs. (2.65) and (2.66) acting as two constraints. The space other than N-2 dimensional intersection space, where the degeneracy between surfaces is lifted out, is called branching space.

The profound implications of CIs include ultrafast nonadiabatic transitions between electronic states and the geometric phase (GP) effect. The latter implies development of phase π when an adiabatic electronic wavefunction encircles a CI by 2π [12, 13] giving rise to non-single valuedness of the electronic wavefunction. In order for the total molecular wavefunction to be single valued, the nuclear wavefunction should also develop a phase of π. The approach that suits quite well to avoid this discontinuity is to transform to diabatic basis as discussed above. Treating the dynamics by adopting diabatic representation naturally includes the GP effect as it ensures correct boundary condition while encircling a CI [14]. In this representation, the signature of the GP effect appears clearly in terms of a change of nodal pattern in the nuclear wavefunction along a coupling coordinate in the presence of CI while undergoing diabatic transfer. This is due to the action of diabatic coupling element in $\mathbf{U}$, which is an odd function of coupling coordinate (in first order). The implications of this GP effect will be discussed in Chap. 5

and Chap. 7.

2.2.1.6 Construction of diabatic potentials

As mentioned previously, it is convenient to perform calculations of the nonadiabatic dynamics in the diabatic representation. For this, the necessary ingredients required in the Hamiltonian are diabatic potentials and the associated coupling between them. We discuss here the construction of such potentials and their coupling approximately from *ab initio* calculated potential energy values [15–19].

The elements of diabatic potential matrix [cf., Eq. (2.62)] can be Taylor expanded up to second order with respect to the dimensionless normal coordinates (Q) at the reference geometry as,

$$U_{11}(\mathbf{Q}) = E_1 + U_0(\mathbf{Q}) + \sum_t \kappa_t^{(1)} Q_t + \sum_{m,m'} \gamma^{(1)}_{m,m'=t,c} Q_m Q'_m, \quad (2.67)$$

$$U_{22}(\mathbf{Q}) = E_2 + U_0(\mathbf{Q}) + \sum_t \kappa_t^{(2)} Q_t + \sum_{m,m'} \gamma^{(2)}_{m,m'=t,c} Q_m Q'_m, \quad (2.68)$$

$$U_{12}(\mathbf{Q}) = U_{21}(\mathbf{Q}) = \sum_c \lambda_c Q_c, \quad (2.69)$$

$$U_0(\mathbf{Q}) = \frac{1}{2}\sum_t \omega_t Q_t^2 + \frac{1}{2}\sum_t \omega_c Q_c^2, \quad (2.70)$$

where E_1 and E_2 are energies of the respective electronic states at the reference geometry. The $\kappa_t^{(n)}$ $(n = 1, 2)$ represent gradients of the potentials at the reference geometry and they are referred to as the first-order intra-state coupling constants. The Q_t are termed as tuning modes as they tune the energy gap between the electronic states and may lead to a crossing between diabatic PESs [18, 19]. The quantity λ_c represents the first-order inter-state vibronic coupling constant and the associated modes Q_c are called coupling modes [18, 19]. The $\gamma^{(n)}_{m,m'}$ $(n = 1, 2)$ represent intra-state bilinear coupling constants and are related to the Dushinsky rotation of normal modes [18–20].

Along a coupling coordinate, from Eq. (2.63), we have,

$$V_+ + V_- = U_{11} + U_{22}, \tag{2.71}$$

$$(V_+ - V_-)^2 = (U_{11} - U_{22}) + (U_{12})^2. \tag{2.72}$$

This shows that the diabatic potentials (U_{11} and U_{22}) and the coupling between them (U_{12}) can be determined from *ab initio* calculated potentials (i.e., adiabatic, $V_\pm$). Practically, a least square fit is performed based on the Eqs. (2.71)- (2.72) in order to predict the diabatic potentials and their coupling as functions of Q_t. The least square fitting is allowed because at $Q_c = 0$ both adiabatic and diabatic potentials are identical.

In the linear vibronic coupling scheme, the parameters $\kappa_t^{(n)}$ [cf., Eqs. (2.67) and (2.68)] and λ_c [cf., Eq. (2.63)] are estimated more conveniently using the following relations, respectively [18, 19] as,

$$\kappa_t^{(1,2)} = \left.\frac{\partial U_{1,2}}{\partial Q_t}\right|_{\mathbf{Q}_0}, \tag{2.73}$$

$$\lambda_c = \left.\left[\frac{1}{8}\frac{\partial^2}{\partial Q_c^2}(V_+ - V_-)^2\right]^{1/2}\right|_{\mathbf{Q}_0}. \tag{2.74}$$

2.2.1.7 Symmetry selection rules

Here, the selection of the most important tuning and coupling modes that are useful in characterizing the CIs is presented following the symmetry rules given below. As the electronic Hamiltonian is always totally symmetric, for nonvanishing linear intra-state coupling constant,

$$\kappa_t^{(n)} = \left.\langle\Phi_n|\frac{\partial \hat{H}_{el}}{\partial Q_t}|\Phi_n\rangle\right|_{\mathbf{Q}_0}, \tag{2.75}$$

the mode along which the gradient of the potential energy is varied must also be totally symmetric. These nonzero gradi- ents induce the nuclear motions in the electronic states.

The symmetry rule for selection of coupling mode requires that the direct product of the symmetry species of two electronic states and the vibrational mode must contain A_1:

$$\Gamma_1 \times \Gamma_{Q_c} \times \Gamma_2 \supset A_1 \quad \Rightarrow \quad \Gamma_{Q_c} = \Gamma_1 \times \Gamma_2 \tag{2.76}$$

In this scenario, the inter-state coupling constant,

$$\lambda_c^{nm} = \frac{\partial}{\partial Q_c} \langle \Phi_n | \hat{H}_{el} | \Phi_m \rangle \Big|_{\mathbf{Q}_0}, \tag{2.77}$$

is nonvanishing.

When two states of same symmetry, i.e., $\Gamma_1 = \Gamma_2$, cross they exhibit "accidental CIs". In this situtation, both the tunning and coupling modes belong to A_1 symmetry [15].

2.3 Optimal control theory

The objective of control theory, in general, is to modify the behavior of a dynamical system by an external control. The theoretical machinery required to achieve optimum control over the dynamics of a system under stated goals and circumstances/constraints is provided by the Optimal control theory (OCT) [21]. In OCT, one arrives at a best shape of an external control (or optimal values of control variables) that gives rise to optimum control. The best shape of the control is judged via incorporation of a performance index functional in OCT. Typically, this functional depends upon the control variables and state of a dynamical system (whose history at a given time entirely depends on the action of the external control, which is a function of say time; hence the name functional). The subject of OCT is interdisciplinary and has broad scope of applications in engineering as well as in science [22, 23].

In this work, we used OCT to design laser pulses that can regulate the evolution of an initial state of molecular system to its desired final state [24,

25]. The idea behind such a controlled evolution is to irradiate the system (via interaction with dipole moment operator, $\hat{\boldsymbol{\mu}}$) with a specially crafted laser pulse(s) in amplitudes, frequency components, etc., of the time dependent electric field, $\boldsymbol{\epsilon}(t)$. Therefore, the designing of shaped fields has become a general task of quantum control in combination with TDSE with a dipole-coupled interaction term (where the electric field, $\boldsymbol{\epsilon}(t)$, enters) included. The TDSE within the dipole approximation [26, 27] is read as

$$i\hbar\frac{\partial}{\partial t}\psi(x,t) = [\hat{H} - \hat{\boldsymbol{\mu}} \cdot \boldsymbol{\epsilon}(t)]\psi(x,t). \tag{2.78}$$

where $\hat{H}_0$ is the system Hamiltonian and $\hat{H}_1(t)$ and -$\hat{\boldsymbol{\mu}} \cdot \boldsymbol{\epsilon}(t)$ is the dipole-coupled interaction term.

As mentioned above, the general mathematical framework of OCT provides a way of designing the electric field of a pulse in combination with TDSE of Eq. (2.78) for efficient control of molecular dynamics. In OCT, the time profile and spectral composition of laser pulse is varied throughout the dynamics in order to explore all the pathways associated with multiple excitations. Thereby complex quantum mechanical interferences among all these pathways come into play. This interference becomes constructive if the desired target is achieved successfully and destructive, if not. Therefore, tuning the laser pulse parameters to their optimal values for manipulating the interference among all the dynamical pathways (created by the pulse that span its spectrum) in order to achieve the maximum target yields, is done using OCT. Below, we discuss the mathematical formulation of OCT.

2.3.1 Formulation

Generally, the objective of control theory is to steer a system by a controller for achieving predefined target successfully. OCT is formulated in terms of maximizing the expectation values of a certain physical observable operator, $\hat{O}$, in a desired target state, $\psi(T)$, or a reaction channel by the design and application of a suitable laser pulse to a molecular system in a given initial state, $\psi(0) = \phi_i$. Hence the aim is to design an optimal laser field, $\boldsymbol{\epsilon}(t)$, in order to perform the given task efficiently abiding by some physical constraints/conditions [28–30].

The design of such a laser field is carried out by phrasing the problem in terms of optimization of a field dependent "cost functional", $J[\boldsymbol{\epsilon}(t)]$. It contains mainly three terms,

$$J[\epsilon(t)] = J_o + J_p + J_c, \tag{2.79}$$

where, the first term, J_o, has the physical objective. This is a measure of the extent of achieving the desired objective. The second term, J_p, as a constraint contains the penalties on control field in order to avoid any undesirable physical processes. And the third term, J_c, contains the dynamical constraint that the system must obey the TDSE during its controlled evolution.

The objective term can involve either time-independent or time-dependent control targets depending on the desired dynamical goal. In the case of time-independent control target the goal is to drive a quantum system to a predefined state $\psi(T)$ at time T, from its initial state, $\psi(0) = \phi_i$. A typical example involving such targets is state selective population transfer. For instance here, maximization of the expectation value of the target operator $\hat{O}$ (which becomes a projection operator, defined below) is considered at the end of laser interaction. On the other hand, the goal in the case of time-dependent control target [31] in the objective term involves maximization of the expectation value of the target operator $\hat{O}$ at each point of time. An example is maximization of outgoing dissociative flux across the dividing line at $R = R_d$ at each point of time

i.e., maximization of the expectation value of the flux operator (defined below).

Using time-independent control targets the objective term in general can be written as

$$J_o = \langle\psi(T)|\hat{O}|\psi(T)\rangle. \tag{2.80}$$

Specifically, for controlling state selective population transfer (that determines the transition probability) as considered in our work, if the operator defined is a projection operator as $\hat{O} = |\phi_f\rangle\langle\phi_f|$, where $|\phi_f$ is the preselected target state. In this situation J_o can be written as

$$J_o = \langle\psi(T)|\phi_f\rangle\langle\phi_f|\psi(T)\rangle = |\langle\psi(T)|\phi_f\rangle|^2. \tag{2.81}$$

This shows that the overlap of laser-driven initial wavefunction with the target wavefunction is to be maximized at the end of the pulse duration in order to maximize J_o.

Similarly, using time-dependent control targets the objective term in general can be written as

$$J_o = \langle\psi(t)|\hat{O}|\psi(t)\rangle. \tag{2.82}$$

Specifically, for controlling dissociative flux as considered in our work, the objective is to maximize the expectation value of the flux operator at each point of time, which can be defined as

$$J_o = \int_0^T dt\langle\psi(t)|\hat{F}_R|\psi(t)\rangle. \tag{2.83}$$

The flux operator, $\hat{F}_R$ (more formal details are discussed later in the text), appearing in above equation, is given as

$$\hat{F}_R = \frac{1}{2}\left\{\frac{\hat{p}_R}{m}\delta(R - R_\infty) + \delta(R - R_\infty)\frac{\hat{p}_R}{m}\right\} \tag{2.84}$$

where $\hat{p}_R = -i\frac{\partial}{\partial R}$ is the momentum operator conjugate to the dissociation coordinate, R, and m is the reduced mass of molecule along R; the quantity R_∞ is a suitably chosen large value of R.

The second term, J_p, is a penalty (or fluence) term meant to curb the freedom of the electric field to assume any higher intensities in achieving desired task during its action. In strong field limit, it is not clear whether this term is needed at all. However, incorporation of this term in the cost functional ensures smooth convergence in such cases also. Therefore we used this term in all the works of this thesis. The mathematical form of this term is the following:

$$J_p = -\alpha_0 \int_0^T |\boldsymbol{\epsilon}(t)|^2 dt, \tag{2.85}$$

where, α_0 is a positive scalar factor that specifies the weight of the fluence term in the functional. The use of penalty term in the cost functional is to manage the fluence of the field. Therefore this term as a constraint avoids any undesirable physical processes such as ionization during the control dynamics by limiting the field intensities within physically reasonable limits.

The third term, J_c, is a dynamical constraint. This term ensures that the system must follow the TDSE in Eq. (2.78) at all time.

Let us illustrate the OCT formalism by considering the control problem involving two electronic states. The cost functional to be optimized can now be written as [28, 29] (we use atomic units "throughout the work, $\hbar = 1$)

$$J[\epsilon(t)] = \lim_{T\to\infty} \langle\psi(T)|\hat{O}|\psi(T)\rangle - \alpha_0 \int_0^T |\epsilon(t)|^2 dt - 2Re\left[\int_0^T \langle\chi(t)|\frac{\partial}{\partial t} + i\hat{H}|\psi(t)\rangle\right] \tag{2.86}$$

where

$$\hat{H} \;=\; \begin{pmatrix} \hat{H}_e & -\hat{\boldsymbol{\mu}}.\boldsymbol{\epsilon}^*(\boldsymbol{t}) \\ -\hat{\boldsymbol{\mu}}.\boldsymbol{\epsilon}(\boldsymbol{t}) & \hat{H}_g \end{pmatrix} \tag{2.87}$$

and

$$\psi = \begin{pmatrix} \psi_e \\ \psi_g \end{pmatrix} \quad ; \quad \chi = \begin{pmatrix} \chi_e \\ \chi_g \end{pmatrix} \tag{2.88}$$

The off-diagonal terms of the matrix Hamiltonian on the right hand side (RHS) of Eq. (2.87) represent the potential due to laser-molecule interaction and the

quantity, $\boldsymbol{\epsilon}(t)$, defines the time-dependent electric field component of the laser radiation. The wavefunctions ψ_e, ψ_g in Eq. (2.88) represent the projections of the system wavefunction, ψ, on the excited and ground state surfaces, respectively. For notational simplicity we have dropped spatial dependence of wavefunctions.

The function $\psi(t)$ is the wavefunction at time, t, propagated under the influence of the laser field $\boldsymbol{\epsilon}(t)$ and $\psi(T)$ is the target state specified at the final time, $t = T$. The function $\chi(t)$ is a Lagrange multiplier function introduced to ensure that the dynamics of the system is governed by the Schrödinger equation. The factor α_0, as mentioned above, is a positive weighting parameter which adjusts the contribution of the radiation energy to the functional $J[\boldsymbol{\epsilon}(t)]$.

Using variational calculus, the cost functional is varied (Eq. 2.86) with respect to $\psi(t)$, $\chi(t)$ and $\epsilon(t)$ to zero in first order. This results into the following nonlinear pulse design equations (The derivation of these equations is presented in Appendix B).

$$\frac{\partial J}{\partial \chi(t)} = 0 \Rightarrow i\frac{\partial \psi(t)}{\partial t} = \hat{H}\psi(t), \quad \psi(t=0) = \psi(0), \tag{2.89}$$

$$\frac{\partial J}{\partial \psi(t)} = 0 \Rightarrow i\frac{\partial \chi(t)}{\partial t} = \hat{H}\chi(t), \quad \chi(T) = \hat{O}\psi(T), \tag{2.90}$$

$$\frac{\partial J}{\partial \boldsymbol{\epsilon}^*(t)} = 0 \Rightarrow \boldsymbol{\epsilon}(t) = \frac{i}{\alpha_0}[\langle \chi_e(t)|\hat{\boldsymbol{\mu}}|\psi_g(t)\rangle - \langle \psi_e(t)|\hat{\boldsymbol{\mu}}|\chi_g(t)\rangle. \tag{2.91}$$

The equations (2.89-2.91) are central for the design of an optimal field. The first of which i.e., Eq. (2.89) describes the time evolution of $\psi(t)$ with a specified initial condition, $\psi(t = 0) = \psi(0)$, under the influence of laser pulse. The Eq. (2.90) implies that the Lagrange multiplier function, $\chi(t)$, must satisfy TDSE at all times with the specified boundary condition, $\chi(T) = \hat{O}\psi(T)$, at final time T. The last of these equations i.e, Eq. (2.91) determines the optimal field, $\boldsymbol{\epsilon}(t)$, of the laser pulse using $\psi(t)$ and $\chi(t)$. In order to obtain the optimal field these nonlinear coupled differential equations are solved iteratively. For numerical evaluation of these equations various iterative methods [28, 29] have been developed. However, the convergence of these methods to optimal (often local) solution is in general

slow and involve significant computational complexity.

As an alternative to these iterative methods two efficient approaches for numerically solving the above equations exist–the gradient based approaches such as conjugate gradient (CG) method [32–35] and approaches based on biological evolution strategies such as Genetic algorithm (GA). Both these approaches involve a search for optimal parameters of laser field that maximize the cost functional. In doing so the CG method uses the gradient of the cost functional with respect to electric field as a central object whereas the GA uses the prescribed definition of the cost functional. The details of theoretical implementation of CG and GA optimization methods are discussed below.

2.3.1.1 Conjugate gradient method

The optimization of an electric field in OCT is carried out using the CG method as suggested by Balint-Kurti *et al.,* [36–39]. The laser field $\epsilon(t)$ is given by [40]

$$\epsilon(t) = s(t)\cdot \epsilon_0(t), \tag{2.92}$$

where $s(t)$ is gaussian shaped envelope which ensures smooth decay of laser field $\epsilon(t)$ at initial and final time and $\epsilon_0(t)$ is a sinusoidal function. The form of the envelope function, $s(t)$ is assumed as

$$s(t) = exp\frac{-(t-T/2)^2}{(T/4)^2}, \tag{2.93}$$

where T is the total time of pulse duration. The gradient of J with respect to the $\epsilon_0(t)$ at time t after k number of iterations in the optimization cycle is written as

$$g^k(t) = \frac{\partial J^k}{\partial \epsilon_0^k(t)} = -2s(t)\left[\alpha_0\epsilon^k(t) - Im\langle\chi(t)|\frac{\partial \hat{H}}{\partial \epsilon^k(t)}|\psi(t)\rangle\right]. \tag{2.94}$$

Both $\psi(t)$ and $\chi(t)$ are propagated in time using a time propagation technique discussed below. The time evolution is done in discrete time steps (t_i). One

can proceed to search for the parameter space of electric fields $\epsilon(t_i)$ that maximize the cost functional value. Then a line search is performed along the Polak-Ribiere-Polyak search direction [41]. The search direction is defined as follows.

$$d^k(t_i) = g^k(t_i) + \lambda^k \cdot d^{k-1}(t_i), \tag{2.95}$$

where the conjugate gradient parameter λ^k is given as,

$$\lambda^k = \frac{\sum_i g^k(t_i)^T (g^k(t_i) - g^{k-1}(t_i))}{\sum_i g^{k-1}(t_i)^T g^{k-1}(t_i)}. \tag{2.96}$$

During the line search the search direction $d^k(t_i)$ is projected [42] to avoid higher values of $\epsilon(t_i)$ from predefined range.

In order to achieve a pulse having simple frequency structure, the frequency range of the laser pulse has to be restricted within the specified range (ω_{min} : ω_{max}) [43]. The frequency filtering is done with a 20^{th} -order Butterworth bandpass filter [44] by filtering the projected search direction,

$$h(\omega) = \left[\left(1 + \left(\frac{\omega_{min}}{\omega} \right)^{40} \right) \left(1 + \left(\frac{\omega}{\omega_{max}} \right)^{40} \right) \right]^{\left(\frac{-1}{2}\right)}. \tag{2.97}$$

The projected search direction is Fourier transformed to obtain a function of frequency, and this function is further multiplied by $h(\omega)$ and transformed back to the time domain, which can be expressed as,

$$d^k_{p,filter}(t) = \int h(\omega) F_\omega[d^k_p(t)] e^{-i\omega t} d\omega, \tag{2.98}$$

where $F_\omega[d^k_p(t)]$ is the Fourier component at frequency ω.

The updated electric-field is expressed as

$$\epsilon^{k+1}(t_i) = \epsilon^k(t_i) + \lambda s(t_i) d^k_{p,filter}(t_i), \tag{2.99}$$

where λ is determined by a line search algorithm.

2.3.1.2 Genetic algorithm

In GA, the laser pulse can be specified in general as a sum of two terms

$$\epsilon_{ga}(t) \quad = \quad \epsilon_g(t) + \epsilon_r(t). \tag{2.100}$$

In general $\epsilon_g(t)$ can be defined by a sinusoidal wave with an envelope function. In the present work the term $\epsilon_g(t)$ is set to zero. The term $\epsilon_r(t)$ is defined as

$$\epsilon_r(t) \quad = \quad E_0 \sin(\omega t) s(t), \tag{2.101}$$

where, E_0 is determined by the pulse area theorem as suggested by Cheng *et al.* [45] and ω is the transition frequency for the transition of interest. The envelop function, $s(t)$, ensures smooth switch on and off of the pulse at the initial and final time, respectively. In the present works of the thesis, it is characterized by four positive time parameters t_0, t_1, t_2 and t_3, where $t_0 < t_1 \leq t_2 < t_3$. Usually, t_0 is set to 0, and t_3 to T. The time period from t_0 to t_1 is the rise time of the pulse, t_2 to t_3 is the switch off period and the intermediate section, t_1 to t_2, the envelop takes the value of unity giving rise to a plateau. The envelop function $s(t)$ is given by

$$s(t) = \begin{cases} \sin^2\left[\frac{\pi}{2}\left(\frac{t-t_0)}{t_1-t_0}\right)\right] & \text{for} \quad t_0 \leq t \leq t_1, \\ 1 & \text{for} \quad t_1 \leq t \leq t_2, \\ \sin^2\left[\frac{\pi}{2}\left(\frac{t_3-t)}{t_3-t_2}\right)\right] & \text{for} \quad t_2 \leq t \leq t_3 = T. \end{cases} \tag{2.102}$$

Using GA, different possible combinations of the amplitude (ϵ), two time parameters (t_1 and t_2) and frequency (ω) are searched. The aim is to find the best possible combination of these four parameters among all possible permutations. A combination of these four parameters that define an electric field is termed as an 'individual' in GA. In order to find the best possible solution, certain individuals (population size) from randomly selected parameters in the parameter space are considered. Each parameter set then represents a chromosome (corresponding to

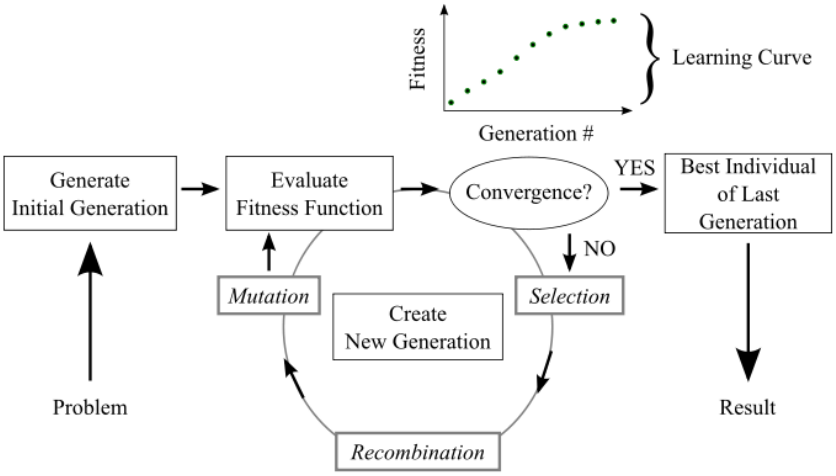

Figure 2.1: Schematic representation of GA optimization: A generation of individuals by random selection are subjected to evaluation by a fitness function which is given as the degree to which desired target is reached, of a given problem. The optimization proceeds iteratively using evolutionary strategies in a loop until the convergence is reached for a given target objective. The best individual of the final generation represents the optimal solution of a given problem. The learning curve represents the fitness values of the best individuals in each generation [J. Savolainen, *Coherent Control of Biomolecules*, Thesis, Switzerland (2008)].

a trial laser field) in analogy with biological evolution process. These randomly selected individuals are then subjected to optimization in an effort to find the best solution that gives rise to maximum value of the cost functional. This optimization is performed iteratively, as follows. In every generation, fitness of each population is measured in terms of the values of the cost functional. Subject to natural selection, a specified number of populations (electric fields) survive. The algorithm relies on the techniques of the natural selection process such as inheritance, mutation, selection, and crossover. Schematic representation of the optimization process using GA algorithm is presented in Fig. 2.1. In the present works, we have implemented the values of the GA parameters that are widely used as suggested in Ref. [46] for achieving good convergence of the algorithm.

2.4 Time propagation

To determine the time evolution of a quantum mechanical system, $\psi(x,t)$, one should solve the TDSE

$$i\hbar\frac{\partial}{\partial t}\psi(x,t) = \hat{H}\psi(x,t). \tag{2.103}$$

with an initial condition $\psi(x,0) = \psi_0$, where, $\psi(x,0)$ is the wavefunction at time $t = 0$ and ψ_0 is a specified initial wavefunction.

In the case of time-independent Hamiltonian, $\hat{H}$, the formal solution of the above equation is written as

$$\psi(x,t) = e^{\frac{-i\hat{H}t}{\hbar}}\psi(x,0), \tag{2.104}$$

where $\psi(x,t)$ is a wavefunction at time t. In order to solve the TDSE, it is clear that the operation on the initial wavefunction with Hamiltonian, $\hat{H}$, should be performed. In fact, the Taylor expansion of $e^{\frac{-i\hat{H}t}{\hbar}}$ suggests the operation must be repeatedly performed. If ψ is an eigenfunction of $\hat{H}$ with eigenvalue E, i.e.,

$$\hat{H}\psi = E\psi, \tag{2.105}$$

then, Eq. (2.104) can be written as

$$\psi(x,t) = e^{\frac{-i\hat{H}t}{\hbar}}\psi(x,0) = e^{\frac{-iEt}{\hbar}}\psi(x,0). \tag{2.106}$$

However, in the case of time-dependent Hamiltonian, $\hat{H}$, the approximate solution of Eq. (2.103) for small time intervals, dt, for which Hamiltonian is assumed to be constant, is given as

$$\psi(x,t+dt) \approx e^{\frac{-i\hat{H}}{\hbar}dt}\psi(x,t). \tag{2.107}$$

Here, the size of the time interval dt decides the accuracy of this approximate solution. The shorter the size of dt the more accurate the solution is. Therefore, the propagated wavefunction at final time T in the presence of a pulse can be

expressed using product of propagators (N times) over short time intervals, dt, as follows

$$\psi(x,T) = \hat{O}(Ndt)\hat{O}((N-1)dt)...\hat{O}(dt)\psi(x,t=0), \tag{2.108}$$

where, N defines the total number of time steps which implies $Ndt = T$ and $\hat{O}(dt)$ is a short time propagator which can be represented as

$$\hat{O}(dt) = e^{\frac{-i\hat{H}}{\hbar}dt} = e^{\frac{-i[\hat{T}+\hat{V}]}{\hbar}dt}. \tag{2.109}$$

By definition, the Hamiltonian operator is the sum of kinetic energy (KE) operator $\hat{T}$ and potential energy (PE) operator $\hat{V}$. To evaluate the action of $\hat{H}$ on ψ, one must recognize that $\hat{T}$ and $\hat{V}$ have different characteristics. The $\hat{V}$ is a local operator (i.e., can be diagonalized) in coordinate space representation, and $\hat{V}\psi$ is obtained by simple multiplication in this space. Whereas, the $\hat{T}$ is a non-local operator (i.e., cannot be diagonalized) in this representation and hence the calculation of $\hat{T}\psi$ involves computationally tedious derivatives of the wavefunction. In the momentum space representation reverse is true, i.e., $\hat{T}$ is local and $\hat{V}$ is non-local. This implies that calculation of $\hat{V}\psi$ becomes tedious whereas $\hat{T}\psi$ involves a simple multiplication, in momentum space. It is clear that moving back and forth between both these spaces is inevitable. This idea has led to the development of grid representation based methods involving Fourier transforms. The use of Fourier transforms together with the grid representation provides a simple, reliable and robust method for evaluating $\hat{H}\psi$. Below we describe a method, namely Fourier-grid method [47–49], that involves Fourier-transforms as well as grids.

2.4.1 The Fourier-grid method

In Fourier-grid method a simple transformation between coordinate space and momentum space is employed on a grid of evenly spaced points. In this method, the actions of $\hat{T}$ and $\hat{V}$ are carried out in their local representations. That means

the PE matrix becomes diagonal in coordinate space and the values are given by just the potentials at all grid points, whereas the KE matrix is diagonal in momentum space and is given by eigenvalues of $\hat{T}$ at all grid points. It is always feasible to work in coordinate representation because the potential could be a complicated function of position in many situations unlike the KE which is a Laplacian operator. Hence the complexity in PE for certain situations forbids one to work in momentum representation since the transformation of PE between two spaces could be cumbersome. So, in order to evaluate the KE matrix in coordinate space, where the potential matrix is diagonal, the Fourier transformation is employed to go back and forth between the coordinate and momentum spaces. The formulation of the Fourier-grid method in one dimension [50] is given below. Further extension of this method to multiple dimensions [51] is simple. The theoretical details are as follows.

The Hamiltonian operator, $\hat{H}$, for a particle of mass m moving on a line, can be written usually as the sum of $\hat{T}$ and $\hat{V}$ as

$$\hat{H} = \hat{T} + \hat{V} = \frac{\hat{p}^2}{2m} + V(\hat{x}), \tag{2.110}$$

where the momentum operator, $\hat{p}$, is given as

$$\hat{p} = -i\hbar\frac{\partial}{\partial x}. \tag{2.111}$$

In coordinate representation, the eigenfunctions $|x\rangle$ of the position operator $\hat{x}$ with associated eigenvalues x, act as basis vectors:

$$\hat{x}|x\rangle = x|x\rangle. \tag{2.112}$$

These basis vectors satisfy respectively the orthogonality and completeness relationships as

$$\langle x|x'\rangle = \delta(x - x'), \tag{2.113}$$

and

$$\int_{-\infty}^{\infty} |x\rangle\langle x| = \hat{I}_x. \tag{2.114}$$

Now, the PE (V) "matrix elements" in the coordinate basis can be written as

$$\langle x'|V(\hat{x})|x\rangle = V(x)\langle x'|x\rangle = V(x)\delta(x-x'). \tag{2.115}$$

Simillarly, the momentum basis can be formed by the eigenfunctions $|k\rangle$ of the operator $\hat{p}$ with eigenvalues $\hbar k$:

$$\hat{p}|k\rangle = \hbar k|k\rangle. \tag{2.116}$$

As above, the corresponding orthogonality and completeness relationships for the momentum bais can be defined as

$$\langle k|k'\rangle = \delta(k-k'), \tag{2.117}$$

and

$$\int_{-\infty}^{\infty} |k\rangle\langle k| = \hat{I}_k. \tag{2.118}$$

Now, the "matrix elements" of $\hat{T}$ in momentum basis can be defined as

$$\langle k'|\hat{T}|k\rangle = T_k\delta(k-k') = \frac{\hbar^2k^2}{2m}\delta(k-k'). \tag{2.119}$$

The back and forth transformation between the coordinate space and the momentum space is performed using Fourier Transformation. The following transformation matrices are used to carry out the forward and inverse Fourier transformations between these two representations,

$$\langle k|x\rangle = \frac{1}{(2\pi)^{1/2}}\exp(-ikx), \tag{2.120}$$

and

$$\langle x|k\rangle = \frac{1}{(2\pi)^{1/2}}\exp(ikx). \tag{2.121}$$

Thus, the matrix elements of $\hat{H}$ in the coordinate representation are given as

$$\begin{aligned}
\langle x|\hat{H}|x'\rangle &= \langle x|[\hat{T}+\hat{V}]|x'\rangle \\
&= \langle x|\hat{T}|x'\rangle + V(x)\delta(x-x') \\
&= \langle x|\hat{T}\left\{\int_{-\infty}^{\infty}|k\rangle\langle k|\right\}|x'\rangle dk + V(x)\delta(x-x') \\
&= \int_{-\infty}^{\infty}\langle x|k\rangle T_k\langle k|x'\rangle dk + V(x)\delta(x-x') \\
&= \frac{1}{2\pi}\int_{-\infty}^{\infty} e^{ik(x-x')}T_k dk + V(x)\delta(x-x'). \qquad (2.122)
\end{aligned}$$

Below we construct a discrete grid representation of the above Hamiltonian [Eq. (2.122)] for numerical applications.

Discretization and grids

For this purpose, the continuous coordinate spaces x and x' each are discretized into respective N evenly spaced grid points $\{x_i\}$ and $\{x_j\}$. They are given as

$$x_i = i\Delta x, \qquad i = 1, \cdots, N. \qquad (2.123)$$

$$x_j = j\Delta x, \qquad j = 1, \cdots, N. \qquad (2.124)$$

Where Δx is the uniform spacing between the successive grid points. Thus the Hamiltonian in Eq. (2.122) is an $N \times N$ matrix with H_{ij} corresponding to the position $i\Delta x$ and $j\Delta x$. The orthogonality condition [Eq. (2.113)] in this discrete grid can be expressed as

$$\Delta x\langle x_i|x_j\rangle = \delta_{ij}, \qquad (2.125)$$

and the identity operator (by completeness property)

$$\hat{I}_x = \sum_{i=1}^{N}|x_i\rangle\Delta x\langle x_i|. \qquad (2.126)$$

The grid length of the coordinate space is $L = N\Delta x$ which determines the longest wavelength (λ_{max}). The reciprocal grid size in momentum space is

determined using the grid length, and spacing chosen in coordinate space by the relation, $k = 2\pi/\lambda$. The momentum grid spacing is given as

$$\Delta k = \frac{2\pi}{\lambda_{max}} = \frac{2\pi}{L} = \frac{2\pi}{N\Delta x}. \tag{2.127}$$

For odd number of grid points N, the values of k in momentum space are evenly distributed around the central point $k = 0$.
An integer n can be defined as:

$$2n = (N-1). \tag{2.128}$$

Thus, the discrete grid in momentum space is defined as

$$\begin{aligned} k_l &= k_{min} + l\Delta k \\ &= \frac{-N\pi}{L} + l\frac{2\pi}{L} \\ &= \frac{-\pi}{\Delta x} + l\frac{2\pi}{N\Delta x}, \end{aligned} \tag{2.129}$$

where $l = 0, 1, \cdots, N-1$.

The grid representation of "matrix elements" of the Hamiltonian operator [Eq. (2.122)] is then

$$\begin{aligned} H_{ij} &= \langle x_i|\hat{H}|x_j\rangle \\ &= \frac{1}{2\pi}\sum_{l=-n}^{n} e^{il\Delta k(x_i - x_j)}\left[\frac{\hbar^2}{2m}(l\Delta k)^2\right]\Delta k + \frac{V(x_i)\delta_{ij}}{\Delta x} \\ &= \frac{1}{\Delta x}\left\{\sum_{l=-n}^{n}\frac{e^{il2\pi(i-j)/N}}{N}\left[\frac{\hbar^2}{2m}(l\Delta k)^2\right] + V(x_i)\delta_{ij}\right\}. \end{aligned} \tag{2.130}$$

This Hamiltonian matrix so constructed is referred to as the Fourier grid Hamiltonian (FGH). The FGH matrix elements can be evaluated analytically [50, 52–54] and diagonalizing this matrix will yield eigenvectors and eigenvalues of the bound potentials. The computations involving the action of FGH on ψ during its time evolution scale as N^2 (as with multiplication of matrices $\hat{H}$ and ψ). Consequently, when the calculations of time propagation of a wavepacket (WP)

on a multidimensional space are required to carry out sufficiently accurately, the computational effort needed can be very great. A considerable computational efficiency can be achieved by using fast Fourier transform (FFT) algorithm [48, 55, 56] to perform the discrete Fourier transform (DFT) of the wavefunction. By using FFT algorithm to perform the DFT, the method scales as $NlnN$ as compared to N^2 in the case of matrix multiplications. Also the use of FFT technique avoids the construction and storage of matrices and it merely works by rearranging the elements of the vector representing wavefunction. Hence, this gives a significant computational saving for large input vectors.

We will exploit the FFT algorithm in a time propagation scheme discussed below, for the action of $\hat{H}$ on ψ during the time evolution of the wavefunction ψ.

2.4.2 The split operator method

In the previous section, we have seen a numerical method (i.e., FGH method) to perform the operation $\hat{H}\psi$ on a grid of points. The method involves using approximate eigenvalues and eigenvectors of $\hat{H}$ for time propagation of ψ. However, the method is limited to time-independent Hamiltonians and is computationally less efficient because it requires the construction and diagonalization of the FGH, the latter scaling as N^3. There exists another approach to deal with numerical implementation of time propagation by retaining the exponent structure of the propagator, i.e., $e^{-i\hat{H}t/\hbar}$. Using such an approach we address the question of the numerical implementation of $e^{-i\hat{H}t/\hbar}\ \psi$ directly rather than repeated operations of $\hat{H}\psi$ as mentioned earlier. The approach in which the exponent structure of the propagator is retained, but is approximated as a product of kinetic and potential energy factor [55] as

$$e^{\frac{-i\hat{H}}{\hbar}dt} \approx e^{\frac{-i\hat{T}dt}{\hbar}} e^{\frac{-i\hat{V}dt}{\hbar}}, \tag{2.131}$$

is called the "Split Operator" (SO) method [55, 56]. As the KE and PE operators do not commute, i.e., $[\hat{T}, \hat{V}] \neq 0$, the exponential term of the short propagator

[Eq. (2.109)] cannot be exactly split as

$$e^{\frac{-i\hat{H}}{\hbar}dt} = e^{\frac{-i\hat{T}dt}{\hbar}} e^{\frac{-i\hat{V}dt}{\hbar}}, \tag{2.132}$$

but can be approximated as in Eq. (2.131) by symmetrically splitting the Hamiltonian as

$$e^{\frac{-i\hat{H}}{\hbar}dt} \approx e^{\frac{-i\hat{T}dt}{2\hbar}} e^{\frac{-i\hat{V}dt}{\hbar}} e^{\frac{-i\hat{T}dt}{2\hbar}} + O(dt^3), \tag{2.133}$$

or

$$e^{\frac{-i\hat{H}}{\hbar}dt} \approx e^{\frac{-i\hat{V}dt}{2\hbar}} e^{\frac{-i\hat{T}dt}{\hbar}} e^{\frac{-i\hat{V}dt}{2\hbar}} + O(dt^3), \tag{2.134}$$

with an error, $O(dt^3)$, proportional to the the commutator $[\hat{T}, \hat{V}]$ (see Appendix A for details).

The splitting as shown in Eq. (2.133) is referred to as the PE referenced SO method [57], and the one in Eq. (2.134) is referred as the KE referenced SO method [57]. Using the former, [Eq. (2.107)] the time propagation of a wavefunction can be rewritten as

$$\psi(x, t + dt) \approx e^{\frac{-i\hat{T}dt}{2\hbar}} e^{\frac{-i\hat{V}dt}{\hbar}} e^{\frac{-i\hat{T}dt}{2\hbar}} \psi(x, t). \tag{2.135}$$

From the above equation it is clear that the consecutive operation of three exponents on the wavefunction, $\psi(t)$, at a given time t gives the time evolved wavefunction at time $t + dt$. The strategy is to employ these exponent operators locally. A local operation of the exponential form of the $\hat{T}$ is performed using FFT algorithm whereas the operation of the exponentiated $\hat{V}$ is performed by simple multiplication, $e^{\frac{-i\hat{V}dt}{\hbar}}\ \psi(x)$.

In one dimension, the time propagation of wavefunction in this scheme involves the following steps:

1. At first, the wavefunction is transformed from coordinate space (x) to momentum (k) space using FFT method, and then multiplied at each grid point by $e^{(-i\frac{\hbar^2 k^2}{2m}\frac{dt}{2\hbar})}$, that is, $e^{(-i\frac{\hbar^2 k^2}{2m}\frac{dt}{2\hbar})}\ \psi(k, t)$, where

$$\psi(k, t) = \frac{1}{(2\pi)^{1/2}} \int_{-\infty}^{\infty} \psi(x, t) e^{-ikx} dx = \mathbf{FFT}\{\psi(x, t)\}. \tag{2.136}$$

2. After this, the wavefunction is transformed back to the coordinate space by an inverse FFT method and then multiplied by $\exp(-i\frac{V(\hat{x})dt}{\hbar})$ as $e^{-i\frac{V(x)dt}{\hbar}}$ $\psi(x,t)$, where

$$\psi(x,t) = \frac{1}{(2\pi)^{1/2}} \int_{-\infty}^{\infty} \psi(k,t) e^{ikx} dk = \mathbf{FFT}^{-1}\{\psi(k,t)\}. \tag{2.137}$$

3. The resulting wavefunction is again Fourier transformed to the momentum space and then multiplied with other half of KE operator, $e^{-i\frac{\hbar^2 k^2}{2m}\frac{dt}{2\hbar}}$ as in point 1.

As the factor $e^{-i\frac{\hbar^2 k^2}{2m}\frac{dt}{2\hbar}}$ is independent of the propagation step, therefore, its left and right parts in Eq. (2.133) can be combined for two successive propagation steps.

In a similar way, the short time propagator in two dimensions (as far as the present work is concerned, it typically involves a tuning coordinate, R and a coupling coordinate, Q) can be defined as

$$\begin{aligned} \hat{U}(dt) \approx\ & e^{\frac{-i\hat{T}_R dt}{2\hbar}} e^{\frac{-i\hat{T}_Q dt}{2\hbar}} \\ & \cdot e^{\frac{-i\hat{V} dt}{\hbar}} e^{\frac{-i\hat{T}_Q dt}{2\hbar}} e^{\frac{-i\hat{T}_R dt}{2\hbar}}, \end{aligned} \tag{2.138}$$

where the action of the KE operator involving coordinate Q follows the similar procedure as explained for propagation of wavefunction in one dimensional case.

The SO method preserves unitarity of the evolution operator. The SO method can be used for time propagation of a wavefunction evolving on multiple electronic states with a coupling between them, either due to nonadiabatic interactions (time-independent) or interactions with light via TDM (time-dependent).

2.5 Physical observables

In this section, we discuss about the physical observables related to the work of this thesis.

2.5.1 Flux operator

The flux operator, $\hat{F}$, is a measure of probability of the current density through a dividing surface. The dividing surface Θ is located in such a way that the reactant and product channels are well seperated. Formally, the quantum flux operator, $\hat{F}$, is defined as

$$\hat{F} = i\left[\hat{H}, \hat{\Theta}\right], \tag{2.139}$$

$$\hat{\Theta} = H(R - R_f), \tag{2.140}$$

$$= \begin{cases} 0, & R<R_f \\ 1, & R>R_f \end{cases} \tag{2.141}$$

where H represents the Heaviside step function of the coordinate R. Since Θ is a function of R, it commutes with PE operator but not with KE operator. Therfore, the $\hat{F}$ takes the form [58]:

$$\hat{F} = i[\hat{T}, \hat{\Theta}]$$

$$= \frac{-i}{2m}\left\{\frac{\partial}{\partial R}\frac{\partial}{\partial R}H(R - R_f) - H(R - R_f)\frac{\partial}{\partial R}\frac{\partial}{\partial R}\right\} \tag{2.142}$$

$$= \frac{-i}{2m}\left\{\frac{\partial}{\partial R}\delta(R - R_f) + \delta(R - R_f)\frac{\partial}{\partial R}\right\}, \tag{2.143}$$

where,

$$\hat{T} = \frac{-1}{2m}\frac{\partial^2}{\partial R^2},$$

$$\frac{\partial}{\partial R}H(R - R_f) = \delta(R - R_f), \tag{2.144}$$

and $$H(R - R_f)\frac{\partial}{\partial R} = -\delta(R - R_f). \tag{2.145}$$

In Eq. (2.145) the adjoint of $\frac{\partial}{\partial R}$ operates on the Heaviside step function and $(\frac{\partial}{\partial R})^{\dagger}$ = - $\frac{\partial}{\partial R}$. For a given reaction coordinate, say R_1, the reaction probability in the i^{th} electronic state is given by the time-accumulated flux about a dividing surface at $R_1 = R_f$:

$$\begin{aligned} F_i^D(t) &= \int dt \, \langle \phi_i(R_1, R_2, .., t) | \hat{F} | \phi_i(R_1, R_2, .., t) \rangle \Big|_{R_1=R_f} \\ &= \int Im \left[\left\langle \phi(R_1, R_2, .., t) | \frac{\partial}{\partial R_1} \phi_i(R_1.R_2, .., t) \right\rangle \Big|_{R_1=R_f} \right] dt \quad (2.146) \end{aligned}$$

In the case of dissociation, the probability of dissociation in a particular channel is obtained by Eq. 2.146 at $R = R_d$. Where R_d is the point where analysis line is located through which the dissociation flux is measured.

2.5.2 Probability density

The probability density (PD) at a given time is defined as the absolute square of the nuclear WP in the i^{th} diabatic (or adiabatic) electronic state, as follows:

$$PD_i^{dia}(t, R_1, R_2, ..) = |\psi_i^{dia}(R_1, R_2, .., t)|^2, \quad (2.147)$$

$$PD_i^{aa}(t, R_1, R_2, ..) = |\psi_i^{ad}(R_1, R_2, .., t)|^2. \quad (2.148)$$

The probability density cuts along a particular nuclear degrees of freedom, say R_1, is obtained by integrating the abolute square of WP over all other degrees of freedom:

$$PD_i^d(t, R_1) = \int dR_2 \int dR_3 ... |\psi_i^d(R_1, R_2, R_3, .., t)|^2, \quad (2.149)$$

$$PD_i^a(t, R_1) = \int dR_2 \int dR_3 ... |\psi_i^a(R_1, R_2, R_3, .., t)|^2. \quad (2.150)$$

2.5.3 Electronic population probability

The quantity of primary focus in the coupled state dynamics is the time-dependence of population probabilities of the electronic states. Adiabatic

(P_i^{ad}) and diabatic (P_i^{dia}) electronic population probabilities are defined as expectation values of the respective projection operators:

$$P_i^{dia}(t) = \langle\Psi(t)|\Phi_i^{dia}\rangle\langle\Phi_i^{dia}|\Psi(t)\rangle, \tag{2.151}$$

$$P_i^{ad}(t) = \langle\Psi(t)|\Phi_i^{ad}\rangle\langle\Phi_i^{ad}|\Psi(t)\rangle. \tag{2.152}$$

The Eqs. 2.151 and 2.151 are equivalent to the respective expressions given by Eqs. 2.153 and 2.154 below. The latter represent the integrated probability densities of WP over all nuclear degrees of freedom in diabatic and adiabatic representation, respectively.

$$P_i^{dia}(t) = \int dR_1 \int dR_2 ... |\psi_i^{dia}(t, R_1, R_2, ...)|^2, \tag{2.153}$$

$$P_i^{ad}(t) = \int dR_1 \int dR_2 ... |\psi_i^{ad}(t, R_1, R_2, ...)|^2. \tag{2.154}$$

In the present work on dissociation, the following trick is employed for calculating both the adiabatic ($P_i^{ad}(t)$) and diabatic ($P_i^{dia}(t)$) population probabilities of an i^{th} state:

$$P_i^{dia}(t) = \int_0^{R_d} dR_1 \int dR_2 ... |\psi_i^{dia}(R_1, R_2, .., t)|^2 + F_i^D(t), \tag{2.155}$$

$$P_i^{ad}(t) = \int_0^{R_d} dR_1 \int dR_2 ... |\psi_i^{ad}(R_1, R_2, .., t)|^2 + F_i^D(t), \tag{2.156}$$

where $F_i^D(t)$ is the respective time-accumulated dissociative flux of diabatic and adiabatic WP calculated in the asymptotic region of PESs at, $R = R_d$, as given in Eq. (2.146). This way, the integration over large nuclear coordinate space (R_1) can be avoided.

Bibliography

[1] J. D. Jackson, *Classical Electrodynamics*, Wiley, New York, (1962).

[2] H. Goldstein, *Classical Mechanics*, 2nd Ed., Addison-Wesley, Reading, MA, (1980).

[3] R. Loudon, *The Quantum Theory of Light*, 2nd ed., Clarendon, Oxford, (1983).

[4] M. Born and R. Oppenheimer, Ann. Phys. **84**, 457 (1927).

[5] F. T. Smith, Phys. Rev. **179**, 111 (1969).

[6] M. Baer, Adv. Chem. Phys. **124**, 39 (2002).

[7] M. Baer, Mol. Phys. **40**, 1011 (1980).

[8] C. A. Mead and D. G. Truhlar, J. Chem. Phys. **77**, 6090 (1982).

[9] J. von Neumann and E. Wigner, Phys. Z. **30**, 467 (1929).

[10] E. Teller, J. Phys. Chem. **41**, 109 (1937).

[11] H. A. Jahn and E. Teller, Proc. Roy. Soc. **244**, 1 (1937).

[12] H. C. Longuet-Higgins, U. Öpik , M. H. L Pryce, and R. A. Sack Proc. Roy. Soc. A, **244**, 1 (1958).

[13] G. Herzberg and H. C. Longuet-Higgins, Discuss. Faraday Soc. **35**, 77 (1963).

[14] F. Boukaline, Chem. Phys. **441**, 31 (2014).

[15] H. Köppel, W. Domcke, and L. S. Cederbaum, Adv. Chem. Phys. **57**, 59 (1984).

[16] C. Woywod, W. Domcke, A. L. Sobolewski, and H. J. Werner, J. Chem. Phys. **100**, 1400 (1994).

[17] D. Simah, B. Hartke, and H.-J. Werner, J. Chem. Phys. **111**, 4523 (1999).

[18] W. Domcke and G. Stock, Adv. Chem. Phys. **100**, 1 (1997).

[19] W. Domcke, D. R. Yarkony, and H. Köppel, *Conical Intersections: Electronic Structure, Dynamics and Spectroscopy*, World Scientific, Singapore, (2004).

[20] Z. Lan, *Photo-induced Nonadiabatic Dynamics of Aromatic Molecules via Conical Intersections. Electronic-structure and Time-dependent Quantum Dynamics Calculations* , Thesis, Munich (2007).

[21] E. Lawrence, *An Introduction to Mathematical Optimal Control Theory: version 0.2* (online lecture notes; http://math.berkeley.edu/evans/).

[22] A. E. Bryson and Y. C. Ho, *Applied Optimal Control: Optimization, Estimation and Control*, Boca Raton, FL: taylor and Francis, (1975).

[23] R. F. Stengel, *Optimal Control and Estimation*, Mincola, NY: Dover, (1994).

[24] S. A. Rice and M. Zhao, *Optical Control of Molecular Dynamics*, Wiley Interscience, New York, (2000).

[25] M. Shapiro and P. Brumer, *Principles of the Quantum Control of Molecular Processes*, John Wiley and Sons Canada, Ltd., (2003).

[26] K. Sunderman and R. de Vivie-Riedle, J. Chem. Phys. **110**, 1896 (1999).

[27] S. P. Shah and S. A. Rice, J. Chem. Phys. **113**, 6536 (2000).

[28] S. Shi and H. Rabitz, J. Chem. Phys. **92**, 364 (1990).

[29] W. Zhu and H. Rabitz, Phys. Rev. A **58**, 4741 (1998).

[30] W. Zhu and H. Rabitz, J. Chem. Phys. **109**, 385 (1998).

[31] Y. Ohtsuki, G. Turinici, and H. Rabitz, J. Chem. Phys. **120**, 5509 (2004).

[32] W. H. Press, S. A. Teukolsky, W. T. Vetterling, and B. P. Flannery. *Numerical Recipes*, Cambridge U. P., Cambridge, MA, (1992).

[33] S. Shi, A. Woody, and H. Rabitz, J. Chem. Phys. **88**, 6870 (1988).

[34] J. Combariza, B. Just, J. Manz, and G. Paramonov, J. Phys. Chem. **95**, 10351 (1991).

[35] G. G. Balint-Kurti, S. Zou, and A. Brown, Adv. Chem. Phys. **138**, 43 (2008).

[36] G. G. Balint-Kurti, S. Zou and A. Brown, Adv. Chem. Phys. **138**, 43 (2008).

[37] G. G. Balint-Kurti, F. R. Manby, Q. Ren, M. Artamonov, Tak-San Ho and H. Rabitz, J. Chem. Phys. **122**, 084110 (2005).

[38] Q. Ren, G. G. Balint-Kurti, F. R. Manby, M. Artamonov, Tak-San Ho and H. Rabitz, J. Chem. Phys. **124**, 014111 (2006).

[39] W. H. Press, S. A. Teukolsky, W. T. Vetterling, and B. P. Flannery, *Numerical Recipes*, Cambridge University Press, Cambridge, (2000).

[40] K. Sundermann and R. de Vivie-Riedle, J. Chem. Phys. **110**, 1896 (1999).

[41] E. Polak, *Computational Methods in Optimization, Mathematics in Science and engineering*, Vol. 77, Academic Press, New York, (1971).

[42] E. G. Birgin, J. M. Martinez and M. Raydan SIAM J. Optim. **10**, 1196 (2000).

[43] P. Gross, D. Neuhauser, and H. Rabitz, J. Chem. Phys. **96**, 2834 (1992).

[44] L. R. Rabiner and C. M. Rader (Eds), *Digital Signal Processing*, IEEE Press, New York, (1972).

[45] T. Cheng and A. Brown, J. Chem. Phys. **124**, 034111 (2006).

[46] S. Sharma, H. Singh, and G. G. Balint-Kurti, J. Chem. Phys. **132**, 064108 (2010).

[47] M. D. Feit, J. A. Fleck, Jr., and A. Steiger, J. Comput. Phys. **47**, 412 (1982).

[48] D. Kosloff and R. Kosloff, J. Comp. Phys. **52**, 35 (1983).

[49] R. Kosloff, J. Phys. Chem. **92**, 2087 (1988).

[50] C. C. Marston and G. G. Balint-Kurti, J. Chem. Phys. **91**, 3571 (1989).

[51] P. Dutta, S. Adhikari, and S. P. Bhattacharyya, Chem. Phys. Lett. **212**, 677 (1993).

[52] G. G. Balint-Kurti, C. L. Ward, and C. C. Marston, Comput. Phys. Comm. **67**, 285 (1991).

[53] G. G. Balint-Kurti, R. N. Dixon, and C. C. Marston, Int. Rev. Phys. Chem. **11**, 317 (1992).

[54] D. T. Colbert and W. H. Miller, J. Chem. Phys. **96**, 1982 (1992).

[55] M. D. Feit and J. A. Fleck, Jr., J. Chem. Phys. **78**, 301 (1983).

[56] M. D. Feit and J. A. Fleck, Jr., J. Chem. Phys. **80**, 2578 (1984).

[57] O. Sharafeddin, R. Judson, and D. Kouri, J. Chem. Phys. **93**, 5580 (1990).

[58] G. C. Schatz and M. A. Ratner, *Quantum Mechanics in Chemistry*, Dover Publications, New York, (2002).

Chapter 3

Control of vibrational transitions in HCl

Selective preparation of states of a molecular system using optimally designed laser pulse has gained much interest in the recent past [1–6]. Such selective excitation in molecules has been explored to control bond dissociation [7–18], isomerization [19–22] and isotope selectivity [23–26]. Of late, the selectively (coherently) prepared molecular states by shaped laser pulses have been found to be useful in the area of quantum computing [28–40].

Given the general scenario related to the applications of coherently prepared molecular (specifically, vibrational) states, we present here the laser controlled vibrational transitions of a simple diatomic molecule, HCl. The general motivation is as follows. Many H-abstraction reactions in chemistry involve mostly halides like HCl, HBr and HI. They often need to undergo coherent vibrational excitation to promote the reaction efficiently. For instance the late-barrier reactions in chemistry require vibrationally hot reactant molecules to enhance the reactivity [41]. We hope that the control studies related to HCl serve well as a prototype for higher halides which participate in the kind of reactions mentioned above.

In this chapter, we have studied the controlled preparation of coherent vibrational eigenstates of HCl using optimally shaped pulses. Both fundamental

and overtone transitions of a vibration are considered for the control study. Specifically, the results of the effect of variation of penalty factor on the physical attributes of the system (i.e., probabilities) and pulse (i.e., amplitudes) considering three different pulse durations for each value of penalty factor are shown and discussed. We have employed the optimal control theory (OCT) machinery [42, 43] to obtain infrared pulses for selective vibrational transitions. The optimization of initial guess field with Gaussian envelope, phrased as maximization of cost functional, is done using conjugate gradient method [44]. The potential and the dipole moment functions used in the calculations of control dynamics are obtained from high level *ab initio* calculations. A point worth mentioning here is that obtaining the correct dipole moment function *ab initio* at large distances is difficult as one goes to higher halides. In this regard, here we were able to calculate the same for the HCl molecule and hence made use of it to study vibrational transitions. This makes the calculations more rigorous and hence more useful in shaping infrared pulses.

Our objective is to carry out the calculations of optimal pulses for controlling vibrational excitations of HCl molecule within the framework of OCT for the following transitions:

$$\mathrm{HCl}(\upsilon = 0) \rightarrow \mathrm{HCl}(\upsilon = 1)$$
$$\mathrm{HCl}(\upsilon = 0) \rightarrow \mathrm{HCl}(\upsilon = 2).$$

These calculations are done for three pulse durations, i.e., 30000 a.u., 60000 a.u. and 90000 a.u., for a given value of penalty factor.

3.1 Theory

3.1.1 Model system and *ab initio* calculations

HCl molecule in its ground electronic state is considered as the model system. Potential and dipole moment functions are shown in Fig. 3.1 and Fig. 3.2,

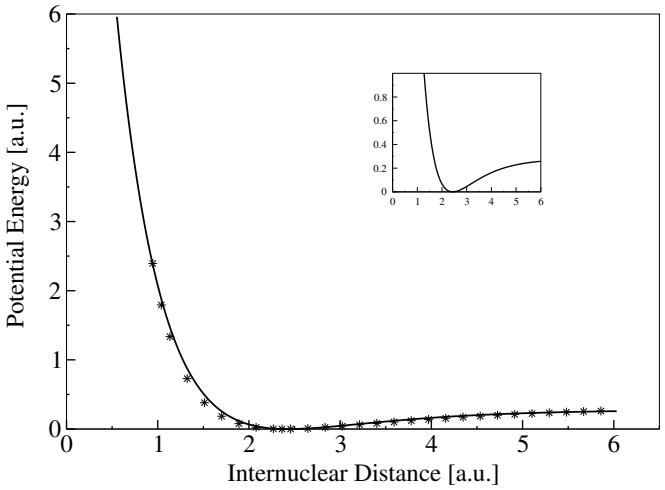

Figure 3.1: Potential Energy curve for HCl: Calculated by *ab initio* CCSD method with cc-pVTZ basis set.The solid curve represents the analytic fit to these calculated *ab initio* points [cf., Eq. (3.1)].

respectively. They are obtained by plotting the data calculated by *ab initio* CCSD method with aug-cc-pVTZ basis and CASSCF(8,8) method with aug-cc-pVTZ basis set, respectively, using Molpro suite of programme package [45]. The potential and the dipolemoment are obtained by curve fitting as follows,

$$V(R) = D_e[1 - e^{-\beta(R-R_e)}]^2, \tag{3.1}$$

where, $D_e = 0.278475$, $R_e = 2.412412037$ and $\beta = 0.918055$ in a.u., and the dipole moment function is given as

$$\mu(R) = \sum_{n=0}^{6} \mu_n R^n e^{-\sigma R^2}, \tag{3.2}$$

where, μ_0 to μ_6 1.06511, -5.2444, 10.9834, -10.7007, 5.51494, -1.43929, 0.159831, respectively, and $\sigma = 0.316883$ (in a.u.).

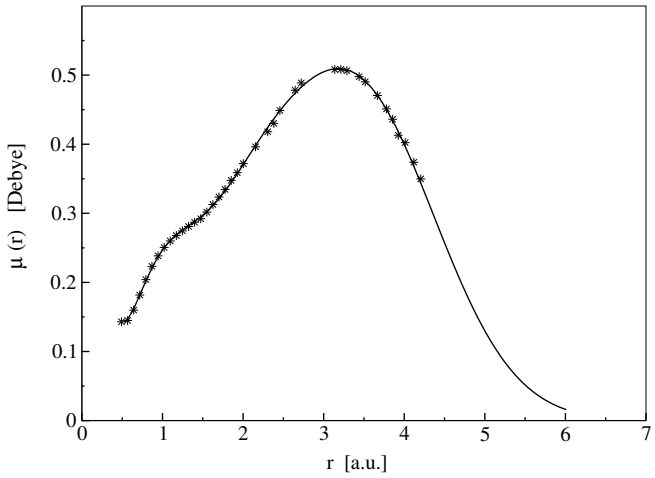

Figure 3.2: Dipole moment curve for HCl: Calculated by *ab initio* CASSCF(8,8) method with aug-cc-pVTZ basis set.The solid curve represents the analytic fit to these calculated *ab initio* points [cf., Eq. (3.2)]

.

3.1.2 1D treatment

Here, it is assumed that the HCl molecule is oriented along the polarization direction of the linearly polarized laser field. The molecular Hamiltonian and the interaction Hamiltonian due to laser-molecule interaction take the following forms,

$$\hat{H}_0 = \frac{-1}{2m}\frac{\partial^2}{\partial R^2} + V(R), \tag{3.3}$$

$$\hat{H}_{int} = -\mu(R)\cdot\epsilon(t), \tag{3.4}$$

where, $V(R)$ and $\mu(R)$ are of the form given in Eqs. (3.1) and Eq. (3.2), respectively, m is the reduced mass of HCl molecule and $\epsilon(t)$ is the electric field amplitude.

3.1.3 Theory of design of optimal pulses

We formulate the problem such that we seek a desired value of an observable at $t = T$, by applying a field. Here our objective is to maximize the population transfer from an initial vibrational state to a predefined target state by applying laser pulses designed using OCT. The time evolution of a system in the presence of a field is governed by time-dependent Schrödinger equation within semiclassical dipole approximation [46, 47]. The Hamiltonian now reads as (ignoring other noise terms)

$$\hat{H} \;=\; \hat{H}_0 - \hat{\mu}\epsilon(t), \tag{3.5}$$

where $\epsilon(t)$ and $\hat{\mu}$ are electric field of laser and electric dipole operator, respectively.

In OCT, the crucial step is to construct and optimize a cost functional, J[$\epsilon(t)$], given by

$$J[\epsilon(t)] = |\langle\psi_i(T)|\phi_f\rangle|^2 - \alpha_0 \int_0^T \epsilon(t)^2 dt - 2Re\left[\int_0^T \langle\chi_f(t)|\frac{\partial}{\partial t} + i\hat{H}|\psi_i(t)\rangle\right] \tag{3.6}$$

Here, the first term refers to the transition probability obtained by measuring the overlap between the laser driven initial wavefunction $\psi_i(t)$ and the target state ϕ_f specified at the final time T. The Second term is a penalty term for the electric field strength with the weight α_0. The last term ensures the physics of the dynamics, the time dependent Schrödinger equation (TDSE) that should be followed exactly. The function $\chi_f(t)$ can be regarded as a Lagrange multiplier function.

Each of the terms in Eq. (3.6) depends explicitly or implicitly on the unknown driving field, $\epsilon(t)$, and the goal is to maximize $J[\epsilon(t)]$ requiring, $\frac{\partial J[\epsilon]}{\partial \epsilon} = 0$. Setting the first order variations of the cost functional with respect to $\chi_f(t)$, $\psi_i(t)$, and $\epsilon(t)$ to zero yield the following nonlinear pulse design equations.

$$\frac{\partial J}{\partial \chi_f} = 0 \Rightarrow i\frac{\partial \psi_i(t)}{\partial t} = \hat{H}\psi_i(t), \psi_i(0) = \phi_i \tag{3.7}$$

$$\frac{\partial J}{\partial \psi_i} = 0 \Rightarrow i\frac{\partial \chi_f(t)}{\partial t} = \hat{H}\chi_f(t), \chi_f(T) = \langle\phi_f|\psi_i(T)\rangle|\phi_f\rangle \tag{3.8}$$

$$\frac{\partial J}{\partial \epsilon} = 0 \Rightarrow \alpha_0\epsilon(t) = -Im(\langle\chi_f(t)|\mu|\psi_i(T)\rangle) \tag{3.9}$$

The desired field can be obtained from Eq. (3.9). The Eq. (3.7) gives the evolution of the initial state in time, Eq. (3.8) gives the magnitude of $\chi(t)$ at $t = T$, and to calculate the field both are required at each point of time. In general, these coupled equations are nonlinear and hence need to be solved iteratively. The optimization is done using CG method described in chapter 2.

3.2 Results and Discussion

In this section, results for the population control of the fundamental and overtone transition of HCl molecule from its ground vibrational state to the desired target state are discussed within dipole approximation. The Fourier Grid Hamiltonian (FGH) [48–50] method is used to compute the vibrational energies and eigenfunctions of the model system. The nuclear wavefunction is represented on a one dimensional grid along the internuclear coordinate, R; its magnitude ranging from 0.530 a_0 to 6.031 a_0.

As mentioned, the initial guess laser field has the following form,

$$\epsilon(t) = E_0 \sin(\omega_{init}t) \cdot s(t), \tag{3.10}$$

where E_0 is the field amplitude and ω_{init}= (ω_f-ω_i) corresponds to the frequency for transition from the initial to target vibrational state of the HCl molecule. The factor, s(t), is a Gaussian envelope function [Eq. (2.93)] to ensure smooth decay of the pulse and preserved during the optimization to design an experimentally

feasible pulse. In Eq. (2.97), the ω_{min} and ω_{max} are set as 10 and 10000 cm^{-1}, respectively.

3.2.1 Fundamental transition: HCl($\upsilon = 0$)$\rightarrow$ HCl($\upsilon = 1$)

Here, our goal is to design a suitable pulse at three different time durations, i.e., for values of T equal to 30000, 60000 and 90000 a.u. that can selectively transfer the population from the initial vibrational state to the target vibrational state. The initial guess amplitude, E_0, and the penalty factor, α_0, are set as 0.005 a.u. and 1.0, respectively.

In Fig. 3.3 , plots a1, b1 and c1 show the optimized electric fields as a function of time for pulse durations 30000, 60000 and 90000 a.u., respectively. It is clear from the structure of the pulses, as we increase the pulse duration, the field amplitude decreases and the shape of the pulse gets broadened in the time domain which is in accordance with the pulse-area theorem [51, 52]. The associated frequency spectra for each pulse durations are shown in plots a2, b2 and c2. It is clear that the plot c2 shows sharp peak at 3447 cm^{-1} compared to plot a2 and plot b2 at their respective transition frequencies. The population transfer dynamics associated with the application of the pulse with durations 30000, 60000 and 90000 a.u., is shown in a3, b3 and c3 respectively. As time increases, the population is transfered to the target state from the initial state for three pulse durations. During the laser driven dynamics, some of the population is transfered to the $\upsilon = 2$ state, considerably for 30000 and 60000 a.u., pulse but negligibly small for 90000 a.u. pulse. However, at the end of each pulse duration 100% population transfer occurs to the target state (i.e., $\upsilon = 1$). The plots a4, b4 and c4 show the variation in transition probability and cost functional with iteration steps of optimization for each durations of pulse considered, respectively. The convergence of the algorithm is found to be faster for 30000 a.u. pulse duration. After a few steps, for application of 90000 a.u. pulse, the cost functional converges

Table 3.1: Results for fundamental transition (υ=0$\rightarrow$ υ=1) for pulse durations of 30000, 60000 and 90000 a.u. for different values of α_0: 1.0, 0.1 and 0.01. 'P' refers to the transition probability; 'J' refers to the cost functional value; ' ϵ_{peak}' refers to the value of maximum amplitude of the optimized laser field. All quantities are in atomic units.

α_0	Pulse duration (T)	P	J	ϵ_{peak}
1.00	30000	0.924	0.523	0.802×10^{-2}
	60000	0.982	0.783	0.323×10^{-2}
	90000	0.990	0.852	0.203×10^{-2}
0.10	30000	0.998	0.943	0.883×10^{-2}
	60000	0.999	0.975	0.355×10^{-2}
	90000	0.999	0.983	0.241×10^{-2}
0.01	30000	0.999	0.993	1.028×10^{-2}
	60000	0.999	0.997	0.505×10^{-2}
	90000	0.999	0.999	0.344×10^{-2}

to a value 0.85 (plot c4) which corresponds to more than 99% population transfer.

The time evolution of initial state probability densities under the action of the three pulses of duration 30000, 60000 and 90000 a.u. is shown in a5, b5 and c5, respectively, at the end of their duration. They show good overlap for 30000 and 60000 a.u. pulse and complete overlap for 90000 a.u. pulse with target probability density at the final time (T) of each pulse.

We show in Figs. 3.4 and 3.5 the effect of the penalty factor (α_0) on transition probability (P), cost functional value (J), and the field peak amplitudes (ϵ_{peak}) by varying its value 0.10 and 0.01 for the three pulse durations. The results are summarized in Table 3.1. It is observed that for $\alpha_0 = 0.01$, the three pulses of duration 30000, 60000 and 90000 a.u. are almost equally efficient in transferring population to the target state. As the time duration increases, these results follow an expected trend of decrease in field amplitudes, increase in probability densities and higher values of cost functional and its faster convergence. Exactly the same arguments would go through for α_0 value of 0.1 as that of 0.01 but with slightly less performance in driving population to the target state, comparatively.

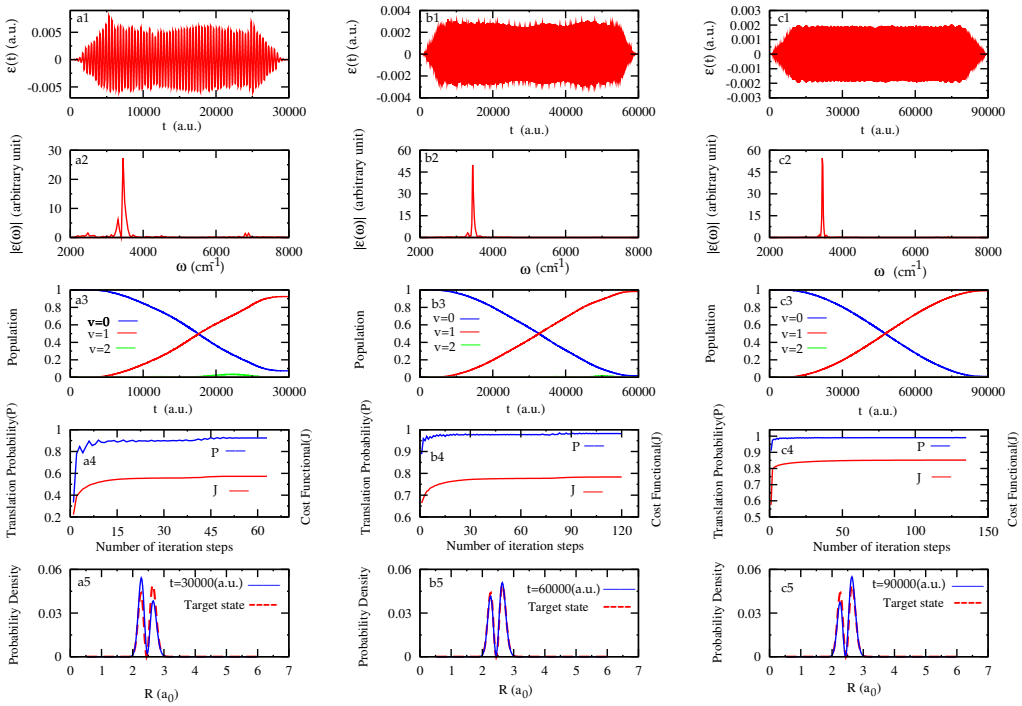

Figure 3.3: Optimized laser fields as function of time (a1, b1 and c1), frequency spectra of the optimized laser fields (a2, b2 and c2), population dynamics of vibrational states (a3, b3 and c3) and convergence of the transition probability (P) and the cost functional (J) with number of iterative steps involved in the optimization (a4, b4 and c4) are shown. Plots (a5, b5 and c5) show the overlap of laser driven evolved probability density at the end of pulse duration with the target probability density, for transition v=0→1 for pulses of duration 30000, 60000 and 90000 a.u.; α_0 is set as 1.0

.

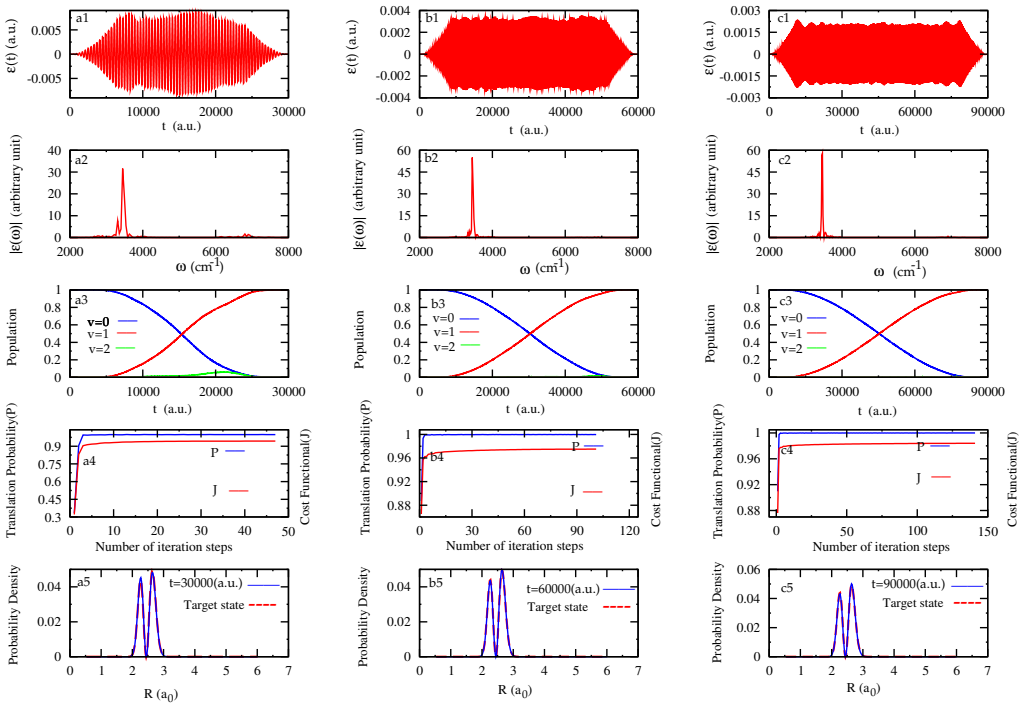

Figure 3.4: Optimized laser fields as function of time (a1, b1 and c1), frequency spectra of the optimized laser fields (a2, b2 and c2), population dynamics of vibrational states (a3, b3 and c3) and convergence of the transition probability (P) and the cost functional (J) with number of iterative steps involved in the optimization (a4, b4 and c4) are shown. Plots (a5, b5 and c5) show the overlap of laser driven evolved probability density at the end of pulse duration with the target probability density, for transition v=0→1 for pulses of duration 30000, 60000 and 90000 a.u.; α_0 is set as 0.1

.

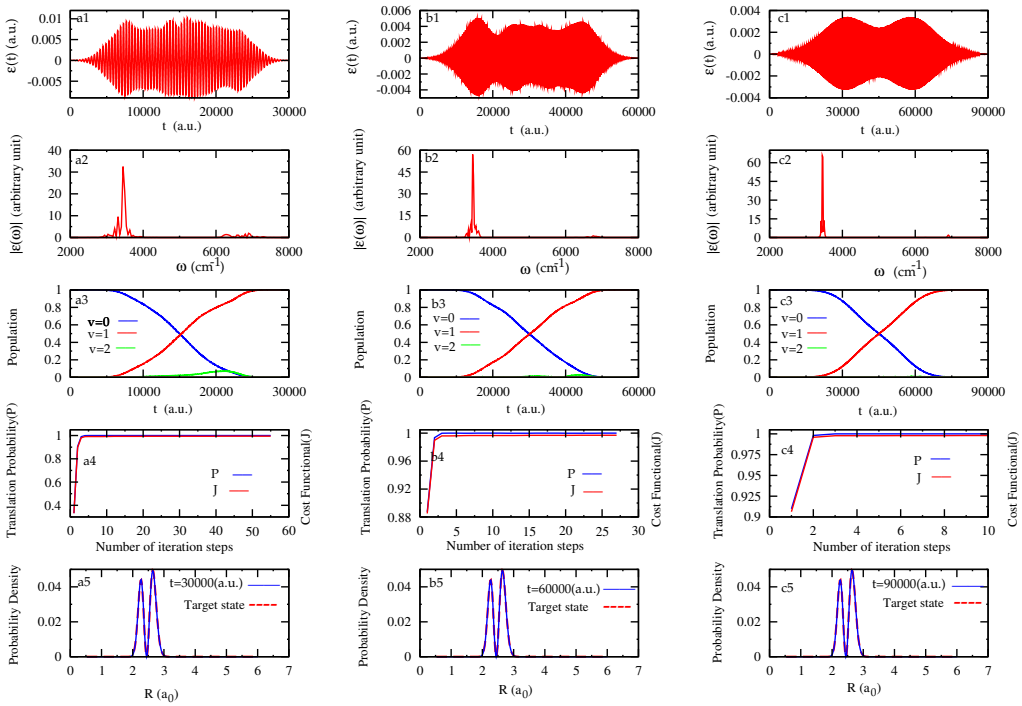

Figure 3.5: Optimized laser fields as function of time (a1, b1 and c1), frequency spectra of the optimized laser fields (a2, b2 and c2), population dynamics of vibrational states (a3, b3 and c3) and convergence of the transition probability (P) and the cost functional (J) with number of iterative steps involved in the optimization (a4, b4 and c4) are shown. Plots (a5, b5 and c5) show the overlap of laser-driven evolved probability density at the end of pulse duration with the target probability density, for transition v=0→1 for pulses of duration 30000, 60000 and 90000 a.u.; α_0 is set as 0.01

.

3.2.2 Overtone transition: HCl($\upsilon = 0$)$\rightarrow$ HCl($\upsilon = 2$)

As for the fundamental transition, here too, we aim to design suitable pulse for three different time scales of pulse duration that can achieve maximum population transfer selectively to the target state. We observed that for this transition, the penalty factor (α_0) plays a crucial role for all the three time scales in the design of optimal pulses. Here, in this case, for instance, setting penalty factor (α_0) to 1.0 with amplitude (E_0) 0.005 a.u. leads to an optimized field with secondary frequency structure and showing highly poor performance in mimicking the initial state with the target state. The results for α_0 equal to 1.0 are shown in Fig. 3.6.

As we decrease the penalty factor by a factor of 10 successively twice and run the optimization calculations, we begin to see the efficient population transfer to an intermediate state ($\upsilon = 1$) and a small amount to the higher state ($\upsilon = 3$) but a fair amount of population transfer to the target state ($\upsilon = 2$) for all three time scales. However, at the end of pulse durations the entire population is transferred to the target state. The secondary structure of the frequency spectrum for each pulse duration is fairly reduced for α_0 values (0.01 and 0.1). However, the reduction of the secondary structure of frequency is better for α_0 equals 0.01 compared to 0.1. The width of the peaks accounts for involvement of other states during population transfer dynamics. We can also observe that, as we decrease the α_0 value from 1.0, the pulse has complex temporal behaviour for all three pulse durations considered. The interesting fact observed for two α_0 values, with each involving three different time scale of the pulse is that, as the pulse duration increases the splitting of initial gaussian enveloped pulse into a train of sub pulses show that excitation with train of pulses is needed to achieve maximum population transfer to the target for overtone transition unlike in the case of fundamental transition. It is therefore clear that the pulse structure accounts for the small oscillations of population of initial and target states during the laser driven dynamics. The effect of oscillation of population is more pronounced for

Table 3.2: Results for overtone transition (υ=0→ υ=2) for pulse duration of 30000, 60000 and 90000 a.u. for different values of α_0: 1.0, 0.1 and 0.01. 'P' refers to the transition probability; 'J' refers to the cost functional value; 'ϵ_{peak}' refers to the value of maximum amplitude of the optimized laser field. All quantities are in atomic units.

α_0	Pulse duration (T)	P	J	ϵ_{peak}
1.00	30000	4.8680×10^{-12}	-9.4845×10^{-8}	0.10622×10^{-6}
	60000	5.3980×10^{-10}	-1.1048×10^{-7}	6.8567×10^{-6}
	90000	1.04212×10^{-8}	-1.6954×10^{-7}	4.985×10^{-6}
0.10	30000	0.9920	0.8385	2.43×10^{-2}
	60000	0.9991	0.9393	0.78×10^{-2}
	90000	0.9996	0.9618	0.48×10^{-2}
0.01	30000	0.9996	0.9730	2.76×10^{-2}
	60000	0.9999	0.9935	0.83×10^{-2}
	90000	0.9999	0.9959	0.51×10^{-2}

90000 a.u. pulse for both α_0 values, as is revealed by its pulse structure compared to 30000 and 60000 a.u. However, it is much more pronounced for α_0 value 0.01. The results are shown in plots of Fig. 3.7 and Fig. 3.8 for α_0 values 0.1 and 0.01 respectively.

We show in Figs. 3.7 and 3.8 the effect of penalty factor (α_0) on the transition probability (P), the cost functional (J), the field peak amplitudes (ϵ_{peak}), by varying its value (0.10 and 0.01) for three different pulse durations for each of these α_0 values. The results are summarized in Table 3.2. Here too, it is observed that for $\alpha_0 = 0.01$, the three pulses of duration 30000, 60000 and 90000 a.u. are almost equally efficient in transferring population to the target state, following a trend in the amplitudes, the cost functional convergence and the probability densities, as expected. These arguments follow same as in the control of fundamental transition.

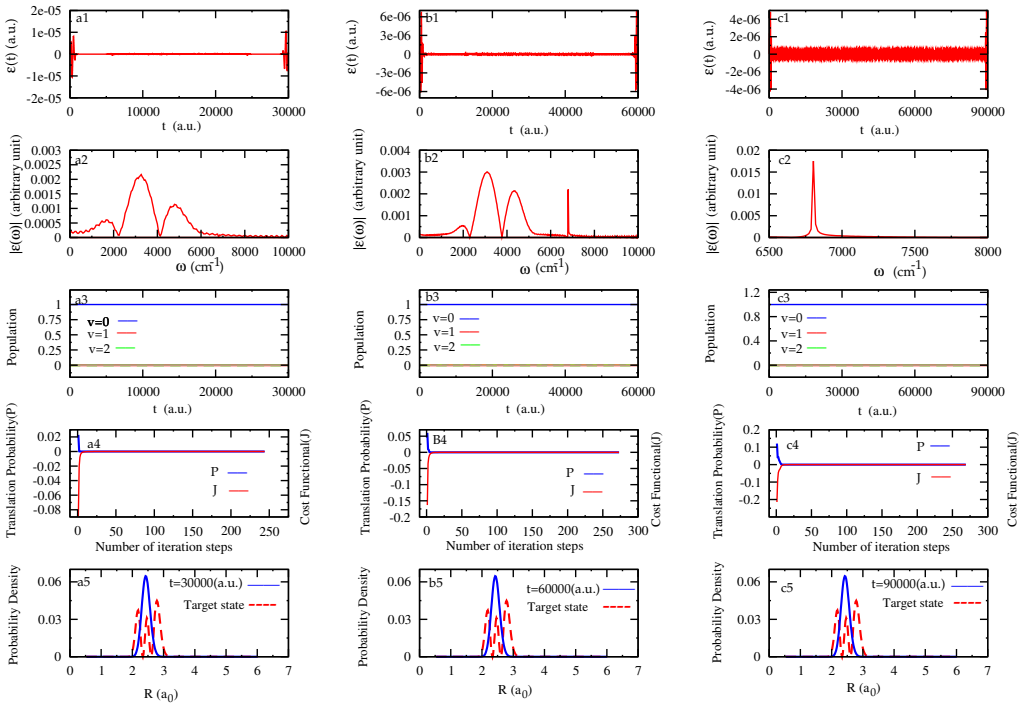

Figure 3.6: Optimized laser fields as function of time (a1, b1 and c1), frequency spectra of the optimized laser fields (a2, b2 and c2), population dynamics of vibrational states (a3, b3 and c3) and convergence of the transition probability (P) and the cost functional (J) with number of iterative steps involved in the optimization (a4, b4 and c4) are shown. Plots (a5, b5 and c5) show the overlap of laser-driven evolved probability density at the end of pulse duration with the target probability density, for transition v=0→2 for pulses of duration 30000, 60000 and 90000 a.u.; α_0 is set as 1.0

.

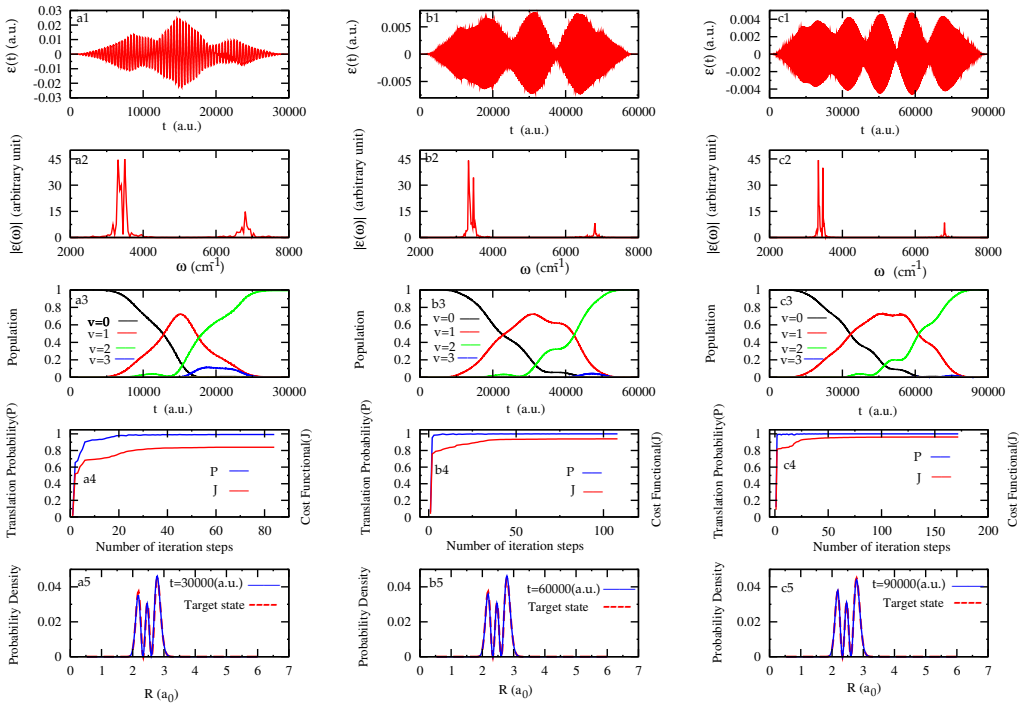

Figure 3.7: Optimized laser fields as function of time (a1, b1 and c1), frequency spectra of the optimized laser fields (a2, b2 and c2), population dynamics of vibrational states (a3, b3 and c3) and convergence of the transition probability (P) and the cost functional (J) with number of iterative steps involved in the optimization (a4, b4 and c4) are shown. Plots (a5, b5 and c5) show the overlap of laser-driven evolved probability density at the end of pulse duration with the target probability density, for transition v=0→2 for pulses of duration 30000, 60000 and 90000 a.u.; α_0 is set as 0.1

.

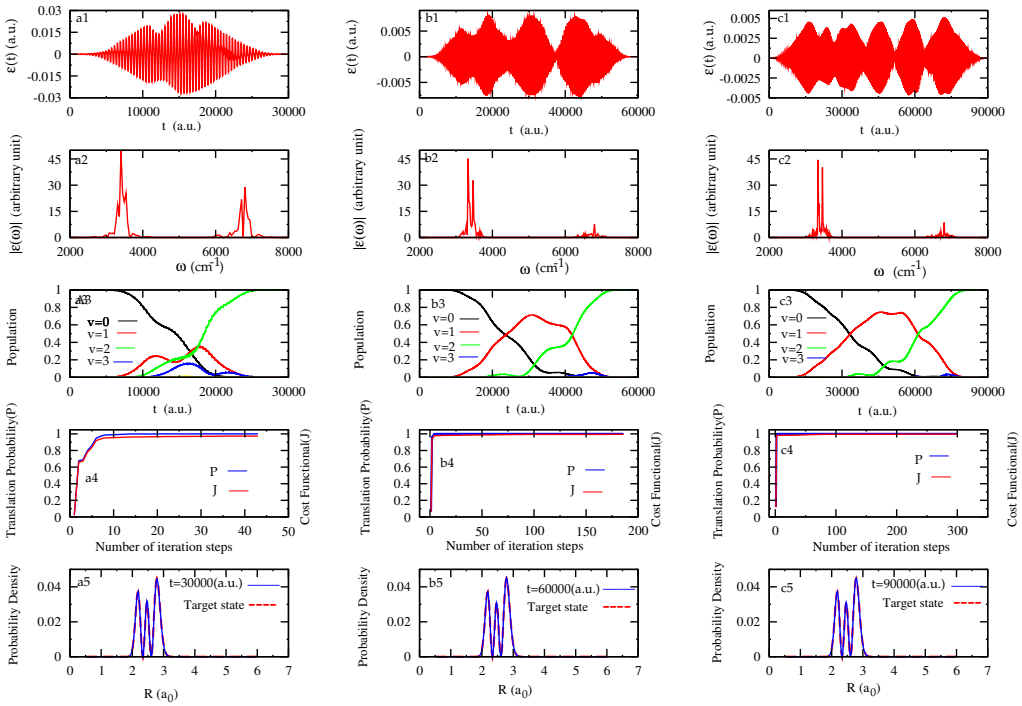

Figure 3.8: Optimized laser fields as function of time (a1, b1 and c1), frequency spectra of the optimized laser fields (a2, b2 and c2), population dynamics of vibrational states (a3, b3 and c3) and convergence of the transition probability (P) and the cost functional (J) with number of iterative steps involved in the optimization (a4, b4 and c4) are shown. Plots (a5, b5 and c5) show the overlap of laser-driven evolved probability density at the end of pulse duration with the target probability density, for transition υ=0→2 for pulse duration of 30000, 60000 and 90000 a.u.; α_0 is set as 0.01

.

3.3 Summarizing remarks

In summary, reliable optimized laser fields for the state selective population transfer using the conjugate gradient method within the theoretical framework of OCT are obtained in the present investigation. The detailed study relied on the calculated *ab initio* potential and dipole moment functions with the aid of stat-of-the-art quantum chemistry mentods. Specifically, the effect of variation of penalty factor on the physical attributes of the system (i. e., probabilities) and pulse (i. e., amplitudes) considering three differ- ent pulse durations for each value of penalty factor, is studied. As expected, we have observed that for each pulse duration considered with decrease in the value of the penalty factor α_0, the field amplitude increases. Similarly, as the pulse duration for a particular α_0 is increased, the amplitude of field decreases. Further, the examination of the results of the cost functional convergence with the variation of the penalty factor (in all cases) reveal that there is an interplay of penalty factor and amplitude term in the penalty function $(-\alpha_0 \int_0^T \epsilon(t)^2 dt)$ with former always showing a dominating role.

As the time duration for a particular α_0 is increased more iterative steps needed for the convergence of transition probabilities. It is almost 100% transfer for both the transitions at the end of each pulse duration for α_0 values of 0.1 and 0.01. The results further indicate that the shape of the optimized laser pulses and associated target yields (here transition probabilities) depend on a particular value of the penalty factor, α_0. The optimized fields obtained with smooth switch on and off behaviour are quite experimentally feasible with judicious choice of the parameters α_0, T and ϵ_{peak} as discussed in this study.

Bibliography

[1] N. Bloembergen and A. H. Zewail, J. Phys. Chem. **88**, 5459 (1984).

[2] C. D. Cantrell (Ed.), *Multi-Photon Excitation and Dissociation of Polyatomic Molecule*, Springer, Berlin, (1986).

[3] D. W. Lupo and M. Quack, Chem. Rev. **87**, 181 (1987).

[4] A. D. Bandrauk (Ed.) *Atomic and Molecular Processes with Short intense Laser Pulses*, Plenum, New York, (1988).

[5] P. Brumer and M. Shapiro, Annu. Rev. Phys. Chem. **43**, 257 (1992).

[6] A. H. Zewail, in *Femtosecond Chemsitry*, edited by J. Manz and L. Wöste, Verlag Chemie, Weinheim, **1**, 15 (1995).

[7] B. Hartke, J. Manz, and J. Mathis, Chem. Phys. **139**, 123 (1989).

[8] S. Shi and H. Rabitz, Comp. Phys. Comm. **63**, 71 (1991).

[9] W. Jakubetz, E. Kades, and J. Manz, J. Phys. Chem. **97**, 12609 (1993).

[10] M. Kaluza, J. T. Muckerman, P. Gross, and H. Rabitz, J. Chem. Phys. **100**, 4211 (1994).

[11] M. V. Korolkov, G. K. Paramonov, and B. Schmidt, J. Chem. Phys. **105**, 1862 (1996).

[12] M. V. Korolkov, J. Manz, and G. K. Paramonov, Chem. Phys. **217**, 341 (1997).

[13] I. V. Andrianov and G. K. Paramonov, Phys. Rev. A **59**, 2134 (1999).

[14] Y. Zhao and O. Kühn, Chem. Phys. Lett. **302**, 7 (1999).

[15] M. Oppel and G. K. Paramonov, Appl. Phys. B:Laser Opt. **71**, 319 (2000).

[16] R. J. Levis, G. M. Menkir, and H. Rabitz, Science **292**, 709 (2001).

[17] R. J. Levis and H. Rabitz, J. Phys. Chem. A **106**, 6427 (2002).

[18] T. Brixner and G. Gerber, Chem. Phys. Chem. **4**, 418 (2003).

[19] J. E. Combariza, J. Manz, and G. K. Paramonov, Faraday Discuss. Chem. Soc. **91**, 358 (1991).

[20] F. Großmann, L. Feng, G. Schmidt, T. Kunert, and R. Schmidt, Europhys. Lett. **60**, 201 (2002).

[21] M. Artamonov, T. -S. Ho, and H. Rabitz, Chem. Phys. **305**, 213 (2004).

[22] M. Artamonov, T. -S. Ho, and H. Rabitz, Chem. Phys. **328**, 147 (2006).

[23] Y. Ohtsuki and Y. Fujimura, Chem. Phys. **338**, 285 (2007).

[24] A. Lindinger, C. Lupulescu, M. Plewicki, F. Vetter, A. Merli, S. M. Weber, and L. Wöste, Phys. Rev. Lett. **93**, 033001 (2004).

[25] F. Vetter, M. Plewicki, A. Lindinger, A. Merli, S. M. Weber, and L. Wöste, Phys. Chem. Chem. Phys. **7**, 1151 (2005).

[26] Y. Kurosaki, K. Yokoyama, and A. Yokoyama, J. Chem. Phys. **131**, 144305 (2009).

[27] M. A. Nielsen and I. L. Chuang, *Quantum Computation and Quantum Information*, Cambridge University Press, London, (2006).

[28] C. M. Tesch, L. Kurtz, and R. de Vivie-Riedle, Chem. Phys. Lett. **343**, 633 (2001).

[29] J. Vala, Z. Amitay, B. Zhang, S. R. Leone, and R. Kosloff, Phys. Rev. A **66**, 062316 (2002).

[30] J. P. Palao and R. Kosloff, Phys. Rev. A **68**, 062308 (2003).

[31] Y. Ohtsuki, Chem. Phys. Lett. **404**, 126 (2005).

[32] B. M. R. Korff, U. Troppmann, K. L. Kompa, and R. de Vivie-Riedle, J. Chem. Phys. **123**, 244509 (2005).

[33] R. de Vivie-Riedle and U. Troppmann, Chem. Rev. **107**, 5082 (2007).

[34] D. Babikov, J. Chem. Phys. **121**, 7577 (2004).

[35] T. Cheng and A. Brown, J. Chem. Phys. **124**, 034111 (2006).

[36] S. Suzuki, K. Mishima, and K. Yamashita, Chem. Phys. Lett. **410**, 358 (2005).

[37] K. Shioya, K. Mishima, and K. Yamashita, Molec. Phys. **105**, 1283 (2007).

[38] K. Mishima, K. Tokumo, and K. Yamashita, Chem. Phys. **343**, 61 (2008).

[39] M. Tsubouchi and T. Momose, Phys. Rev. A **77**, 052326 (2008).

[40] R. R. Zaari and A. Brown, J. Chem. Phys. **132**, 014307 (2010).

[41] J. C. Polanyi, Acc. Chem. Res. **5**, 161 (1972).

[42] S. Shi and H. Rabitz, J. Chem. Phys. **92**, 364 (1990).

[43] W. Zhu, J. Botina, and H. Rabitz, J. Chem. Phys. **108**, 1953 (1998).

[44] G. G. Balint-Kurti, S. Zou, and A. Brown, Adv. Chem. Phys. **138**, 43 (2008).

[45] H. -J. Werner, P. J. Knowles, R. D. Amos, A. Bernhardsson, and others, MOLPRO-2002, a package of ab inition programs; Universitat Stuttgart: Stuttgart, Germany; University of Birmingham, United Kingdom, (2002).

[46] K. Sunderman and R. de Vivie-Riedle, J. Chem. Phys. **110**, 1896 (1999).

[47] S. P. Shah and S. A. Rice, J. Chem. Phys. **113**, 6536 (2000).

[48] C. C. Marston and G. G. Balint-Kurti, J. Chem. Phys. **91**, 3571 (1989).

[49] G. G. Balint-Kurti, C. L. Ward and C. C. Marston, Comput.Phys. Comm. **67**, 285 (1991).

[50] G. G. Balint-Kurti, R. N. Dixon and C. C. Marston, Int. Rev. Phys. Chem. **11**, 317 (1992).

[51] T. Cheng and A. Brown, J. Chem. Phys. **124**, 034111 (2006).

[52] M. Holhaus and B. Just, Phys. Rev. A **49**, 1950 (1994).

Chapter 4

Control of intramolecular H-transfer in malonaldehyde: A 2-states-1-mode model study

The H-bond is present in a variety of chemical and biological systems [1, 2] and plays an important and decisive role in their structure and reactivity. Considerable work has been done both experimentally and theoretically in order to understand the dynamics of hydrogen (H) motion [2, 3] in such systems. Among these, one of the most studied processes is intramolecular H-transfer in malonaldehyde and its derivatives [4]. The tunneling and over-the barrier transfer are the two mechanistic paths via which the proton (rather H) motion occurs in this molecule [5]. Tunneling mechanism is faciliated by the light mass of 'H' atom, relatively high barrier, low temperature and is purely a quantum effect, while barrier crossing mechanism is favored by relatively low barrier and high temperature. Among many, the details of the mechanism latter can be treated using the transition state theory (TST) approach as well [6].

In this chapter we have explored the simplest version of Tannor-Rice pump-dump scheme [7, 8] within the framework of OCT [9] for a controlled initiation of intramolecular H-transfer (HT) in malonaldehyde molecule mediated via an optically bright electronic excited state. It is noted that so far the

strategies applied for the control of H-transfer in malonaldehyde derivatives occurring in their electronic ground state [10, 11] are treated with the aid of infrared (IR)-laser pulse. In the past, the pump-dump mechanism of electronic control was much less explored compared to the vibrational control. This is due to the ease of choosing arbitrary time delay in the vibrational control processes. Furthermore, many of the studies were focussed on the control of intramolecular vibrational redistribution (IVR) and other dissipative molecular processes (in contrast to isomerization processes) occuring in picosecond time scales [12]. With the advancement of both theoretical and experimental techniques for treating electronic control with the aid of strong and short (a few cycle or sub-cycle) femtosecond pulses bypassing the competitive IVR and other dissipative phenomena (which occur in picosecond time regime) gave much scope for treating the control of molecular phenomena effectively.

Photo-isomerization of cis-malonaldehyde in the electronic ground state mediated via a bound electronic excited state is both conceptually novel and experimentally feasible. Study of such controlled isomerization process is motivated by: (a) the stronger action of transition dipole moment, $\boldsymbol{\mu(R)}$, [compared to the permanent dipole moment, $\mathbf{d}(R)$] in promoting electronic transitions, (b) the fact that an electronic excitation changes the force-field of the molecule effectively instantaneously compared to the delayed step-wise vibrational excitation, and (c) the pulse shaping technology in the UV region, which is more advanced compared to the same in the IR region. The above approach of designing optimal pulses was explored in the quantum control of Li_2Na photo-isomerization from a stable acute to the near-degenerate obtuse configuration and more recently in isomerization dynamics of semibullvalene in the electronic ground state by Manz *et al.* [13, 14]. We have adapted the pump-dump scheme mentioned in Ref. [9] and achieved, notably, significant yield of the dynamical objective with strong and short ($\sim$80 fs) optimal UV-pulses. In

our approach we use the conjugate gradient method (CG) as described in the previous chapter [15] for the optimization.

Since the HT reactions (in the electronic ground state) in these kind of systems occur on the time scale of about 60 fs [16], we set a pulse duration of 80 fs so that the pump-dump mechanism is set to complete within 60 fs. Even though the effective pumping and dumping of the wavepacket (WP) can be done at arbitrary time scales for any given total duration of the pulse, we set the duration to 80 fs so that the dynamical evolution of the system encompasses most of its possible configurations along the reaction coordinate. The smooth switching on and off of both the pump and dump pulse is ensured by time-varying gaussian envelopes. The laser driven dynamics is allowed to occur on the *ab initio* potentials of the chosen system along the reaction coordinate (ξ). The Franck-Condon excitation energy for the respective transition is obtained by *ab initio* quantum chemistry calculations. The calculated excitation energies are in good agreement with those estimated from experiment [17].

4.1 Theoretical model and techniques

The reaction coordinate of the HT process is defined as the difference between two O-H distances i.e., $\xi = R_{O_1H} - R_{O_2H}$. Constrained optimization (fixing either of R_{OH} and optimizing rest of the molecular geometrical parameters) imposing C_s symmetry followed by single point calculations have been performed for the minimum-energy-path along the reaction coordinate, ξ. The electronic structure calculations are carried out at the EOM-CCSD (equation of motion coulpled cluster singles and doubles) level of theory employing aug-cc-pVTZ (augmented version of correlation-consistent polarized valence-triple-zeta) basis set and MOLPRO suite of programs [18].

The potential energy curves for the ground S_0 (V_g) and optically bright excited S_2 ($\pi\pi^*$, V_e) electronic states and the transition dipole moment (TDM)

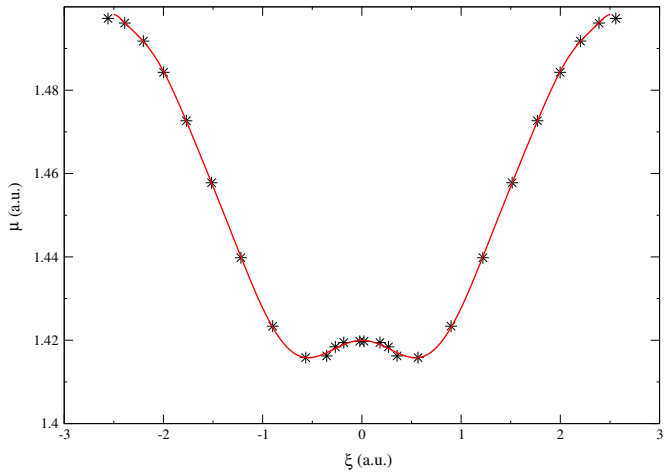

Figure 4.1: *Ab initio* calculated transition dipole moment as a function of ξ shown by the points. An analytic fit [cf. Eq. (4.3)] to these *ab initio* points is shown by the solid curve.

(μ) of malonaldehyde molecule are plotted along ξ in Fig. 4.4 and Fig. 4.1, respectively. The points in these curves represent the calculated *ab initio* data and the superimposed lines represent an analytic fit. The analytical fit equations of these quantities as functions of ξ are obtained by nonlinear least squares approach as,

$$V_g(\xi) = a_0 + \sum_{i=1}^{4} a_i \xi^{2i}, \tag{4.1}$$

$$V_e(\xi) = a_0 + \sum_{i=1}^{3} a_i \xi^{2i}, \tag{4.2}$$

$$\mu(\xi) = a_0 + \sum_{i=1}^{7} a_i \xi^{2i}. \tag{4.3}$$

where, a_i's are fit parameters and their values are given in the Table 4.1.

The associated reduced mass of the system along the coordinate ξ reads as, $2M_H M_O/(M_H + 2M_O)$. The system dynamics in the presence of field within the semiclassical dipole approximation [19, 20] is given by the Schrödinger equation as follows

$$i\hbar \frac{\partial}{\partial t} \begin{pmatrix} \psi_e \\ \psi_g \end{pmatrix} = \begin{pmatrix} \hat{H}_e & \hat{V}_{ge} \\ \hat{V}_{eg} & \hat{H}_g \end{pmatrix} \begin{pmatrix} \psi_e \\ \psi_g \end{pmatrix}, \tag{4.4}$$

Table 4.1: Fit parameters of the TDM (μ), electronic ground state (V_g) and excited state (V_e) potential energy functions [cf. Eqs. (4.1)-(4.3)].

Parameter	Value for μ	Value for V_g	Value for V_e
a_0	1.41996	0.00782249	0.169584
a_1	-0.0317928	-0.00988406	0.0123232
a_2	0.0720818	0.00366599	-0.00196209
a_3	-0.0451523	-0.00053346	0.000125813
a_4	0.0152445	0.00098584	–
a_5	-0.0028904	–	–
a_6	0.000286821	–	–
a_7	-0.0000115625	–	–

where ψ_e, ψ_g are the projections of the wavefunction (ψ) on the excited and ground state surfaces. The off-diagonal terms of the matrix Hamiltonian on the right hand side represent the interaction potential, $\hat{V}_{eg} = \hat{\mu}_{eg}\ \epsilon(t)$ and $\hat{V}_{ge} = \hat{V}^*_{eg}$. The quantity, $\epsilon(t)$, defines the time-dependent electric field component of the laser radiation.

The initial and final target WPs (they correspond to the structure I and III, respectively, drawn below the abscissa of Fig. 4.4) are approximated to a Gaussian. The initial packet is prepared at the equilibrium minimum of the reagent (I) ground state (zero of the energy scale) and the target packet (III) with its total energy, $E_g \approx 0.028 E_h$, prepared past the barrier of the ground state. The snapshots of both the WPs are shown in Fig. 4.4 and are labeled as **a** and **f** respectively. The separation in reaction coordinate (ξ) between the initial and target WPs is set to $\Delta\xi = 2.31\ a_0$. The initial and target WPs are represented by the following functional form,

$$\Psi_{init}(\xi) \approx \left(\frac{1}{2\pi\delta^2}\right)^{\frac{1}{4}} \times e^{-\frac{(\xi-\xi_{init})^2}{4\delta^2}}, \tag{4.5}$$

$$\Psi_{g,target}(\xi) \approx \Psi_{init}(\xi - \Delta\xi) \times e^{ik\xi}. \tag{4.6}$$

The values of the width parameter, δ, the location of the initial and target WPs are ξ_{init} and ξ_{target} ($= \xi_{init} + \Delta\xi$), respectively, appearing in the above equations

Table 4.2: Numerical grid parameters used in the laser-driven WP dynamics calculations.

Parameter	Value	Description
N_ξ	1024	Number of grid points
ξ_{min}/ξ_{max} (a_0)	-2.50/2.50	Extension of the grid along ξ
$\Delta\xi$ (a_0)	0.0049	Grid spacings along ξ
ξ_{init}/ξ_{target} (a_0)	-1.40/0.91	The location of the center of the initial/target Gaussian WP in the coordinate space
δ (a_0)	0.24/0.25	Initial width parameter of the initial/target Gaussian WP
Δt (a.u.)	0.10	Length of the time step used in the WP propagation
T (a.u.)	3309.89	Total propagation time

are given in the Table 4.2.

4.1.1 Design of optimal laser pulse

We formulate the problem such that we seek a desired value of an observable at time, $t = T$, by applying a field. The corresponding cost functional reads,

$$J[\epsilon(t)] = \langle\psi(T)|\hat{P}|\psi(T)\rangle - \alpha_0 \int_0^T |\epsilon(t)|^2 dt - 2Re\left[\int_0^T \langle\chi(t)|\frac{\partial}{\partial t} + i\hat{H}|\psi(t)\rangle\right]. \tag{4.7}$$

The first term in Eq. (4.7) refers to the transition probability, where $\hat{P}$ is the projection operator defined as, $|\Psi_{g,target}\rangle\langle\Psi_{g,target}|$. The second and third term are usal contraints as defined in the previous chapter [cf., Eq. (3.6) and its description]. Each of these terms depends explicitly or implicitly on the unknown driving field, $\epsilon(t)$, and the goal is to maximize $J[\epsilon(t)]$ requiring, the gradient, $\frac{\partial J[\epsilon]}{\partial \epsilon}$ = 0. Setting the first order variation of the cost functional with respect to $\chi(t)$, $\psi(t)$, and $\epsilon(t)$ to zero results the nonlinear pulse design equations as described in Chapter 2 [cf., Eqs. (2.89)-(2.91)] [21].

The laser field $\epsilon(t)$ is given by the following superposition of sinusoidal

components $\varepsilon_i(t)$,

$$\epsilon(t) = \sum_i s_i(t) \cdot \varepsilon_i(t), \tag{4.8}$$

where $s_i(t)$ is a gaussian envelope which ensures smooth decay of the field component $\varepsilon_i(t)$ at initial and final time. The envelope function $s_i(t)$ is given by

$$s_i(t) = exp\left(\frac{-(t-t_i)^2}{2\sigma_i^2}\right), \tag{4.9}$$

where t_i is the center of the pulse. The gradient of J with respect to the $\varepsilon_i(t)$ at time t after k number of iterations in the optimization cycle can be written as

$$g^k(t) = \sum_i \frac{\partial J^k}{\partial \varepsilon_i^k(t)} = -s(t)\left[\alpha_0 \epsilon^k(t) - i\left(\langle\chi_u|\frac{\partial H}{\partial \epsilon^k(t)}|\psi_g\rangle - \langle\psi_u|\frac{\partial H}{\partial \epsilon^k(t)}|\chi_g\rangle\right)\right] \tag{4.10}$$

where $s(t) = \sum_i s_i(t)$. The optimal laser pulse in this study is designed by employing the CG method explained in chapter 2.

4.2 Results and discussion

The initial guess of the laser field is approximated by the following analytic form

$$\epsilon(t) = A_0 exp[-(t-t_0)^2/2{\sigma_0}^2]\sin(\omega_0 t) + A_1 exp[-(t-t_1)^2/2{\sigma_1}^2]\sin(\omega_1 t), \tag{4.11}$$

where A_i, t_i, ω_i and σ_i represent the amplitude, time, frequency and width of the sub-pulse i [with i= 0, 1 referring to the pump, dump pulses, respectively]. The hand optimized initial guess values of these parameters are given in Table 4.3. The the shape of this hand optimized guess field and associated population dynamics are shown in Fig. 4.2.

The shape of the optimized laser pulse, $\epsilon(t)$, and the associated population dynamics are shown in panel a and b of Fig. 4.3, respectively. From panel a, it is clear that the pump pulse at 46.94 fs having a δ-function type of shape acts to transfer about ∼97% of the ground state population (panel b) through a Franck-Condon type of transition to the excited state (cf., point **b** of Fig. 4.4).

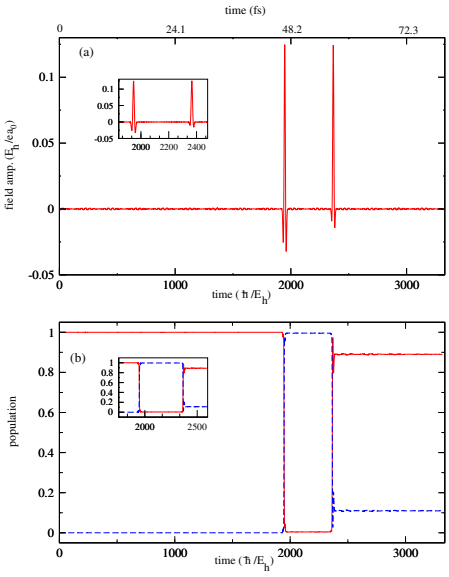

Figure 4.2: (a) Hand optimized laser field amplitude as a function of time, (b) WP population on the ground (red color thick line) and the excited (blue color dotted line) state during the action of the pump and dump pulses.

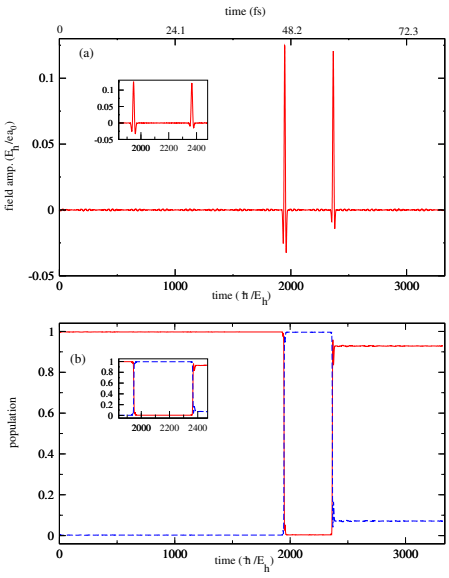

Figure 4.3: (a) Optimized laser field amplitude as a function of time, (b) WP population on the ground (red color thick line) and the excited (blue color dotted line) state during the action of the pump and dump pulses.

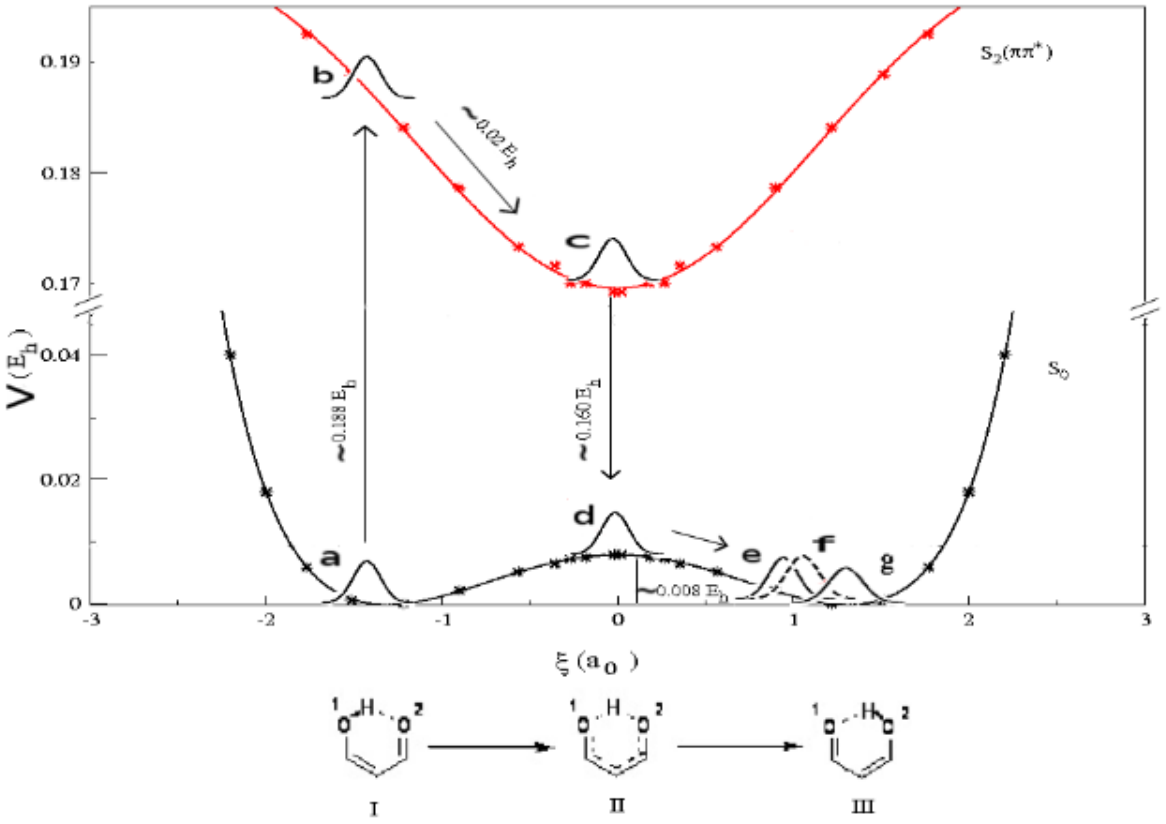

Figure 4.4: Electronic ground V_g (S_0) and excited V_e (S_2) potential energy curves of malonaldehyde plotted along the coordinate of the H-motion (ξ). The calculated *ab initio* energies and their fitting [cf., Eq. (4.1) and Eq. (4.1)] are shown by points and solid lines, respectively. The pump-dump mechanism and the associated laser driven WP dynamics is schematically shown in the diagram. The points marked **a, b, c, d, e** and **f** show probability density of the WP (schematic) on the reagent ground state (at t= 0 fs), promoted to the excited state by the pump pulse (at $t = 46.9$ fs) , time propagated laser driven WP on the excited state, WP dumped to the ground state (at $t = 57.01$ fs), time propagated laser driven WP on the ground state (at $t = 80$ fs) and the final target state located above the product well, respectively. The isomerization of malonaldehyde is illustrated by its structural change under the figure. The snapshot **g** represents the free evolution of the WP on the ground state after the end of laser pulse (i.e., $t > T$) action, which in about 2.5 fs attains the product configuration.

Table 4.3: Initial guess parameters for electric field used in the calculations.

Parameter	Value	Description
A_0/A_1 (E_h/ea_0)	0.125/0.125	initial amplitudes of the electric field
σ_1/σ_2 (a.u.)	10.0/7.14	initial widths of the pump/dump subpulses
$\omega_{min}/\omega_{max}$ (cm^{-1})	$10^3/2\times\ 10^5$	minimum/maximum of frequency range of the electric field
t_{pump}/t_{dump} (a.u.)	1943.75/2357.320	time scales of action of the pump/dump sub-pulses
α_0	0.01	penalty factor

This transferred WP, gains momentum by virtue of its location on the excited state, is then allowed to evolve on this state (cf., point **c** of Fig. 4.4) until the dump pulse (again δ-function type) acts to cause its Franck-Condon de-excitation to the ground state after a time delay of ∼10.11 fs (roughly equal to the quarter of a vibrational period on the excited state). The total energy, E_g, of the dumped WP (cf., point **d** of Fig. 4.4) consists of the kinetic energy gained from the excited state and the potential energy of the ground state at the dumping location. The dumping location of the WP and the momentum it gained from the excited state define the initial conditions for the subsequent dynamics of the WP on the ground state potential throughout the pulse duration. The dynamical mechanism involving Franck-Condon transitions during the dynamics is accompanied by the conservation of kinetic energy [cf., Eq. (4.14)]. The switching of population between the two states (as shown in panel b of Fig. 4.3) is a manifestation of the pump-dump mechanism described above. In what follows, we mention and discuss pump and dump energies, time of actions, intensity and the associated specific features of the optimal pulse.

The entire duration of the pulse action (T) is set to 80 fs for the H-transfer. The pump and dump pulses are centered around, t_{pump} ≈1941.05 a.u. (46.94 fs), and, t_{dump} ≈2359.01 a.u. (57.04 fs), respectively, with a time delay (t_d) of ∼417.96 a.u. (10.11 fs). The corresponding near-resonant photon energies for the

transitions are set closer to experimental values [17]. The latter closely correspond to the calculated potential energy gaps as shown below.

$$\hbar\omega_{pump} \approx V_e(\xi_{pump}) - V_g(\xi_{pump}) \approx 0.188E_h, \tag{4.12}$$

$$\hbar\omega_{dump} \approx V_e(\xi_{dump}) - V_g(\xi_{dump}) \approx 0.160E_h, \tag{4.13}$$

at the location, ξ_{pump} = -1.40 a_0 and ξ_{dump} = 0.01 a_0.

The optimal pump and dump pulses are shown in Fig. 4.3(a). They consist of greater than one half (pump) (i.e., 0.71 n_c) and less than one half (dump) cycle (i. e., 0.43 n_c), and hence the optimal pulse is down-chirped. The associated field amplitudes are strong with, ϵ_{max} = 0.1247 (E_h/ea_0), and the resulting intensity, $I_{max} = c\epsilon_0\epsilon_{max}^2$ = 1.37× 10^{15} W/cm^2. The width parameters, ∼10.0 a.u. (0.241 fs), ∼7.14 a.u. (0.172 fs), and full width at half maximum (FWHM) of both the gaussian shaped pump and dump pulses are set to ∼23.94 a.u. (0.57 fs), ∼17.10 a.u. (0.41 fs), respectively. The population dynamics shown in Fig. 4.3(b) clearly demonstrates that, at times close to either the maxima or minima of pulse amplitude, the effective population transfer occurs and very little or no transfer is observed for times when the amplitudes are close to zero. Although the population dynamics is very mildly affected by the small kinks at the start of the pulse (in the case of Condon approximation results, shown in supplementary material,) and at the end of it, this does not affect the underlying mechanism of pump-dump action. The optimal field profile is very similar to the guess filed. However, differences can be seen if one looks into details like the amplitudes of contributing frequencies. Overall, while the pump and dump components in the guess field were taken identical, they vary slightly in the optimal field. Consequently, the widths of the Gaussian also change. The amplitudes of the spectral components are also seen to differ significantly.

In Fig. 4.5a, the power spectrum of the optimal field obtained by the Fourier transform of the time-dependent field is shown. The observed broad frequency spectrum is a manifestation of the constructed δ-function type of pump and dump

pulses in the time domain. The sharp line structures seen in the spectrum arise from the energy difference between vibrational levels of the ground and excited state potentials which participate in the Franck-Condon transitions. The spacing between the two peaks of large intensity in the spectrum corresponds to a time period of ∼11 fs which is roughly equal to a quarter of vibrational period of the excited state (i. e., time delay between the pump and dump pulses). It is clear from the spectrum that the peak associated with dump frequency comes first with slightly less intensity than the pump frequency which follows it with a spacing of $\sim$ 2950 cm^{-1}. This is in accordance with the associated transition energies and amplitudes of the pump and dump pulses in the time domain. Since the optimal field of two sub pulses are δ - function like, the wide range frequency components in it coherently drive the transitions during pump and dump actions and these frequency components are present in the spectrum with moderate intensity on either side of pump and dump frequency. From the spectrum, it is clear that the pulse does not have a periodic structure. In Fig. 4.5b, the convergence behavior of the cost fuctional J and the transition probability P with the number of iterations is plotted and shown by the blue and red color lines. It is clear from this figure that a significant increase of the cost fuctional J and the transition probability P results from the first iteration and the values are converged for all subsequent iterations. This is due to the nature of the CG method used for the optimization which makes significant changes in the very first iteration itself and very minor changes of the field and the associated dynamics for subsequent iterations.

It is interesting to see that the entire mechanism follows kinetic energy conservation during the time delay between the pump and dump pulse, i.e.,

$$\begin{aligned} V_e(\xi_R) - V_e(\xi_{dump}) &= E_g(t_{dump}) - V_g(\xi_{dump}) \\ &\approx E_g - V_g(\xi_{dump}). \end{aligned} \tag{4.14}$$

$$E_g = E_{kin} + V_g(\xi_{target}). \tag{4.15}$$

where, $E_{kin} = \hbar^2 k^2/(2m)$ and m is the reduced mass. The value of E_g is set to

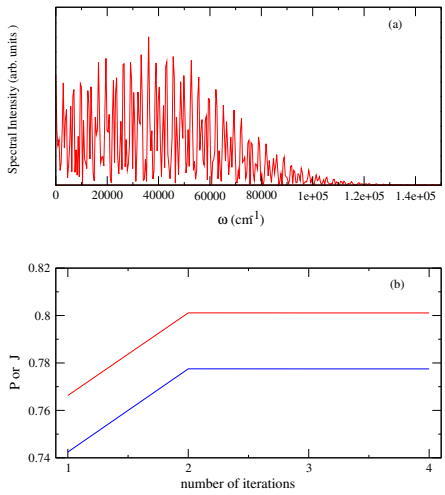

Figure 4.5: The frequency spectrum of the optimized laser fields plotted in panel a. In the panel b the convergence behavior of the transition probability (P) and the cost functional (J) with respect to number of iterations in the conjugate gradient method shown by the red and blue color lines, respectively.

be approximately 0.028 E_h in accordance with the dumping location at, $\xi = 0.01$ a_0. The time delay of ∼417.96 a.u. (10.11 fs), i. e., from pump time (t_{pump}) ∼ 1941.05 a.u. (46.93 fs) to dump time, (t_{dump}) ∼2359.01 a.u. (57.04 fs), is the time in which the WP $\Psi_e(\xi, t)$ propagates on the excited state from ξ_{pump} = -1.40 a_0 to $\xi_{dump} = 0.01$ a_0, gaining momentum due to the steep repulsive nature of this part of excited electronic state (cf., Fig. 4.4). It is obvious that during propagation the spreading and dephasing of WP occurs. However, owing to an extremely short nature of the pulse (∼80 fs) acting on it, near coherent excitation and de-excitation of the WP takes place. An overlap of ∼80% with the target state at the end of the pulse duration (around ∼80 fs) is obtained. The snapshots of the laser driven WP probability densities on both the ground (shown in red color) and excited (shown in green color) states are shown at different times in Fig. 4.6. Panels a1 and a2 of the figure represent the evolution of WP probability density on the ground state until the action of pump pulse occurs. Panels a3 and

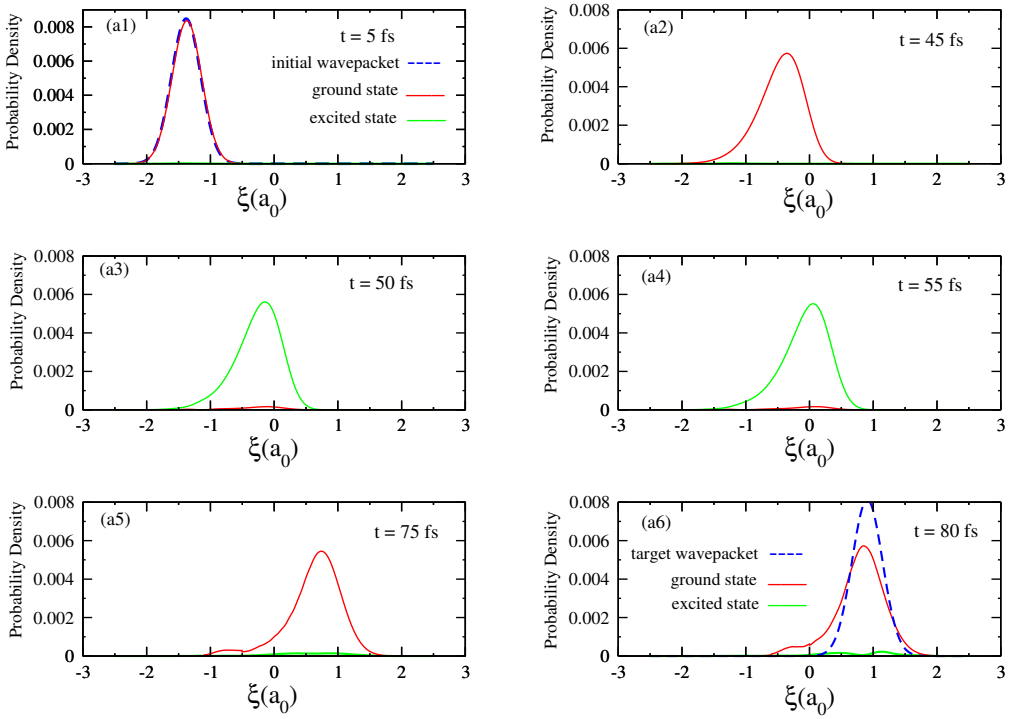

Figure 4.6: Snapshots of the laser driven WP dynamics on the ground (shown in red color) and excited state (shown in green color) in terms of probability densities of WP components at different times (indicated in the respective panel) are shown.

Table 4.4: Initial guess parameters for the electric field used in the calculations using CDA.

Parameter	Value	Description
A_0/A_1 (E_h/ea_0)	0.4250/0.4250	initial amplitudes of the electric field
σ_1/σ_2 (a.u.)	7.13692946/7.13692946	initial widths of the pump/dump subpulses
$\omega_{min}/\omega_{max}$ (cm^{-1})	10^3/2x10^5	minimum/maximum of frequency range of the electric field
t_{pump}/t_{dump} (a.u.)	1943.75/2357.320	time scales of action of the pump/dump sub-pulses
α_0	0.1	penalty factor

a4 show the evolution of the WP probability density on the excited state after the action of pump pulse at ∼46.94 fs (the time at which maximum probability density is transferred to the excited state). Subsequent evolutions to reach the target state (dotted blue curve in the panel a6) on the ground state after the action of dump pulse at ∼57.04 fs (the time when the probability density of the excited state is dumped back almost completely to the ground state) is shown in panels a5 and a6 of the figure. It is seen from the figure that the probability densities evolve forward in time, by the positive momentum gained, from the excited state potential and reaches the target located in the ground state at the end of the pulse. For the better overlap (shown in panel a6) at the end of the pulse duration, the initial (blue-dotted line shown in panel a1) and target WP widths taken slightly differently as mentioned in the Table 4.2.

We have also examined the difference of the dynamics within constant dipole approximation (CDA) (taking μ=0.4 a.u.) to that using *ab initio* calculated transition moment function (TMF) discussed above. The initial guess parameters for the field are given in Table 4.3 for the former case and in Table 4.4 for the latter case. For the CDA case, the field parameters are changed in two respects, (a) increase in the amplitude of the initial guess field and (b) decrease in the width of pump pulse. The figures 4.7-4.9 are drawn parallel to those obtained in the

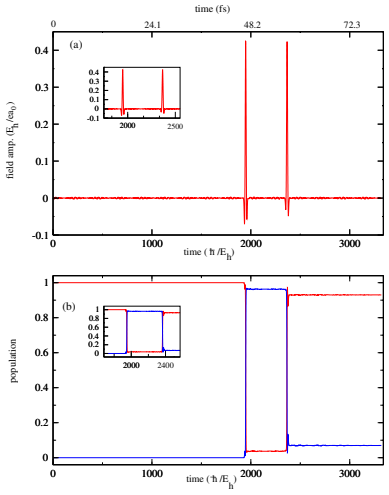

Figure 4.7: (a) Hand optimized laser field amplitude as a function of time, (b) wave packet population on the ground (red color thick line) and the excited (blue color dotted line) state during the action of the pump and dump pulses.

earlier case using the *ab initio* TMF. It is clear that the optimal field amplitudes [cf., Fig. 4.8(a)] differs slightly in numerical values from the corresponding results using TMF discussed earlier. Nevertheless, the field exhibits the same effect on the system dynamics as in the TMF case except in this case is the population transfer somewhat better. This is a result of action of high energy content of the field. The change from TMF to CDA case does not have a significant impact on the fluence term indicating that there is an interplay between the field amplitude and and the penalty factor. The changes made initially evolve such that fluence remains constant. This follows the pulse-area theorem [27, 28] also. The laser driven population dynamics [cf., Fig. 4.8(b)], the convergence behavior of the transition probability (P) and the cost functional (J) [cf., Fig. 4.8(c)] show more or less the same behavior as for the TMF case. The figure 4.9 demonstrates the laser driven WP probability densities along the same line as discussed above for the case of *ab initio* TMF used dynamical calculations.

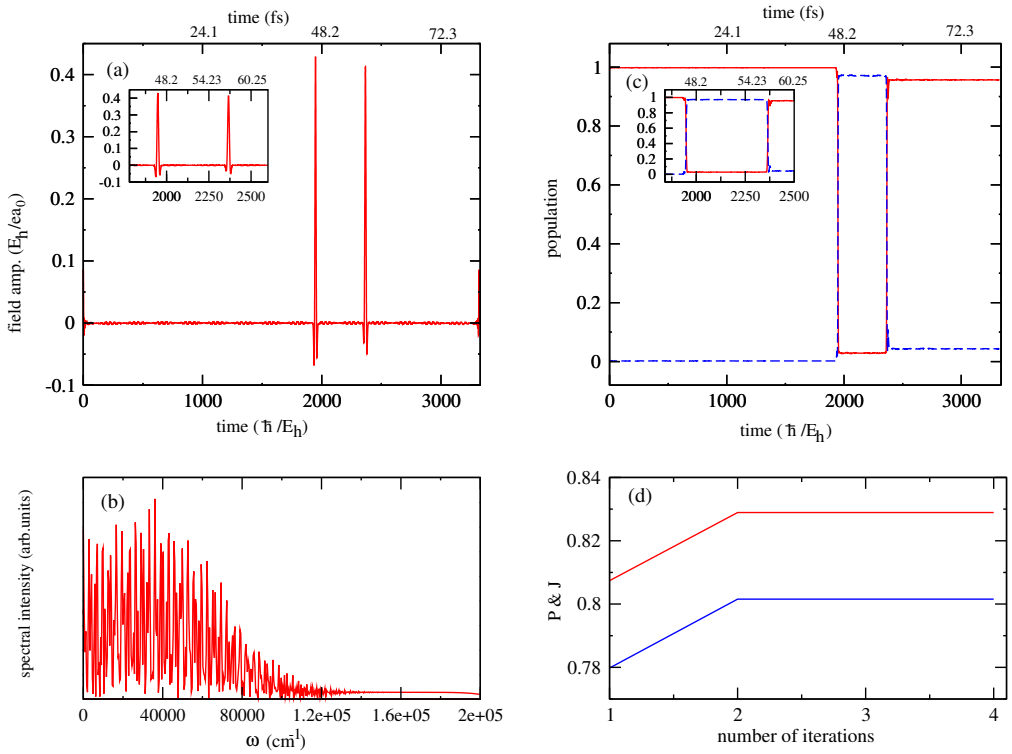

Figure 4.8: The optimized laser field amplitude as function of time (a), population dynamics of ground and excited states (b), frequency spectrum of the optimized laser field (c) and convergence of the transition probability (P) and the cost functional (J) with respect to the number of iterations involved in the optimization (d) for the ground and excited state transitions are shown.

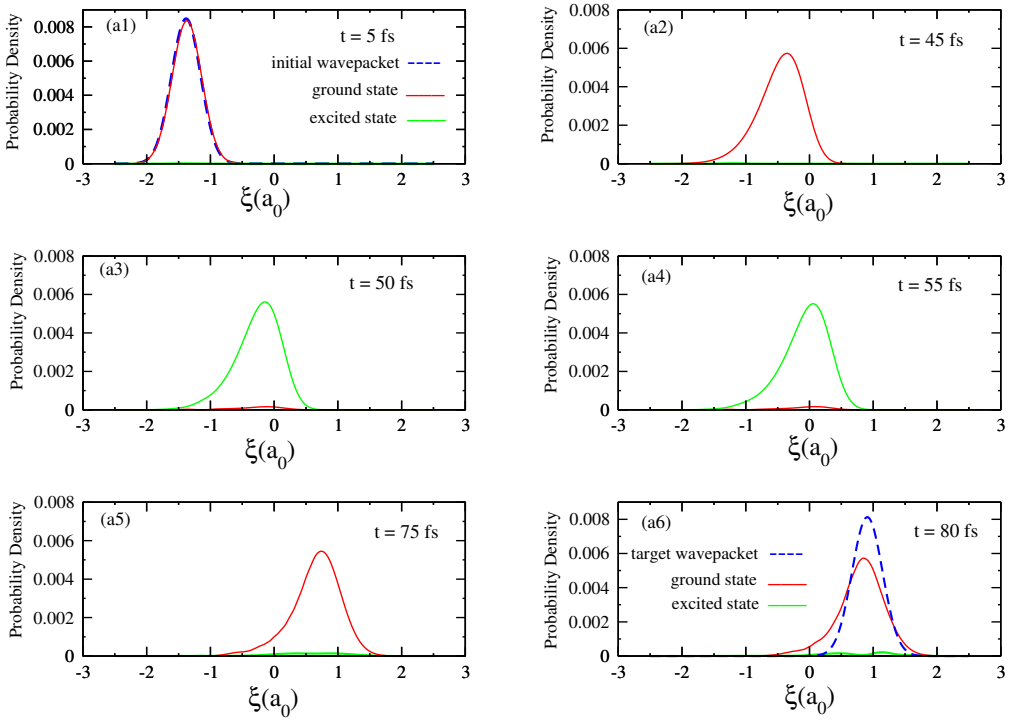

Figure 4.9: Snapshots of the laser driven WP dynamics on the ground (shown in red color) and excited state (shown in green color) in terms of evolution of the probability densities of WP components at different times (indicated in the respective panel) are shown.

4.3 Summarizing remarks

We have designed the ultrashort down-chirped pump-dump pulse(s) using the Tannor-Rice scheme implemented in OCT for achieving controlled initiation of H-transfer in the ground state mediated by electronic excited state. The optimal pulse(s) is short and strong. Because of the complete population transfer between the two electronic states, there is no room for occurrence of competitive tunneling dynamics during the control. The left over WP components are minimal after near-resonant excitation and de-excitation in both the ground and excited state. Hence ∼93% (and ∼95% within CDA) final population transfer to the ground state is achieved by the pump-dump pulse.

It is possible to achieve the task of controlled initiation of H-transfer in the ground state of cis-malonaldehyde by the application of an optimal pulse designed using optimal pump-dump approach in the present model. This task ensures the product formation with good yield. This happens for both the cases of dynamical calculations (i. e., within CDA and taking *ab initio* TMF). The dynamical results in which CDA is used are slightly better than those obtained using *ab initio* TMF. The more or less good agreement in the results for the two cases serves as an illustration to check or confirm the validity of CDA. Hence we conclude that for the problems involving electronic transitions in 1D the CDA is fairly a good approximation to use.

The excited state used in the process acts as a mediator, changes the force field and providing momentum to the WP to move towards product side. The convergence of optimization is also rapid. The importance of optimization is evident by the enhancement in dumping of population by about ∼5% by the optimal field compared to hand optimized initial field.

Bibliography

[1] D. Hadži (ed.), *Theoretical treatments of hydrogen bonding*, John Wiley and Sons, Chichester, (1997).

[2] J. T. Hynes, J. P. Klinmen, R.L. Schowen (eds.), *Hydrogen transfer reactions*, Wiley-VCH, Weinheim, (2006).

[3] N. Došlić, Y. Fujimura, L. González, K. Hoki, D. Kröner, O. Kühn, J. Manz, and Y.Ohtsuki, in F. C. De Feyter, G. Schweitzer (eds.), *Femtochemistry*, VCH-Wiley, Berlin, 189 (2001)

[4] N. Došlić, O. Kühn, J. Manz, and Ber. Bunsenges. Phys. Chem. **102**, 292 (1998).

[5] N. Došlić, O. Kühn, J. Manz, and K. Sundermann, J. Phys. Chem. A **102**, 9645 (1998).

[6] B. Saritha and M. Durgaprasad, J. Phys. Chem. A **115**, 2802 (2001).

[7] D. J. Tannor and S. A. Rice, J. Chem. Phys. **83**, 5013 (1985).

[8] D. J. Tannor and R. Kosloff, S. A. Rice, J. Chem. Phys. **85**, 5805 (1986).

[9] R. Kosloff, S. A. Rice, P. Gaspard, S.Tersigni, and D. J. Tannor, Chem. Phys. **139**, 201 (1989).

[10] K. Nishikawa, Y. Ohta, T. Yoshimoto, T. Saito, K. Nishi, and H. Nagao, J. Mol. Struct. **615**, 13 (2002).

[11] N. Došlić, O. Kühn, J. Manz, and K. Sundermann, J. Phys. Chem. A **102**, 9645 (1998).

[12] M. V. Korolkov, J. Manz, and G. K. Poromonov, J. Chem. Phys. **105**, 24 (1996)

[13] J. Manz, K. Sundermann, and R. de Vivie-Riedle, Chem. Phys. Lett. **290**, 415 (1998).

[14] T. Bredtmann and J. Manz, J. Chem. Sci. **124**, 121 (2012).

[15] W. H. Press, S. A. Teukolsky, W. T. Vetterling, and B. P. Flannery, *Numerical Recipes in FORTRAN*, Cambridge University Press, London, (2000).

[16] J. L. Herek, S.Pedersen, L. Banares, and A. H. Zewail, J. Chem. Phys. **97**, 9046 (1992).

[17] C. J. Seliskar and R. E. Hoffmann, Chem. Phys. Lett. **43**, 481 (1976).

[18] H. -J. Werner, P. J. Knowles, and R. D. Amos, A. Bernhardsson, others, MOLPRO-2002, a package of ab inition programs; Universitat Stuttgart: Stuttgart, Germany; University of Birmingham, United Kingdom, (2002).

[19] K. Sunderman and R. de Vivie-Riedle, J. Chem. Phys. **110**, 1896 (1999).

[20] S. P. Shah and S. A. Rice, J. Chem. Phys. **113**, 6536 (2000).

[21] S. A. Rice and M. Zhao, *Optical control of Molecular Dynamics*, Wiley Interscience, New York, (2000).

[22] M. D. Feit and J. A. Fleck, Jr., J. Chem. Phys. **78**, 301 (1983).

[23] M. D. Feit and J. A. Fleck, Jr., J. Chem. Phys. **80**, 2578 (1984).

[24] E. Polak, *Computational Methods in Optimization, Mathematics in Science and engineering*, Academic Press, New York, (1971).

[25] E. G. Birgin, J. M. Martinez, and M. Raydan SIAM J. Optim. **10**, 1196 (2000).

[26] P. Gross, D. Neuhauser, and H. Rabitz, J. Chem. Phys. **96**, 2834 (1992).

[27] M. Holhaus, and B. Just, Phys. Rev. A **49**, 1950 (1994).

[28] T. Cheng and A. Brown, J. Chem. Phys. **124**, 034111 (2006).

Chapter 5

Control of intramolecular H-transfer in malonaldehyde: A 3-states-2-modes model study

It is clear from the model used in chapter 4 for control studies that in malonaldehyde, the electronic ground state (S_0) possesses a barrier to H-transfer whereas the optically bright ($^1\pi\pi^*$) S_2 state is free of any barrier, along the reaction coordinate, ξ. There exists also an intermediate symmetry-forbidden ($^1n\pi^*$) S_1 state between S_0 and S_2 states. This state is known to play a crucial role in controlling H-transfer after initial excitation to the optically bright S_2 state [1, 2] as it forms CIs with the latter near its transition state region. In the Franck-Condon region, the optically bright S_2 state lies above the dark S_1 state [cf., Fig. 5.1(c)]. The barrier to H-transfer in the latter increases (nearly 3 times) as compared to that in S_0 (which is 0.008 E_h). This is because the electron density on oxygen of the carbonyl group (the acceptor in H-transfer process) depletes as a result of the $^1n\pi^*$ excitation, leading to weak H-bonding. The interaction of the bright S_2 state and the ($^1n\pi^*$) S_1 state is very important as it leads to coupling of H-transfer with electronic de-excitation [1, 2]. A more rigorous model should necessarily take such nonadiabatic interactions into account. Therefore, here we consider the inclusion of $^1n\pi^*$ state in the dynamical control mechanism of

H-transfer in malonaldehyde.

The aim of the present study is to extend the model study of chapter 4 in order to examine as to what extent laser-driven H-transfer can be achieved in a situation which includes nonadiabatic interactions between electronic states. In the chapter 4, we have explored the simplest version of Tannor-Rice pump-dump scheme [3, 4] within the framework of OCT [5] using CG method for a controlled initiation of intramolecular H-transfer in malonaldehyde molecule mediated via an optically bright excited state (S_2). In this chapter, the same control task with a higher-order model that includes the above mentioned three electronic states (that is S_0, S_1 and S_2) with a coupling between the excited potentials (S_1 and S_2) and two modes (a tuning coordinate, ξ, and coupling coordinate, Q_7) of the malonaldehyde, is considered. These coordinates are defined in Fig. 5.1. Because of coupling between the excited states, the two potentials in the vicinity of the interaction region exhibit complicated topography [cf., Fig. 5.1(c)]. As the PESs are not simple enough to allow us to use a simple pump and a time-delayed dump pulse for achieving successful control of isomerization in the ground state, one should rely on a mechanism that involves a constant pump followed by a dump operation with a pulse in action (as suggested in introductory remarks of the section **1.1.2**). This obviously enables the continuous electronic transitions in order to reshape and subsequently direct the WP to the desired location on the excited states so that the population flow to the desired product channel in the ground state could be achieved.

We therefore have designed an optimal laser pulse that has temporally and spectrally shaped field using OCT framework in combination with GA optimization technique for successfully achieving the yield of the product isomer in the ground state mediated by excited electronic states interacting nonadiabatically. The reason for the choice of GA over CG method for optimization is a) to make the model more realistic so that it can synthesize

practically realizable laser pulses and b) it has numerically stable global search algorithm. In this work, we have set 200 fs as the time duration of the pulse. This time scale is found to be sufficient for maximum population transfer between electronic states and for the excursion of the WP components over the entire region of PESs.

5.1 Theoretical model and techniques

The reaction coordinate, ξ, of the H-transfer process is taken as the difference between two O-H distances i. e., $\xi = R_{O_1H} - R_{O_2H}$. The potentials along this coordinate are constructed using constrained optimization as discussed in chapter 4. The coupling coordinate, Q_7, describes the out-of-plane bending motion of O-H. For simplicity we refer Q_7 as Q hereafter. The normal mode corresponding to the dimensionless normal coordinate Q_7 is calculated at the equilibrium geometry of the ground electronic state see Fig. 5.1(a). Pictorially, the two coordinates are shown in Fig. 5.1. The potential energies as functions of these two coordinates are obtained at the same level of theory as in chapter 4. These energy plots for the ground S_0, and the excited S_1 ($^1n\pi^*$) and S_2 ($^1\pi\pi^*$) electronic states along these coordinates are shown in Fig. 5.1.

The diabatic potentials and their coupling potentials are calculated based on the *ab initio* potential energy values as suggested in chapter 2. The analytical fit equations of these quantities as functions of ξ and Q are obtained by using Levenberg Marquardt algorithm as implemented in MATLAB [6] as,

$$U_g(\xi, Q) = a_0 + \sum_{i=1}^{3} a_i \xi^{2i} + (a_0 + a_1\xi^2)Q^2, \tag{5.1}$$

$$U_{e1}(\xi, Q) = a_0[1 - exp(-a_1(\xi + 1.94))]^2 + a_2Q^2 + a_3\xi Q + a_4, \tag{5.2}$$

$$U_{e2}(\xi, Q) = a_0[1 - exp(-a_1(\xi - 1.94))]^2 + a_2Q^2 + a_3\xi Q + a_4, \tag{5.3}$$

$$U_{e1e2}(\xi, Q) = \lambda(\xi)Q = \left(a_0 + \sum_{i=1}^{3} a_i \xi^{2i}\right)Q, \tag{5.4}$$

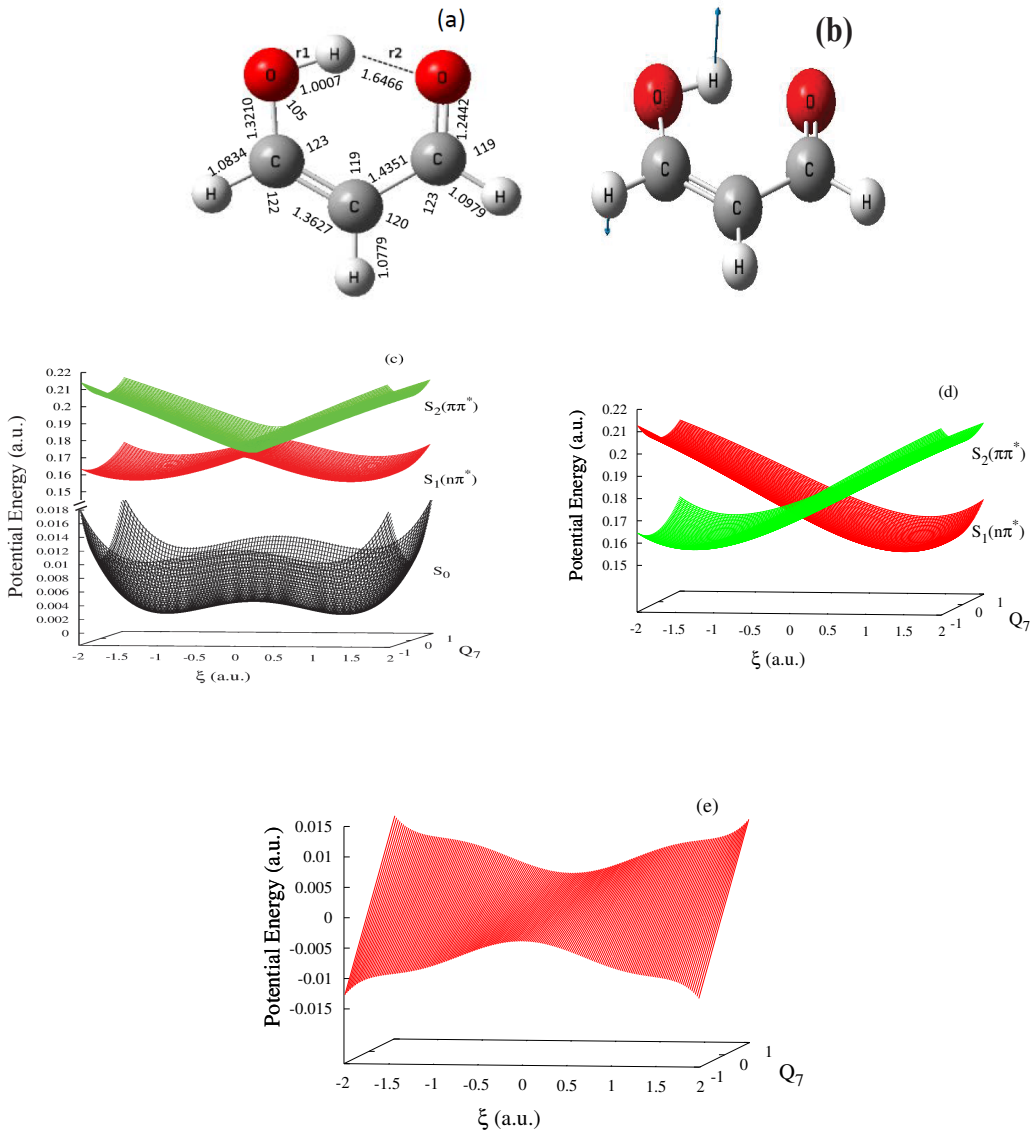

Figure 5.1: The potential energies of S_0, $S_1[^1B_1(n\pi^*)]$ and $S_2[^1B_2(\pi\pi^*)]$ along the ξ (reaction coordinate, represents the difference of OH distances $(r1 - r2)$ shown in (a)) and Q (dimensionless coupling coordinate (b)) in the adiabatic (c) electronic representation. The corresponding diabatic potential energies of the coupled $^1B_1(n\pi^*)$ and $^1B_2(\pi\pi^*)$ states along with the associated diabatic coupling (U_{e1e2}) are shown in panels (d) and (e), respectively.

Table 5.1: Fit parameters of the potential energy functions of Eqs. (5.1)-(5.3)

.

Parameter (eV/a_0)	Value for U_g	Value for U_{e1}	Value for U_{e2}	Value for U_{e1e2}
a_0	0.1956	3.5240	3.5240	0.0979
a_1	0.0277	0.2689	0.2689	0.1741
a_2	-0.1283	0.2187	0.2187	-0.0707
a_3	0.03062	-0.0473	0.0473	0.0109
a_4	–	4.1670	4.1670	–

where, λ is a linear inter-state coupling parameter and a_i's are the fit parameters and their values are given in the Table 5.1.

The system dynamics in the presence of field within the semiclassical dipole approximation [7, 8] is given by the Schrödinger equation as follows

$$i\hbar\frac{\partial}{\partial t}\begin{pmatrix}\psi_{e2}\\ \psi_{e1}\\ \psi_g\end{pmatrix} = \begin{pmatrix}\hat{H}_{e2} & \hat{W}_{e2e1} & \hat{W}_{e2g}\\ \hat{W}_{e1e2} & \hat{H}_{e1} & \hat{W}_{e1g}\\ \hat{W}_{ge1} & \hat{W}_{ge2} & \hat{H}_g\end{pmatrix}\begin{pmatrix}\psi_{e2}\\ \psi_{e1}\\ \psi_g\end{pmatrix}, \tag{5.5}$$

where ψ_{e2}, ψ_{e1} and ψ_g are the projections of the wavefunction (ψ) on the excited states S_2, S_1 and ground state surfaces, respectively. The operator $\hat{H}_{g/e1/e2}$ reads,

$$\hat{H}_{g/e1/e2} = -\frac{\hbar^2}{2m}\frac{\partial^2}{\partial\xi^2} - \frac{1}{2}\omega\frac{\partial^2}{\partial Q^2} + \hat{U}_{g/e1/e2}, \tag{5.6}$$

where, $m = 2\mathrm{M}_H\mathrm{M}_O/(\mathrm{M}_H{+}2\mathrm{M}_O)$ is the reduced mass along ξ (M_H and M_O denote the mass of the hydrogen and oxygen atoms, respectively) and $\omega = 855$ cm^{-1}, is the frequency of the coupling vibrational mode Q. The off-diagonal terms of the matrix Hamiltonian on the right hand side of Eq. (5.5) represent the interaction potential, $\hat{\mu}_{ge1/ge2/e1e2}\cdot\epsilon(t)$, plus the diabatic coupling, $\hat{U}_{ge1/ge2/e1e2}$, i.e., $\hat{W}_{ge1/ge2/e1e2} = \hat{\mu}_{ge1/ge2/e1e2}\cdot\epsilon(t){+}\hat{U}_{ge1/ge2/e1e2}$. Where $\hat{W}_{ge1/ge2/e1e2} = \hat{W}^*_{e1g/e2g/e2e1}$ and $\hat{U}_{ge1/ge2} = 0$. The quantity, $\epsilon(t)$, defines the time-dependent electric field of the laser pulse. We treat the transition dipole moment operator $\hat{\mu}_{eg}$ within the constant dipole approximation (CDA) for numerically solving the three states TDSE. Moreover, the CDA is a valid approximation in a

Table 5.2: Numerical grid parameters used in the present calculations.

Parameter	Value	Description
N_ξ/N_Q	256/128	Number of grid points
ξ_{min}/ξ_{max} (a_0)	-2.50/2.50	Extension of the grid along ξ
Q_{min}/Q_{max}	-15.0/15.0	Extension of the grid along Q
$\Delta\xi$ (a_0)	0.0196	Grid spacings along ξ
ΔQ	0.2362	Grid spacings along Q
Δt (a.u.)	1.0098	Length of the time step used in the WP propagation
T (a.u.)	8271.29 (200 fs)	Total propagation time

diabatic electronic basis [9] as the electronic character of the states is retained throughout the nuclear coordinate space in this basis. Numerically, the Fourier transformation method is used to evaluate the action of kinetic energy operators of the Hamiltonian on the wavefunction and the time propagation is carried out by a second order split-operator method [10, 11] adapted to coupled electronic states [12, 13]. The numerical values of the parameters used in the dynamical calculations are presented in Table 5.2.

The initial and final target wavefunctions are given as $|0,0\rangle$ wavefunction (for nomenclature see below) in the left and right well of the ground S_0 state, respectively. These wavefunctions are calculated by using the Fourier grid hamiltonian (FGH) method [14–16]. Some of the wavefunctions are plotted in Fig. 5.2 and the associated vibrational energies are given Table 5.3. As can be seen from the figure and table that the wavefunctions are degenerate which is a reflection of the fact that potential has symmetric wells. The wavefunctions are designated in terms of number of nodes along ξ and Q as $|n_\xi, n_Q\rangle$.

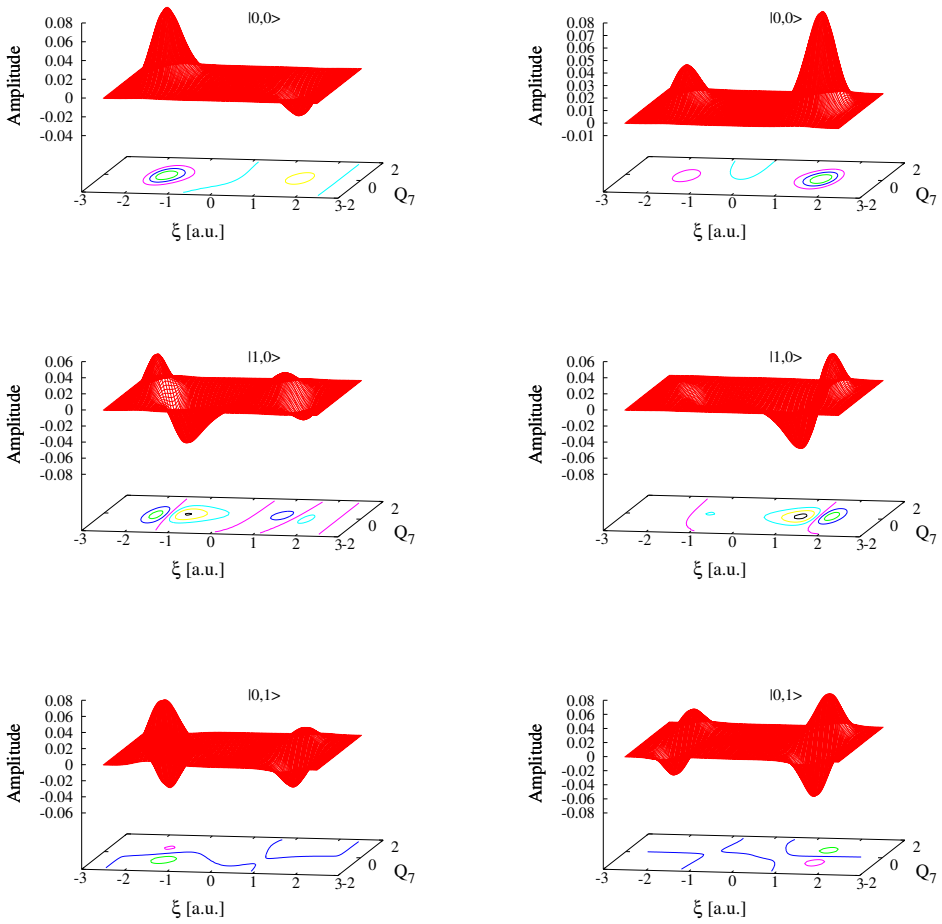

Figure 5.2: Wavefunctions of the electronic ground state (S_0) of malonaldehyde. Wavefunctions are labeled according to the number of nodal lines along ξ and Q coordinates and designated as, $|n_\xi, n_Q\rangle$ representing number of quanta along these coordinates. The wavefunctions in the left and right columns belong to the reactant and product well, respectively.

Table 5.3: The calculated energy eigenvalues for eigenfunctions labeled by $|n_\xi, n_Q\rangle$ in the electronic ground state (S_0).

Energy (cm^{-1})	$\|n_\xi, n_Q\rangle$	Energy (cm^{-1})	$\|n_\xi, n_Q\rangle$
718	$\|0,0\rangle$	3795	$\|1,1\rangle$
1861	$\|1,0\rangle$	3815	$\|2,1\rangle$
1882	$\|2,0\rangle$	4584	$\|0,2\rangle$
2650	$\|0,1\rangle$	5728	$\|1,2\rangle$

The present objective involves maximization of the product yield (in terms of its population) on the ground electronic state. The portions of the WP located on the product (prod) and reactant (react) configurations for the ground ($i = g/S_0$) and excited states ($i = e1/S_1$ and $e2/S_2$), at a given time, are quantified by the populations,

$$Y_{prod,i}(t) = \int_{-15}^{15} dQ \int_{0}^{2.5} d\xi \psi_i{}^*(\xi, Q; t)\psi_i(\xi, Q; t), \tag{5.7}$$

and

$$Y_{react,i}(t) = \int_{-15}^{15} dQ \int_{-2.5}^{0} d\xi \psi_i{}^*(\xi, Q; t)\psi_i(\xi, Q; t), \tag{5.8}$$

respectively.

The degree of achieving a given objective of obtaining product isomer in the ground electronic state is measured in terms of the transition probability, given by the overlap of the laser driven WP with the target WP (ψ_{target}, which is the $|0,0\rangle$ packet in the right well of S_0 state):

$$Y_o(t) = \int_{-15}^{15} dQ \int_{0}^{2.5} d\xi \psi_g{}^*(\xi, Q; t)\psi_{target}(\xi, Q) \tag{5.9}$$

Along with the above objective additional constraints that restrict the population flow to undesired channels (such as reactant (product)-configuration in the S_1 (S_2) adiabatic state) and increase the population flow towards desired channels (such as product-configuration of the S_1 adiabatic state). The incorporation of these terms makes sure that the laser driven packet on the

excited state is mostly situated over the product channel in the ground state so that it will be dumped effectively to the latter. Therefore, we have constructed and implemented the following multi-target functional (J) (apart from usual constraints on fluence of the field and dynamics of the system) as suggested in Ref. [17].

$$J = J_o + J_{prod,S_1} + \frac{10^{-8}}{J_{react,S_1}} + \frac{10^{-8}}{J_{prod,S_2}}, \tag{5.10}$$

where

$$J_o = \frac{1}{T}\int_0^T dt' Y_o(t'), \tag{5.11}$$

$$J_{prod,i} = \frac{1}{T}\int_0^T dt' Y_{prod,j}(t'), \tag{5.12}$$

$$J_{react,i} = \frac{1}{T}\int_0^T dt' Y_{react,i}(t'), \tag{5.13}$$

where 'o' refers to objective and $j = S_1, S_2$ and $j \neq i$.

The functional in Eq. 5.10 derives contributions from four terms. The first term (J_O) maximizes the product yield of the ground state in its lowest vibrational level. The second term (J_{prod,S_1}) maximizes the yield of product configuration in the excited S_1 adiabatic states. The last two terms are inversely proportional to the yields of reactant and the product configurations of S_1 and S_2 adiabatic state, respectively. The coefficients 10^{-8} in the latter two terms are judiciously chosen such that they aid to maximize functional (fitness function) for very small values of J_{react,S_1} and J_{prod,S_2}.

5.1.1 Laser field parameterization in GA

The initial guess parameters [cf., Fig. 5.3(a)] for a typical form of an initial guess field) are optimized using GA [18–20] and the relevant equation for the field reads as

$$\epsilon_{ga}(t) = \epsilon \sin(\omega t) \cdot s(t), \tag{5.14}$$

where, ϵ is the amplitude of the laser field of frequency ω. The amplitudes are varied in a range of 0.0-0.03 a.u. and frequencies are varied within a range of 0.05 a.u. (10973 cm^{-1}) starting from an initial guess value of 0.16 a.u.(35115 cm^{-1}) to optimize the functional. The envelop function, $s(t)$, ensures smooth switch on and off of the pulse at the initial and final time, respectively [cf., Eq. (2.102) in chapter 2]. The total time duration of 200 fs is considered with a penalty factor, $\alpha = 0.001$ a.u.. The present calculations show good convergence behaviour with the widely used values of the GA parameters as suggested in Ref. [21]. The calculations took 28 generations to converge [cf., Fig. 5.3(f)].

5.2 Results and discussion

At first, the $|0,0\rangle$ nuclear wavefunction [cf., Fig. 5.2] in the reactant well of the ground electronic state (S_0) is subjected to the optimal UV-laser pulse [cf., Fig. 5.3(b)] with a carrier frequency of 43690 cm^{-1} of the pulse [cf., Fig. 5.3(c)]. In an effort to excite the system from the ground to the excited electronic state and and hence initiate the subsequent isomerization process, the action of the pulse in time is understood from the associated population dynamics of the states and the corresponding WP dynamics of both ground and excited components.

The action of the optimal pulse on the $|0,0\rangle$ packet involves a continuous effective pump action for certain time followed by a continuous effective dump action after that until certain time. In such a scenario, the amplitude of the packet is being transferred between the ground and the excited electronic states in commensurate with the pump-dump mechanism. This can be understood in terms of the laser driven population probabilities, presented in Fig. 5.3(d) and 5.3(e), of the S_0, $^1n\pi^*$ (S_1) and $^1\pi\pi^*$ (S_2) states. It can be seen from the plots of diabatic populations [cf., Fig. 5.3(d)] that the population of the ground S_0 state (curve A) decreases until $\sim$ 75 fs while that of the excited S_1 and S_2 states (curves B and C, respectively) increases in the same time range. After $\sim$ 75 fs,

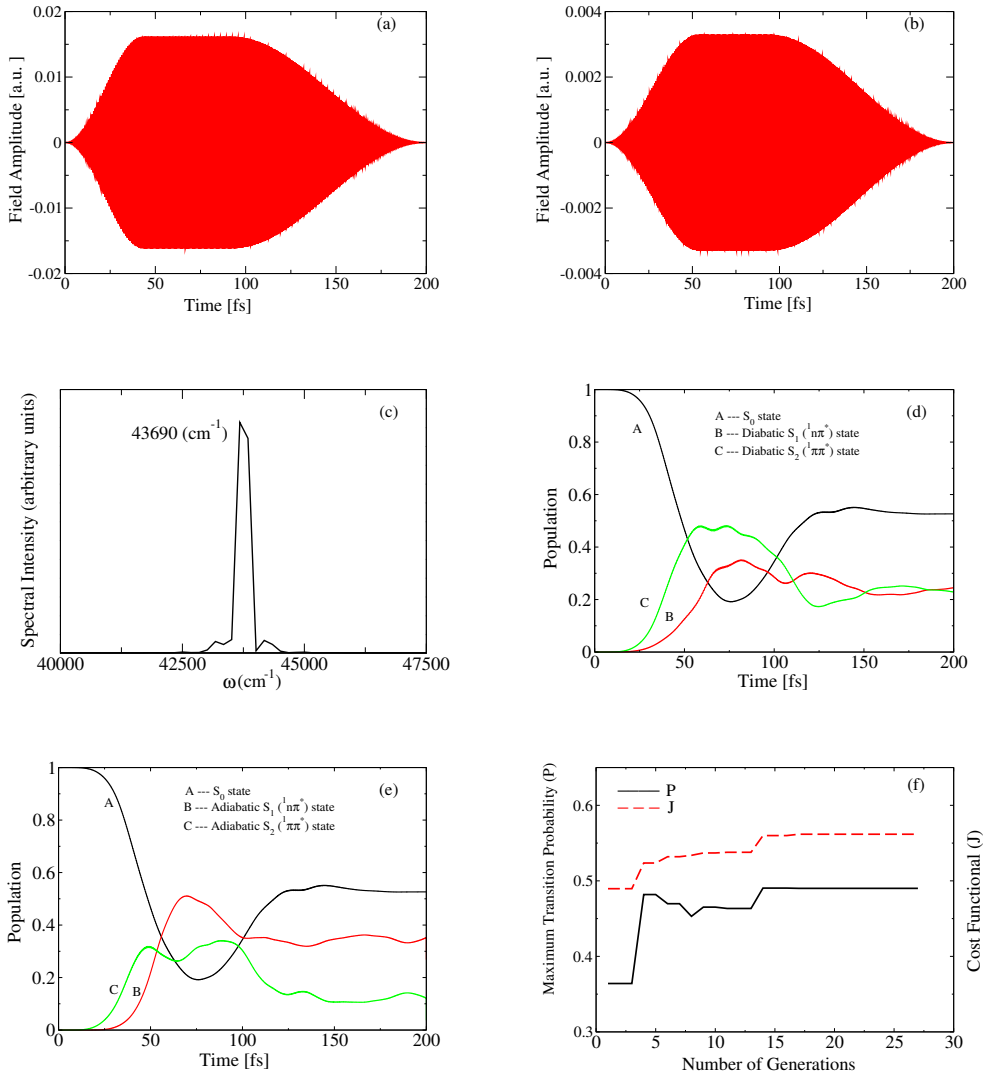

Figure 5.3: Figures (a) to (f) are initial field, optimal field, frequency spectrum, diabatic and adiabatic population dynamics (as explained in the text) and convergence behaviour of the cost functional (J) and the transition probability (P), respectively.

the population of the S_0 state starts rising mostly at the expense of diabatic S_2 and to a less extent diabatic S_1 state populations. This is because the dump portion of the optimal pulse assumes its action effectively immediately after the effective pump action (i.e., at $\sim$ 75 fs). Finally, the ground state population reaches a constant value of 0.52 around $\sim$ 175 fs. Also, excited states have their surplus populations after the dump action by laser pulse is over. Here it is noted that the S_1 state acquires its population by the pump action of the laser on S_0 state as well as nonadiabatic transfer from S_2 via CI. As transition to the S_1 state is symmetry-forbidden, the major contribution to its population comes from the latter. It can be seen from Fig. 5.3(d), the population dynamics of S_2 state (curve C) grossly reflects (apart from small oscillations which will be discussed below) the opposite behaviour to that of the S_0 state (curve A). This clearly indicates that the pump-dump mechanism operates between these two states mainly. This is because the carrier frequency of the optimal pulse ($\sim$ 0.195 a.u) is near resonant with the vertical energy of S_2 adiabatic state ($\sim$ 0.195 a.u). Therefore, the S_1 state has contribution to its population majorly due to the nonadiabatic interaction with S_2. Also the population transfer to the S_1 state due to its coupling with S_2 state by laser pulse is found to be minimal. This is explicitly verified by switching of the laser-molecule interaction term between S_1 and S_2. In this case the population remains very close to when the interaction is on. The adiabatic populations in Fig. 5.3(e) follow same arguments as that of the diabatic in the case of ground state populations (curve A) but the excited states populations (curve B and C) differ from their corresponding diabatic curves. The essential difference is that the adiabatic population curves for these excited states reverse their trends, both qualitatively and quantitatively, to their corresponding diabatic counter parts [cf., B and C in Fig. 5.3(d)]. The curves reveal that the populations promoted to the optically bright S_2 state undergo nonadiabatic transfer via S_1/S_2 CI in less than $\sim$ 25 fs onwards populating S_1 adiabatic state

efficiently. As will be discussed later, the accessing of CI can also be seen in terms of the spreading of the laser driven WP. The oscillations in both the diabatic and adiabatic excited state population curves are attributed to the repeated access of the CI by the WP components of S_1 and S_2 states because of their high vibrational energy content and their subsequent passage through CI.

The pump-dump mechanism discussed above can be illuminated further in terms of the laser driven WP snapshots taken at times that best represent the process. In Fig. 5.4 we show the probability density plots of the WPs corresponding to S_0, diabatic S_1 and S_2 states at specified times. As expected, the amplitude of the ground state packet [cf., Fig. 5.4a(i-iii)] keeps decreasing in time and it stays as a stationary gaussian during the pump action of the pulse. On the other hand, during the dump action of the pulse the amplitude of the WP starts building up in time preferentially in the product well of the ground state [cf., Fig. 5.4a(iv-vi)]. The accumulation of WP amplitude and mimicking of the shape of the target state in the right well clearly reveals that the product is formed in its lowest vibrational level. Quantitatively, the product yield is given by the transition probability and is found to be ~ 0.48 [cf., Fig. 5.3(f)]. It is noted that the dump action of the pulse could also cause population transfer to the reactant well as seen from the slightly increased amplitudes of the lobe present in it [cf., Fig. 5.4a(iv)]. However, the amplitude in this well is found to deplete again after $\sim$ 125 fs [cf., Fig. 5.4a(iv)] while the amplitude of the lobe in the right well increases around 150 fs [cf., Fig. 5.4a(v)] and reaches maximum at the final time i.e., 200 fs [cf., Fig. 5.4a(vi)] . This trend can also be observed from the population dynamics of the S_0 state and S_2 states between 125 to 150 fs time scales [cf., Fig. 5.3(d)]. This suggests that the pulse is operating the pump-dump mechanism throughout the dynamics and exploits it whenever required in maximizing the desired product yield.

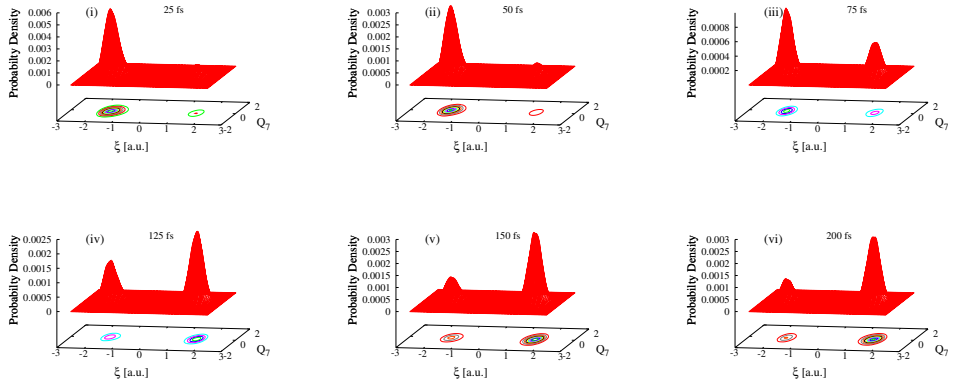

(a) Snapshots of the probability densisty of S_0 state WP components

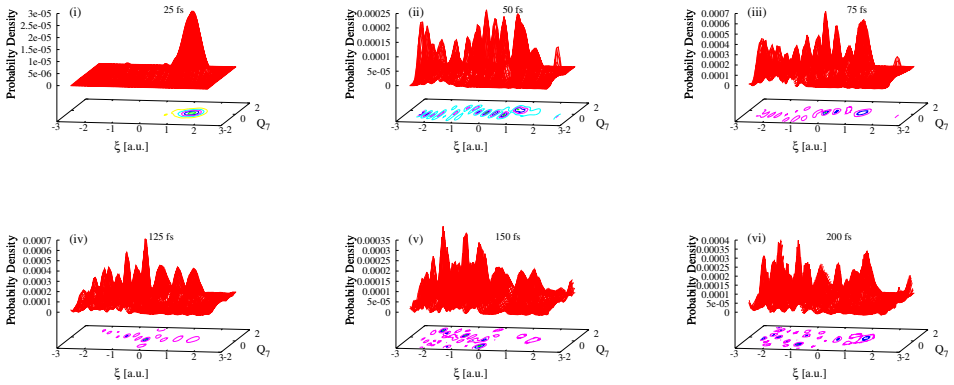

(b) Snapshots of the probability density of diabatic S_1 state WP components

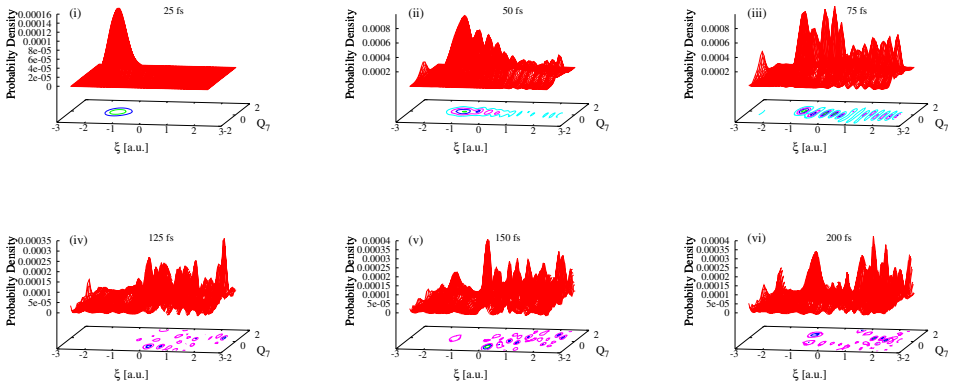

(c) Snapshots of the probability density of diabatic S_1 state WP components

Figure 5.4: Snapshots of the WP components on the S_0 state (a), diabatic S_1 (b) and diabatic S_2 (c) state at different times during the field driven dynamics (see text for details).

The probability density plots of the diabatic WPs for the excited S_1 and S_2 states are shown in Fig. 5.4b(i-vi) and Fig. 5.4c(i-vi), respectively. The snapshots of both these states taken at 25 fs suggests that the transition by laser situates the WP in the upper (S_2) adiabatic surface [cf., Fig. 5.4b(i) and cf., Fig. 5.4c(i)] for the locations of these diabatic WPs]. This is because the vertical energy difference between the S_2 adiabatic state and the left and right wells of the ground state is in resonance with the optimal pulse as discussed above in the population dynamics. The WP amplitude of S_1 diabatic state which is very low arises out of excitation of the lobe (of initial packet) present in right well of the ground state. At other time scales, both the S_1 and S_2 diabatic packets acquires a nodal pattern [cf., Fig. 5.4b(ii-vi) and cf., Fig. 5.4c(ii-vi)]. In the case of former the nodal pattern is solely due to internal conversion to vibrationally hot levels of S_1 state. This hot packet during the course of the dynamics repeatedly accesses the CI and interferes with pulse transited WP components to S_2 state leading to the nodal structure of the overall diabatic WP in latter. The interference phenomena also brings in non-symmetric nodal structure of the S_1 diabatic packet along the coupling coordinate (Q). Further, the WP with its high vibrational energy content in the diabatic S_2 state gets concentrated towards the product configuration of adiabatic S_1 state [cf., Fig. 5.4c(ii-vi)]. This suggests that the pulse effectively prepares the excited packet over the product channel in the ground state so that it is amenable to dumping to that particular channel. In doing so the laser pulse cooperatively uses effects of CI for maximizing the product yield.

The optimal field shown in Fig. 5.3(b) seem to have similar temporal profile as that of the form a typical initial guess field Fig. 5.3(a). however the peak amplitude of the optimal field ($\sim$ 0.0033 a.u.) substantially differs from that of the latter ($\sim$ 0.015 a.u.). The peak amplitude of the field is in weak field regime and hence does not infulence the topography of the PESs and their associated couplings. The convergence of the objective is seen to confirm the quality of

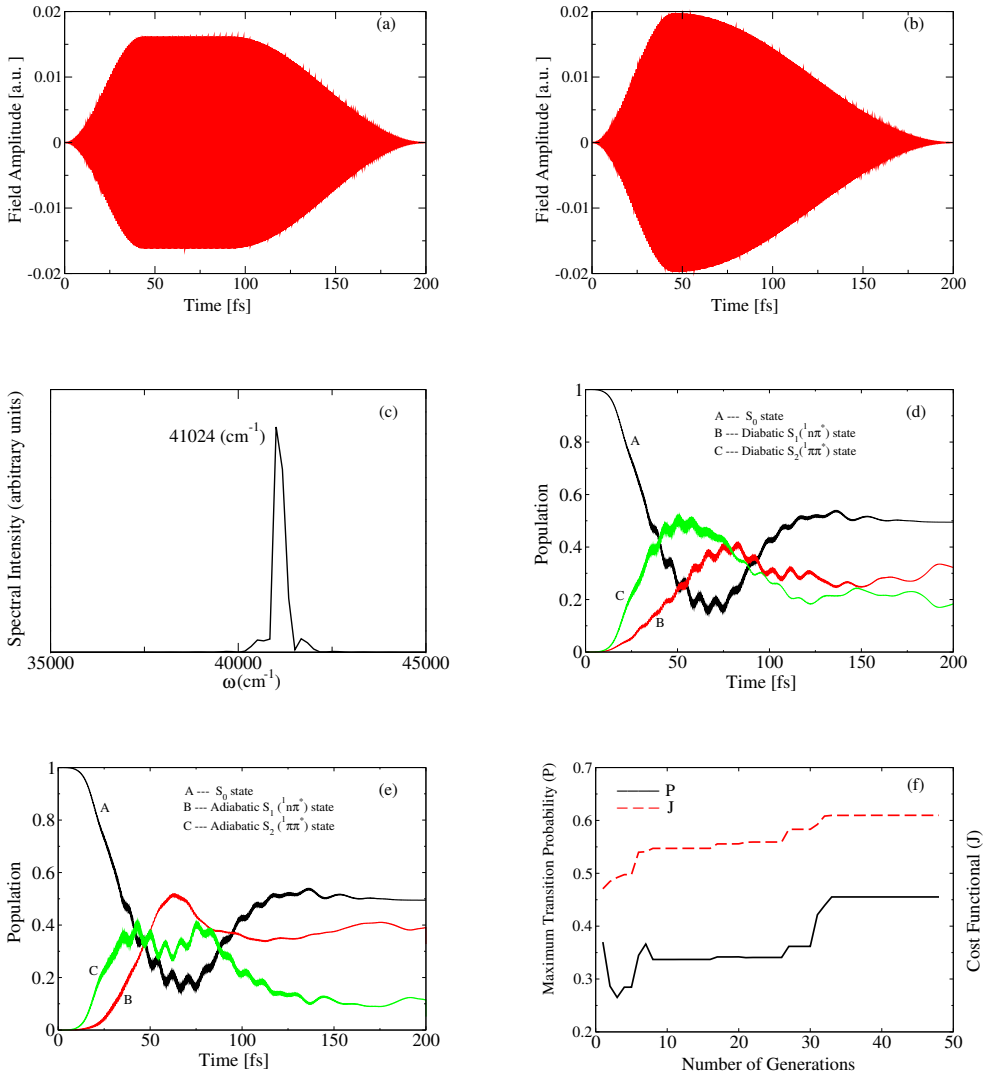

Figure 5.5: **Results of the calculations for fixed value of λ:** Figures (a) to (f) are initial field, optimal field, frequency spectrum, diabatic and adiabatic population dynamics (as explained in the text) and convergence behaviour of the cost functional (J) and the transition probability (P), respectively.

the GA. As can be seen from Fig. 5.3(f), the maximum transition probability (P) of each generation and the corresponding cost functional (J) values exhibit a constant behaviour after a certain number of generations.

We have also studied the effect of nonadiabatic coupling on the control dynamics. In this regard, calculations are carried out keeping the value of linear inter-state coupling constant λ fixed at $\xi = 0$, i.e., at the location of CI, as $\sim$ 0.006. The designed optimal UV-laser pulse [cf., Fig. 5.5(b) and 5.5(c) for its frequency spectrum] achieves the yield of product isomer about 45% which is close [cf., Fig. 5.5(f) for the transition probability] to the above discussed yield. The shape of the optimal field substantially differs from that of the initial guess field in this case unlike above. But the field peak amplitudes are quite high in this case and the pulse effectively operates in a time range that is less than that of the operational time of the pulse in the above case. However, the pump-dump mechanistic details grossly follow the same line of arguments as above but there occurs a continuous operation of back and forth transitions between the electronic states. Examination of the population dynamics of all the states [cf., Fig. 5.5(d) and 5.5(e) for diabatic and adiabatic populations, respectively] is in conjunction with the continuous pump-dump action of the pulse. Finally, the convergence behaviour of the optimization algorithm is found to be good here also. This took more number of generations as compared to the convergence above [cf., Fig. 5.5(f)].

5.3 Summarizing remarks

We have designed optimal laser pulses that have simple shape both in time and frequency domain for controlling H-transfer in malonaldehyde in its ground electronic state from the lowest vibrational state of the reactant to that of product. The task of designing optimal pulses for achieving such a state-to-state H-transfer is carried out using the OCT framework. These control calculations are carried out in the presence of nonadiabatic coupling between the electronic excited surfaces S_1 and S_2. The model used involves three electronic states and a reaction coordinate and a coupling coordinate. The optimal pulse is succesful in achieving the yields of the product in such a scenario. The laser driven dynamics yields product isomer in its lowest vibrational level in the ground (S_0) electronic state about 48%.

The control mechanism operating here is quite different from the simple pump-dump scheme explored in one dimensional case. But the idea of using excited electronic states as mediators to control isomerization in ground state remains same. The results suggest that the use of negatively chirped pulses could enhance the yield of the target product. This is because the efficient dumping of the excited packet, given its location during control dynamics, requires a portion of the pulse with a frequency that is less than that of pump portion of the pulse. The field peak amplitudes are within the experimentally accessible limits. Also, optimization using the GA method along with the pulse shaping features encourages experimental implementation. The convergence of optimization obtained in few generations.

Bibliography

[1] J. D. Coe and T. J. Martinez, J. Phys. Chem. A **103**, 618 (2006).

[2] A. L. Sobolweski and W. Domcke, J. Phys. Chem. A **103**, 4494 (1999).

[3] D. J. Tannor and S. A. Rice, J. Chem. Phys. **83**, 5013 (1985).

[4] D. J. Tannor and R. Kosloff, S. A. Rice, J. Chem. Phys. **85**, 5805 (1986).

[5] R. Kosloff, S. A. Rice, P. Gaspard, S.Tersigni, and D. J. Tannor, Chem. Phys. **139**, 201 (1989).

[6] MATLAB and Statistics Toolbox, The MathWorks, Inc., Natick, Massachusetts, United States, (2016).

[7] K. Sunderman and R. de Vivie-Riedle, J. Chem. Phys. **110**, 1896 (1999).

[8] S. P. Shah and S. A. Rice, J. Chem. Phys. **113**, 6536 (2000).

[9] C. Woywod, W. Domcke, A. L. Sobolewski, and H. -J. Werner, J. Chem. Phys., **100**, 1400 (1994).

[10] M. D. Feit and J. A. Fleck, Jr., J. Chem. Phys. **78**, 301 (1983).

[11] M. D. Feit and J. A. Fleck, Jr., J. Chem. Phys. **80**, 2578 (1984).

[12] S. Mahapatra and H. Köppel, J. Chem. Phys. **109**, 1721 (1998).

[13] S. Ghosal and S. Mahapatra, J. Phys. Chem. A **109**, 1530 (2005).

[14] C. C. Marston and G. G. Balint-Kurti, J. Chem. Phys. **91**, 3571 (1989).

[15] G. G. Balint-Kurti, C. L. Ward, and C. C. Marston, Comput.Phys. Comm. **67**, 285 (1991).

[16] G. G. Balint-Kurti, R. N. Dixon, and C. C. Marston, Int. Rev. Phys. Chem. **11**, 317 (1992).

[17] R. D. Guerrero, C. A. Arango, and A. Reyes, J. Chem. Phys. **145**, 031101 (2016).

[18] T. Brixner and G. Gerber, Chem. Phys. Chem. **4**, 418 (2003).

[19] P. Neuernberger, G. Vogt, T. Brixner, and G. Gerber, Phys. Chem. Chem. Phys. **9**, 2470 (2007).

[20] R. S. Judson and H. Rabitz, Phys. Rev. Lett. **68**, 1500 (1992).

[21] S. Sharma, H. Singh, and G. G. Balint-Kurti, J. Chem. Phys. **132**, 064108 (2010).

Chapter 6

Control of photodissociation dynamics of pyrrole: A mode-specific mechanism

The complexity of the interaction of radiation with large biological structures makes an understanding of their photochemistry a challenging exercise. Experimental advances in time-resolved spectroscopy have made it possible to have an intuitive understanding of the features of ultrafast dynamics in these large systems in terms of the relevant and smaller chromophoric units present in these structures [1]. Therefore, the quest to understand the underlying dynamics of photoexcited biological systems at the molecular level has been extensively exercised in the recent past focusing on the relevant chromophoric units [2].

Pyrrole, as is well known, has high biological relevance as a main constituent of many biomolecules. It can act as a prototype for the heteroaromatic compounds that occur in amino acids, nucleobases, heme etc. Hence, the photophysics [3] and photochemistry [4–18] of pyrrole is of fundamental interest from the viewpoint of both the experiment and theory. The photochemistry is evidenced by low quantum yield of fluorescence when UV-excitation is done to the optically bright $^1\pi\pi^*$ state. The quenching of fluorescence is due to an ultrafast nonradiative transfer to the electronic ground state. This occurs because of

strong vibronic mixing of optically bright $^1\pi\pi^*$ state with energetically low-lying optically dark $^1A_2(^1\pi\sigma^*)$ state which in turn coupled to the electronic ground state (S_0) [5, 19]. This intermediate $^1\pi\sigma^*$ state can lead to a fast N-H bond fission because of its repulsive character along the N-H bond. The experimental signature of the participation of $^1A_2(^1\pi\sigma^*)$ state in the excited state dynamics of pyrrole is confirmed by the appearance of fast moving hydrogen atoms after photoexcitation to the $^1\pi\sigma^*$-state by 250 nm, 238 nm, 243.1 nm and 242-217 nm radiations [4, 6, 14, 16]. It is also observed that tunneling also plays a crucial role in N-H fission at 250 nm excitation across a small barrier ($\sim$0.4 eV) in the $^1\pi\sigma^*$ state [13]. This photodissociation has the importance for both intra and inter molecular H-transfer reactions with regard to photoexcited nucleic acid bases and the biologically relevant aromatic amino acids. Therefore, $^1\pi\sigma^*$ excited state plays an essential role in electron/proton-transfer processes in clusters of pyrrole, indole, phenol and related chromophores and amphoteric solvent molecules, such as water or ammonia. In the latter, it is found that the photoinduced H-transfer to solvent is governed by a coupling with $^1\pi\sigma^*$ state which rules out the usual thought of coupling of the $^1\pi\pi^*$ state with ion-pair states leading to proton transfer [20].

Given the important role played by the $^1\pi\sigma^*$ state in mediating the photochemistry of pyrrole, theoretical studies to understand the underlying mechanistic details in field free conditions are carried out. These studies were based on time-dependent quantum wavepacket (WP) propagation in a reduced dimensional model [9] that provided qualitative understanding of the photodissociation dynamics. The key feature of interest is that the time scale of the dissociation dynamics and the branching ratio of the dissociation channels depend on the initial state preparation. This gives rise to mode-specific dissociation of $^1\pi\sigma^*$ state. With growing experimental interest in probing $^1\pi\sigma^*$-photochemistry, it is natural to ask what optimal shape of the pulse could effectively prepare the system (pyrrole) in this state and drive it further to the

predefined target region (in this case, to the dissociation limits)! It is with this backdrop and motivation, we address here the question of obtaining reliable optimal pulse shapes that can efficiently initiate and drive the photodissociation of a specified initial vibrational state of the electronic ground state of pyrrole. Design of such pulses is achieved theoretically within the framework of optimal control theory (OCT) [21, 22] using genetic algorithm (GA) optimization technique. This led to the simple optimal pulse shapes that are amenable to experimental implementation in probing the $^1\pi\sigma^*$ photochemistry.

In this chapter, we have considered the task of designing optimal UV-laser pulses that effectively transfer population to the $^1\pi\sigma^*$ state from various initial vibrational levels of the electronic ground state of the pyrrole. These optimal pulses causing effective transition to the $^1\pi\sigma^*$ can efficiently initiate the photodissociation dynamics via $^1A_2(^1\pi\sigma^*)$-(S_0) conical intersections (CIs) progressing further to maximal N-H dissociation. The optimal shapes of the pulses are designed using the OCT with maximization of overall dissociative flux of the WP as an objective term. The above mentioned key qualitative features of field free case are observed in this laser driven photodissociation also. We mention that under the action of the pulse, and depending on the initial vibrational state, the variation in branching ratio of the two dissociation channels is implicitly observed while monitoring the overall flux in a controlled fashion. No IR pulses are used to create specific initial vibrational states in the present work.

6.1 Theoretical model and techniques

6.1.1 Quantum dynamics within the OCT formalism

We have considered the two state two modes model in this work as developed in [9]. The coordinate definitions of the two modes are shown in Figs. 6.1a and 1b. They represent N-H stretching (r_{NH} or r, tuning mode) and the screwing deformation of H atoms (a dimensionless normal coordinate, Q_{11}, coupling mode),

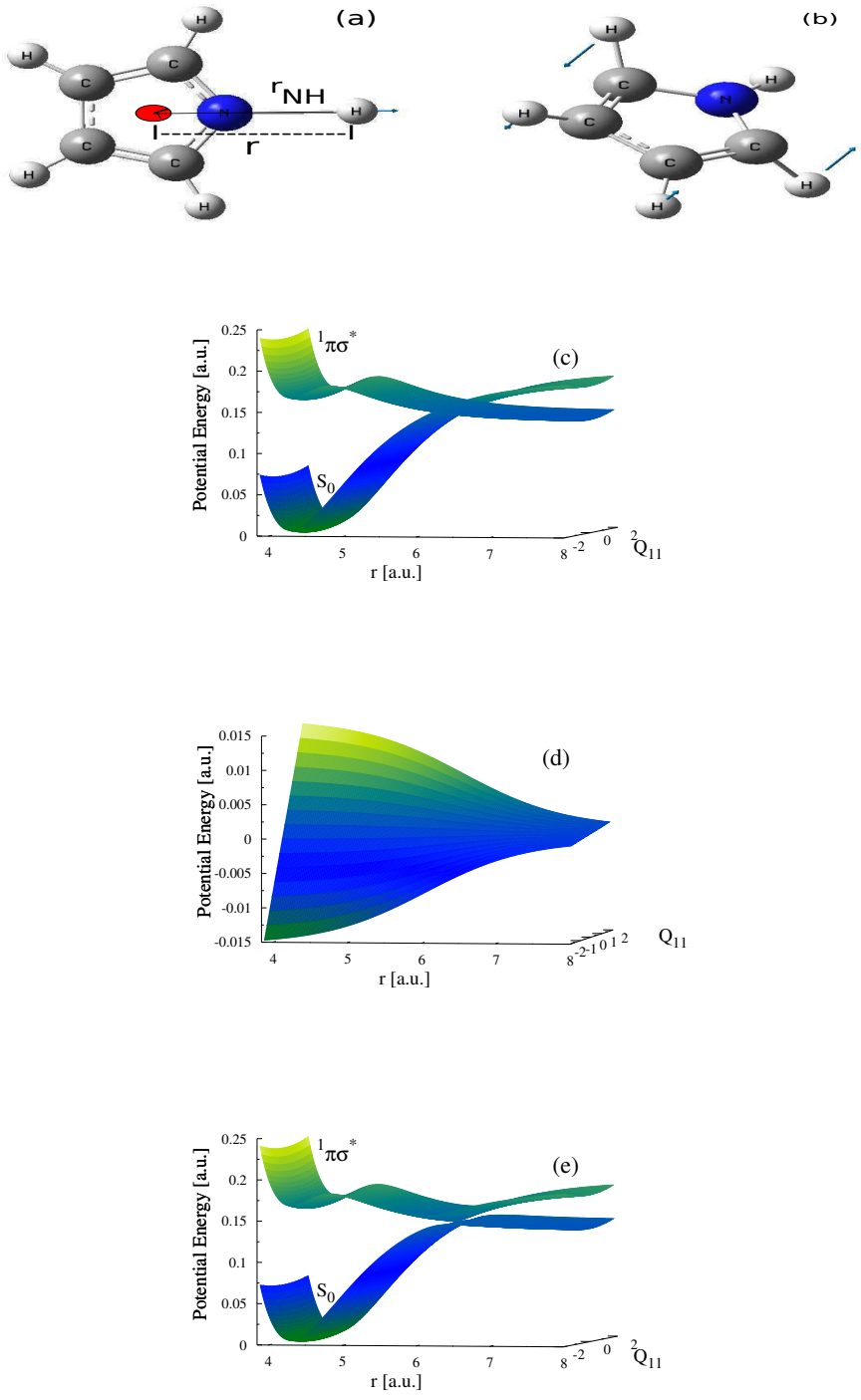

Figure 6.1: The potential energies of S_0 and $^1A_2(\pi\sigma^*)$ along the r (as shown in (a), represents N-H stretching coordinate) and Q_{11} (dimensionless coupling coordinate (b)) in the diabatic (c) and adiabatic (e) electronic representations along with the diabatic coupling (V_{12}) (d).

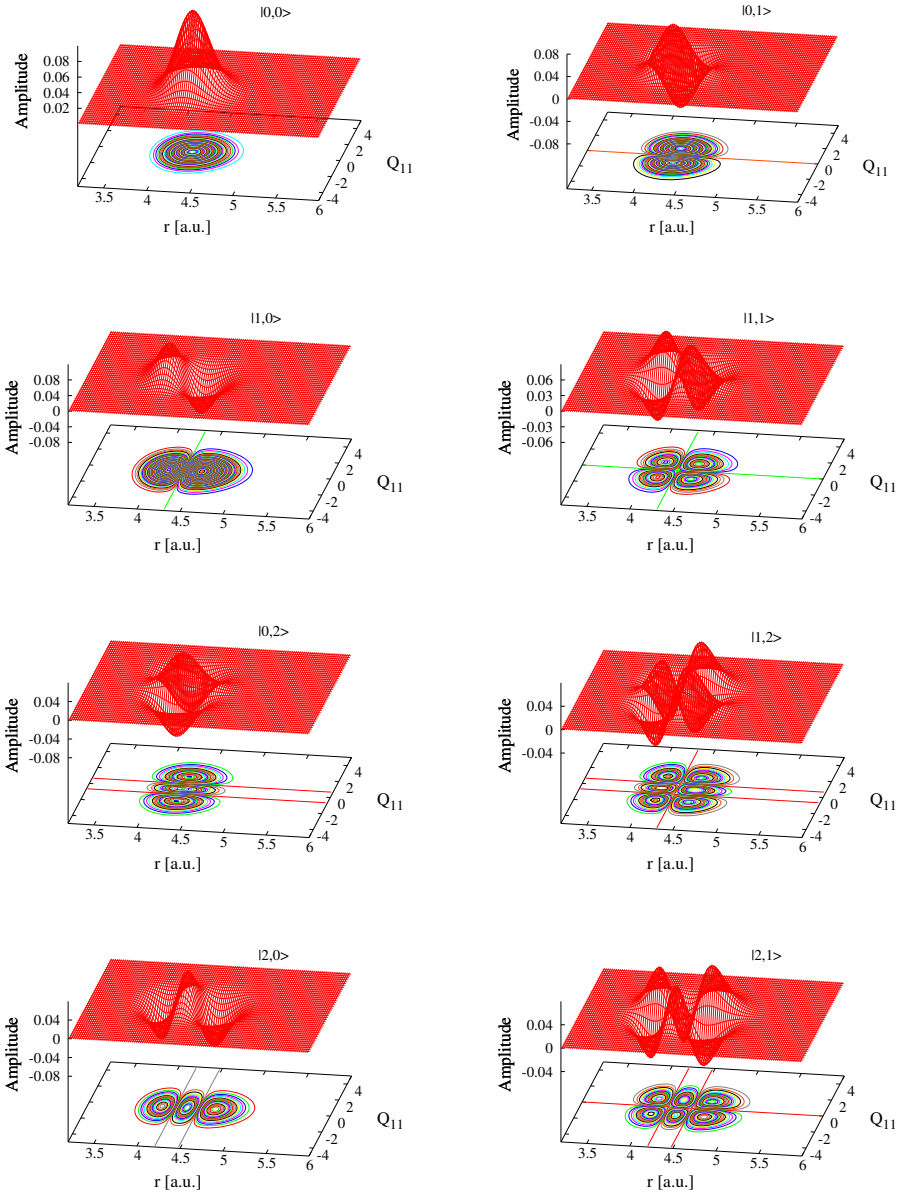

Figure 6.2: Wavefunctions of the electronic ground state (S_0) of pyrrole. Wavefunctions are labelled according to the number of nodal lines along r and Q_{11} coordinates and designated as, $|n_r, n_{Q_{11}}\rangle$ representing number of quanta along these coordinates.

Table 6.1: The calculated energy eigenvalues for eigenfunctions labelled by $|n_r, n_{Q_{11}}\rangle$ in the electronic ground state (S_0).

Energy (cm^{-1})	$\|n_r, n_{Q_{11}}\rangle$	Energy (cm^{-1})	$\|n_r, n_{Q_{11}}\rangle$
2144	$\|0,0\rangle$	6317	$\|1,1\rangle$
2919	$\|0,1\rangle$	7093	$\|1,2\rangle$
3695	$\|0,2\rangle$	8783	$\|2,0\rangle$
5542	$\|1,0\rangle$	9558	$\|2,1\rangle$

respectively. The diabatic and adiabatic potential energy surfaces (PESs) as functions of these coordinates for the two states are shown in the Figs. 6.1c and 6.1e, respectively, along with the coupling element in Fig. 6.1d. The vibrational energies and wavefunctions of the electronic ground state (S_0) are calculated using the Fourier grid hamiltonian (FGH) method [23–25]. The wavefunctions are designated in terms of number of nodes along r and Q_{11} as $|n_r, n_{Q_{11}}\rangle$. Some of these wavefunctions are plotted in Fig. 6.2. The optimal grid consists of 512 $\times$ 128 points, ranging from 3.0 a.u. to 15.0 a.u. along r and -15.0 to 15.0 along Q_{11}, respectively. Theoretically calculated vibrational frequencies [cf., Table 6.1] are found to be in good agreement with the reported experimental data [26].

In the mathematical framework of OCT, a field dependent functional is constructed and optimized to test the performance of the laser pulse in achieving desired objective. For the dissociation process, the objective is given in terms of maximizing the time-integrated outgoing flux of the WP across the dividing surface at the asymptotic dissociation channel (at, $r = r_d$), by designing an optimal field subject to the constraints on the fluence (defined as time-integrated intensity) of the field and system dynamics (governed by the time-dependent Schrödinger equation (TDSE). The dissociative flux is calculated along an analysis line at the asymptotes at, $r_d = 11.976$ a.u., as shown in Fig. 6.3. The dissociative

flux at r_d at time t_i is given by

$$F(t_i) = \frac{\hbar}{\mu} Im \left[\Psi^*(r, t_i) \frac{\partial}{\partial r} \Psi(r, t_i) \right]_{r=r_d}, \tag{6.1}$$

where m is the reduced mass along N-H stretching coordinate. The total dissociation probability [cf., Eq. 2.146 in chapter 2] is obtained by integrating the given flux over the entire duration of WP propagation as

$$P = \int_0^T F(t_i) dt, \tag{6.2}$$

The cost functional for the dissociation process is constructed using the total dissociation probability as an objective term, as

$$J\left[\epsilon(t)\right] = P - \alpha_0 \int_0^T \left[\epsilon(t)\right]^2 dt, \tag{6.3}$$

where, the second term represents the penalty constraint to lower the total energy or fluence of the pulse. The goal is to optimize (maximize) this field-dependent functional using GA based optimization method.

In the present two state model involving matter-radiation interactions, within the semi-classical dipole approximation [27, 28], the TDSE reads as

$$i\hbar \frac{\partial}{\partial t} \begin{pmatrix} |\psi_e\rangle \\ |\psi_g\rangle \end{pmatrix} = \begin{pmatrix} \hat{H}_e & \hat{U}_{ge} \\ \hat{U}^*_{ge} & \hat{H}_g \end{pmatrix} \begin{pmatrix} |\psi_e\rangle \\ |\psi_g\rangle \end{pmatrix}. \tag{6.4}$$

In the above equation, the labels e and g, are used for the $^1\pi\sigma^*$ and S_0 electronic states of pyrrole, respectively, for the wavevectors and the operators. The operator $\hat{H}_{g/e}$ reads,

$$\hat{H}_{g/e} = -\frac{\hbar^2}{2m} \frac{\partial^2}{\partial r^2} - \frac{1}{2} \omega_{11} \frac{\partial^2}{\partial Q_{11}^2} + \hat{U}_{g/e}, \tag{6.5}$$

where, $m = \frac{m_H m_p}{m_H + m_p}$, is the reduced mass along r (m_H and m_p denote the mass of the hydrogen atom and the rest of the pyrrole ring, respectively) and $\omega_{11} = 664$ cm^{-1}, is the frequency of the coupling vibrational mode Q_{11}. The off-diagonal terms of the matrix Hamiltonian on the right hand side of Eq. (6.4) represent the

interaction potential, $\hat{\mu}_{eg} \cdot \epsilon(t)$, plus the diabatic coupling, $\hat{U}_{dc}$, and $\hat{U}_{ge} = \hat{U}^*_{eg}$. The quantity, $\epsilon(t)$, defines the time-dependent electric field of the laser pulse. We treat the transition dipole moment operator $\hat{\mu}_{eg}$ within the constant dipole approximation (CDA) for numerically solving the two states TDSE. The CDA is assumed over complete space because there exists a non-vanishing transition dipole moment (TDM) for large range of the dissociation coordinate (r) between the two electronic states under consideration. Moreover, the CDA is a valid approximation in a diabatic electronic basis [29] as the electronic character of the states is retained throughout the nuclear coordinate space in this basis. Numerically, the Fourier transformation method is used to evaluate the action of kinetic energy operators of the Hamiltonian on the wavefunction and the time propagation is carried out by a second order split-operator method [30, 31] adapted to coupled electronic states [32, 33].

A sine-damping function [34] is used to absorb the wavefunction at the grid boundaries to avoid spurious reflections of the wavefunction

$$f(r_i) = \sin\left[\frac{\pi}{2}\frac{r_{mask} + \Delta r_{mask} - r_i}{\Delta r_{mask}}\right], r_i \geq r_{mask}, \tag{6.6}$$

where $r_{mask} = 13.5$ a.u. is starting point of the damping function and $\Delta r_{mask} = r_{max} - r_{mask}$ is the width of the damping function over which it decays from 1 to 0.

In order to follow the action of the laser pulse and hence to interpret the associated control mechanism, analysis of the laser driven population dynamics is carried out. In this regard, more insights can also be obtained by examining adiabatic, $P_i^{ad}(t) = \langle\Psi(t)|\psi_i^{ad}\rangle\langle\psi_i^{ad}|\Psi(t)\rangle$, $i = e$ or g, and diabatic, $P_i^{dia}(t) = \langle\Psi(t)|\psi_i^{dia}\rangle\langle\psi_i^{dia}|\Psi(t)\rangle$, $i = e$ or g, electronic populations. Adiabatic and diabatic electronic population probabilities are defined as expectation values of the respective projection operators constructed using ground and excited WP components [35]. Numerical calculations of adiabatic populations is done using adiabatic projectors constructed in a diabatic basis as suggested in [36, 37]. Here,

we have employed the prescription given by Eqs. 2.155 and 2.156 in chapter 2 for estimating both the diabatic and adiabatic populations.

6.1.2 Laser field parameterization in GA

The initial guess parameters (see Fig. 6.4 for a typical initial guess field form) are optimized using GA [38–40] and the relevant equation for the field reads as

$$\epsilon_{ga}(t) = \epsilon \sin(\omega t) \cdot s(t), \tag{6.7}$$

where, ϵ is the amplitude of the laser field of frequency ω. The amplitudes are varied in a range of 0.0-0.03 a.u. and frequencies are varied within a range of 0.05 a.u. (10973 cm^{-1}) starting from an initial guess value of 0.1609 a.u.(35313 cm^{-1}) to optimize the cost functional. The envelop function, $s(t)$, ensures smooth switch on and off of the pulse at the initial and final time, respectively. The total time duration of 30000 a.u, is considered with a penalty factor, $\alpha = 0.001$ a.u.. The envelop function $s(t)$ is given by Eq. (2.102) in chapter 2. The present calculations show good convergence behaviour with the widely used values of the GA parameters as suggested in Ref. [41].

We note that throughout the text we follow the nomenclature suggested in Fig. 6.3 for the electronic states and dissociation limits. In this figure the curves with same color coding represents diabatic and with different color coding represent adiabatic electronic states. Therefore, the lower (S_0) curve (black) connected with the red one beyond CI represents the ground (lower) adiabatic state and upper ($^1\pi\sigma^*$) curve (red) connected with the black one beyond CI represents the excited (upper) adiabatic state. Therefore in this definition the black and red curves beyond the CI represent the upper and lower adiabatic dissociation channels.

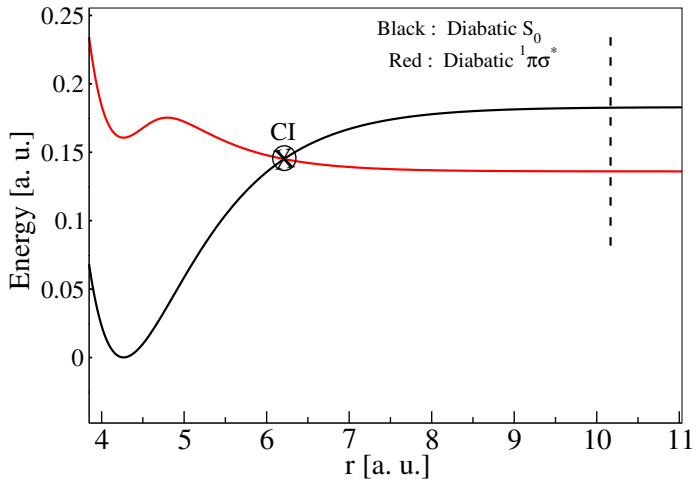

Figure 6.3: The diabatic potential energies of S_0 and $^1A_2(\pi\sigma^*)$ states of pyrrole along r (defined in the text). The location of CI and the analysis line of dissociative WP flux is shown by an encircled cross mark and a dashed line, respectively.

6.2 Results and discussion

To start with, the $|0,0\rangle$ nuclear wavefunction [cf., Fig. 6.2] in the ground electronic state (S_0), is subject to the optimal UV-laser pulse [cf., Fig. 6.4(b)] with a central wavelength of 267 nm. The wavelength is obtained from the carrier frequency of the pulse shown in Fig. 6.4(c). In an effort to excite the system from the ground to the excited electronic state and and hence initiate the subsequent dissociation process, the action of the pulse in time is understood from the associated population dynamics of the states, time-integrated flux behaviour of the two dissociation limits and the corresponding field-driven WP (both ground and excited component) dynamics.

Throughout the optimal pulse action on the $|0,0\rangle$ packet, its amplitude is continuously being transferred from the ground to the excited electronic state, till the end of time duration. The laser driven dynamics yields dissociation

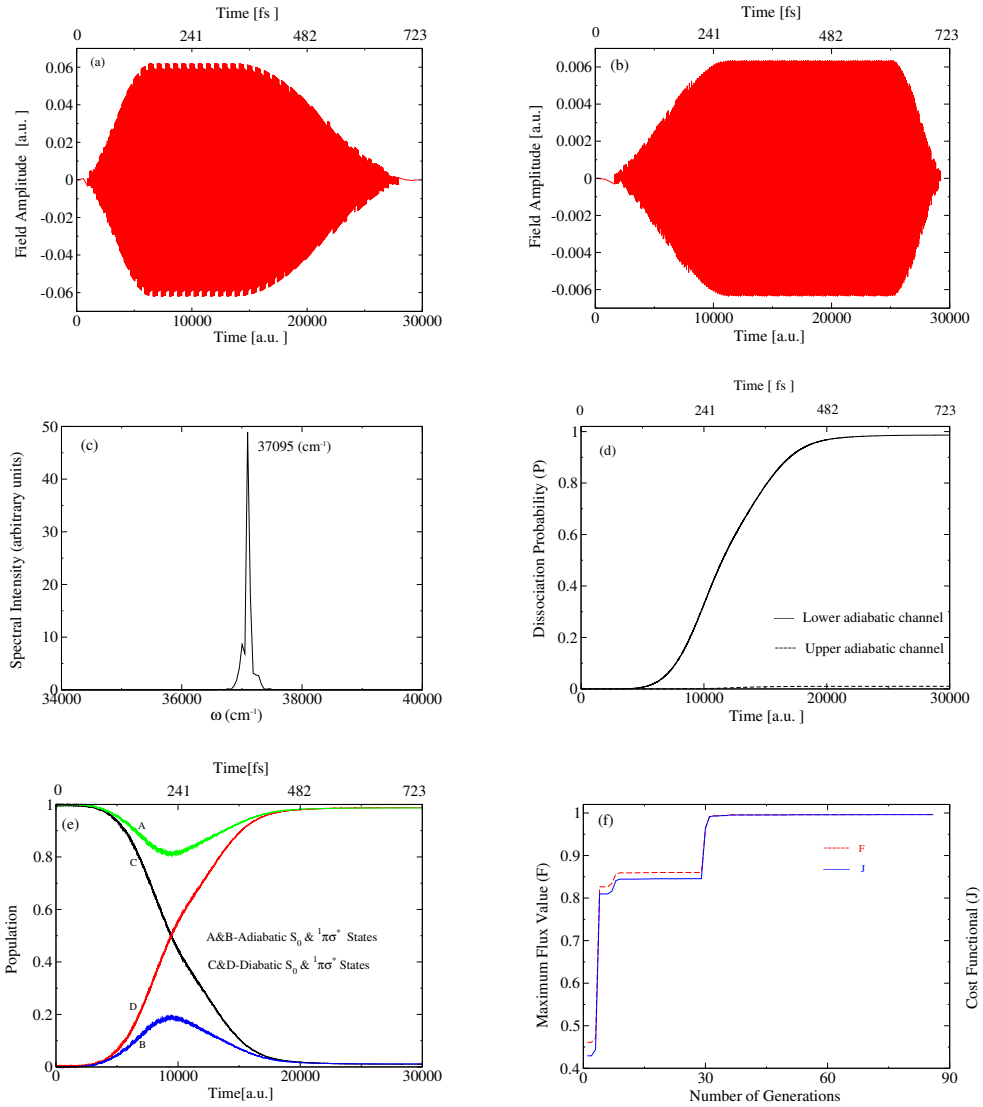

Figure 6.4: Figures (a) to (f) are initial field, optimal field, frequency spectrum, time-integrated flux, diabatic-adiabatic population dynamics (as explained in the text) and convergence behaviour of cost functional (J) and total flux (F), respectively.

products on the lower (S_0) adiabatic asymptote almost entirely. The dissociation probabilities calculated at the S_0 and $^1\pi\sigma^*$ adiabatic asymptotes are shown by the dot-dashed and solid lines, respectively, in Fig. 6.4(d). It can be seen that, in this situation virtually there is no dissociation taking place via $^1\pi\sigma^*$ adiabatic asymptote. This can be understood from the corresponding field-driven population dynamics. It can be seen from Fig. 6.4(e) that both the adiabatic and diabatic S_0 state populations (curves A & D, respectively) start decreasing at early times. But complete recovery of adiabatic population occurs after $\sim$ 230 fs, while the diabatic populations continuously decrease. Exactly an opposite behaviour is reflected in the population dynamics of the $^1\pi\sigma^*$ state [cf., the adiabatic and diabatic population curves, B & C in Fig. 6.4(e), respectively]. After the excitation of the WP amplitude at each point of time with the optimal pulse, the complete dissociation takes place on the lower (S_0) adiabatic dissociation [cf., Fig. 6.4(d)] limit. This explains the population dynamics after $\sim$ 230 fs. The transfered WP leaks through the barrier present in the excited $^1A_2(^1\pi\sigma^*)$ state due to insufficient mean energy of the WP compared to the barrier height. Thereby the excited WP reaches $^1A_2(^1\pi\sigma^*)$-S_0 CIs subsequently and dissociates on the lower adiabatic surface at large r limit. The internal conversion to the S_0 state is minimal in this situation. This also means that the transferred WP population stays on the ($^1\pi\sigma^*$) diabatic state giving rise to the population dynamics as discussed above. Also, the time-behaviour of the flux clearly indicates the recovery of adiabatic populations and continuous decrease/increase of diabatic populations in the $S_0/^1\pi\sigma^*$ state at later times. In Fig. 6.7a(i-iii) the snapshots of the WP components on the diabatic states are shown at regular intervals of time. As expected, the amplitude of the ground state packet keeps decreasing in time and it stays as a stationary gaussian for most of the time. Some nodal pattern starts appearing in the S_0 state component solely due to internal conversion to vibrationally hot levels (of S_0 state) although it is

insignificant as seen from the population dynamics. The $^1\pi\sigma^*$ diabatic WP, at each time, moves to the CI by tunneling after it is created by the pulse as is evident from the snapshots of the Fig. 6.7a(iv-vi). Finally it starts dissociating to the lower (S_0) adiabatic asymptote. This keeps happening for the entire period of pulse-driven dynamics. Most efficiently, the dissociation occurs around ~ 230 fs) when the population transfer is maximum. The convergence of the objective is seen to confirm the quality of the optimization algorithm used, as can be seen from Fig. 6.4(f), where the maximum flux value and the cost functional values start coinciding and become constant after a certain number of generations. It is worth mentioning that the field driven tunneling dynamics (for 30000 a.u.) is much faster and quantitatively yields higher dissociation probability on the lower adiabatic asymptote when compared to the field free dynamics. For illustration of the differences in the dynamics, we show in Fig. 6.5 for the flux variation (a) and the associated the population dynamics (b) of the $|0,0\rangle$ in the field free situation for a total propagation time of 90000 a.u. (the time scale and the calculations are made use of heavily in the following chapter).

Similarly, different initial vibrational levels are subjected to the same initial guess control field as in the $|0,0\rangle$ case in an effort to design respective optimal fields that bring about effective photodissociation. It is observed that the laser driven dissociation dynamics with these initial conditions qualitatively differs from $|0,0\rangle$ condition as follows. As shown in Fig. 6.6, the vibrational states $|1,0\rangle$, $|1,1\rangle$ and $|1,2\rangle$ as initial conditions lead to different values of the the branching ratio by opening up the upper dissociation channel [cf., panels A3, B3 and C3 of the figure]. Although the values of dissociation probabilities in panel A3 ($|1,0\rangle$) are similar to the $|0,0\rangle$ case [cf., Fig. 6.4(d)], the rate at which dissociation occurs differs from it. Indeed, the dissociation probability starts sharply rising at times earlier than ~ 230 fs, as compared to the $|0,0\rangle$ case in which it rises at ~ 230 fs. The same is also true for the $|1,1\rangle$ and $|1,2\rangle$ cases [cf., B3 and C3]. This shows

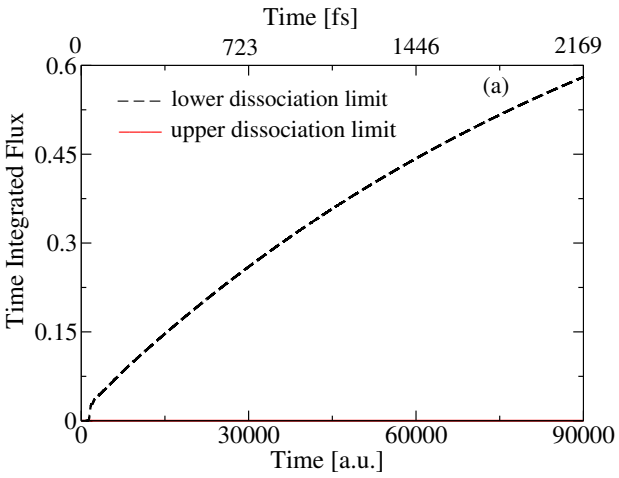

(a) Flux behaviour

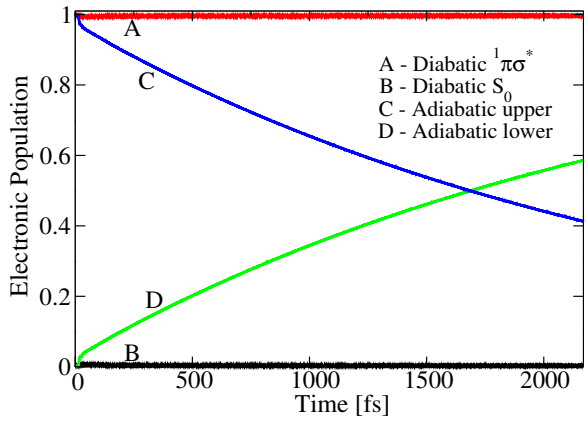

(b) Population dynamics

Figure 6.5: (a) The time-integrated flux of both the upper and lower dissociation channels and (b) the time dependence of diabatic and adiabatic electronic population, in the field free dynamics of $|0,0\rangle$ packet situated in the $^1A_2(^1\pi\sigma^*)$ state by vertical excitation.

that excitation along the tuning mode (r) enhances the rate of the dissociation. The early rise of dissociation probabilities clearly manifests in the corresponding population dynamics [cf., panels A4, B4 and C4]. The optimal laser driven $|1,1\rangle$ and $|1,2\rangle$ WPs possess enough energy to go over the barrier to reach the CIs [cf., B1 and C1, Fig. 6.6 for their respective optimal pulses]. The snapshots of both the S_0 and $^1\pi\sigma^*$ diabatic WP components in the case of $|1,1\rangle$ are presented in Fig. 6.7(b). The main dynamical features of the WP are more or less the same as that of $|0,0\rangle$ case except that it contains high energy components that enable it to reach the upper adiabatic dissociation limit. Also in this case there is relatively more internal conversion to the S_0 state and the WP components in the latter state become vibrationally hot [cf., Fig. 6.7b(i-iii)]. On the other hand, the WP components on the excited state undergo interference and give rise to nodal structure along r [cf., Fig. 6.7b(iv-vi)]. The interference arises due to the trapped WP components in the attractive well between the barrier and dissociation limit, on the upper state. A point worth noting from the snapshots of the excited state WPs in all cases (including $|1,0\rangle$ and $|1,2\rangle$ cases also) is that they are a replica of initial WP in the ground state, at all times in the Franck-Condon (FC) region. This indicates that at each point of time, components of the optimal pulse causes a δ-excitation by promoting a small portion of the initial WP to the upper electronic state.

It is also seen that the optimal pulses (A1, B1 and C1 of Fig. 6.6) in each case [including $|0,0\rangle$, cf., Fig. 6.4(b)] seem to have overlapping frequency spectrum [cf., panels A2, B2 and C2 of Fig. 6.6] although the central frequency differs. This indicates that the effect of initial conditions on pulse shaping is more in terms of determining the amplitude profile as is seen in the markedly different pulse profiles. Moreover, in all the cases the optimal pulses are associated with high intensity ($\sim$2-15 TW/cm^2). And they are experimentally feasible to generate at their high carrier frequencies with such intensities. Finally, the convergence

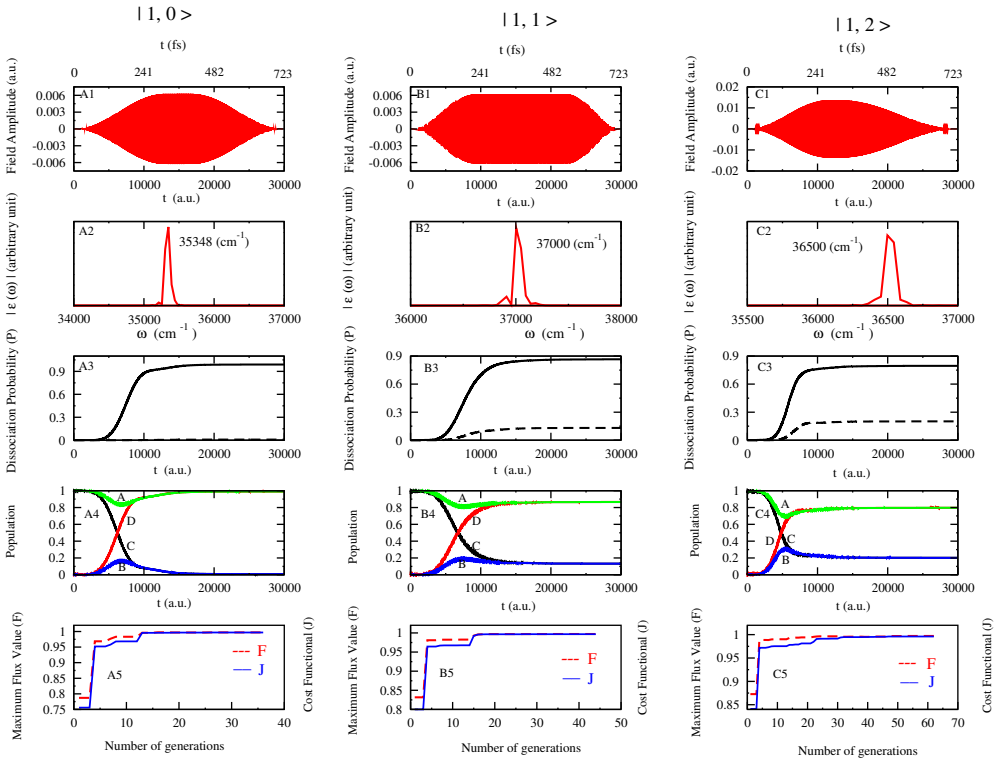

Figure 6.6: Amplitude profiles of optimal pulses as functions of time (A1, B1 and C1), frequency spectra of the optimised laser fields (A2, B2 and C2), dissociation probabilities (A3, B3 and C3, line types are same as Fig. 6.4(d)) and diabatic and adiabatic population dynamics of the S_0 and $^1\pi\sigma^*$ electronic states (A4, B4 and C4, the curves in each panel follow the same designation as in Fig. 6.4(e)). The plots in A5, B5 and C5 show convergence behaviour of total flux (F) and the cost functional (J) with number of generations involved in the optimization.

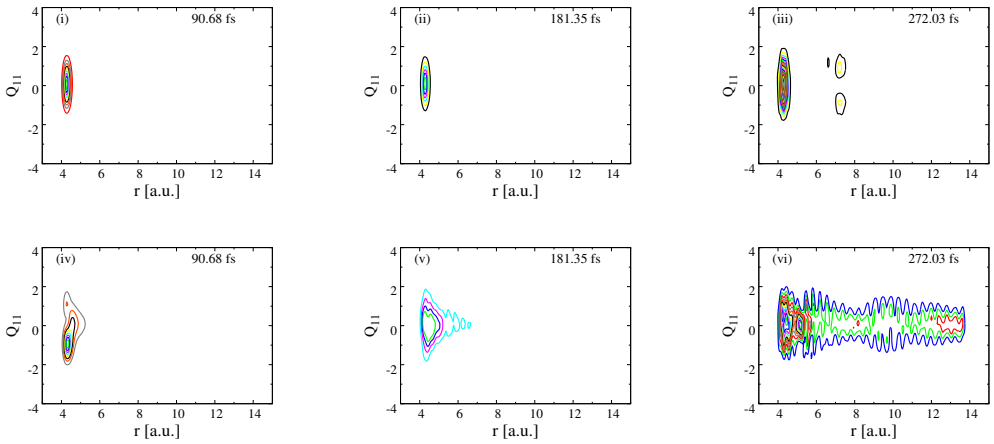

(a) $|0,0\rangle$ case

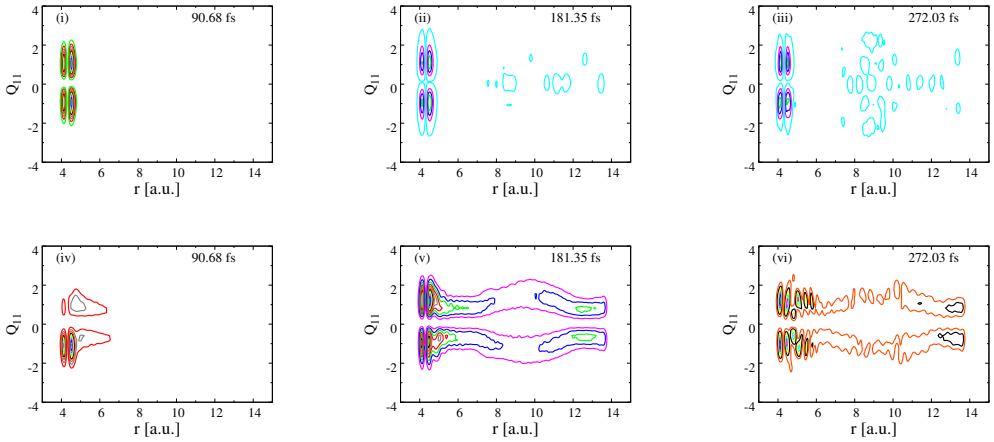

(b) $|1,1\rangle$ case

Figure 6.7: Snapshots of the WP components on the diabatic S_0 state (panels i,ii and iii) and diabatic $^1\pi\sigma^*$ state (panels iv, v and vi) at different times during the field driven dynamics (see text for details).

behaviour set up by the GA with the number of generations evolved is shown in panels A5, B5 and C5 of Fig. 6.6. These plot(s) show the maximum flux (F), and cost functional (J) values are more or less comparable and they keep increasing in steps until a constant value is reached for the final generations. It can be seen that the convergence in all cases is found to be good in general.

Finally, in all the above cases the effective transition between the two electronic states occurs before CIs, mostly in the FC region, since the pulses are in resonance with the energy gap. This is explicitly verified by setting the transition moment value to zero after CIs by switching off the laser-molecule interaction term in the Hamiltonian. In such a situation we found that the overall pulse driven dynamics (both qualitatively and quantitatively) is similar to the case when the interaction term is on. Furthermore this suggests that the constant value of TDM (within the Condon approximation) assumed in this work is well justified.

6.3 Summarizing remarks

We have designed and applied optimal UV-laser pulses to carry out excitation to the $^1\pi\sigma^*$ state and initiate photodissociation of pyrrole via S_0-$^1\pi\sigma^*$ CIs with maximum dissociation yields. The optimal pulses for various initial vibrational states of the system are designed to achieve the desired control task. In all cases, the designed pulses are simple, have smooth profile in time and hence are amenable to experimental implementation. Moreover, the pulses have roughly close matching central wavelengths (ranging from $\sim$269-282 nm) of that of experimentally implemented pulses for probing both the tunneling and barrier crossing dynamics on the $^1A_2(^1\pi\sigma^*)$ state. Therefore, the theoretical quantum control insights obtained here are highly experimentally relevant and useful in understanding $^1\pi\sigma^*$-photochemistry.

The optimally driven dissociation made use of the effect of CIs in such a way that the dissociation flux is maximized (i.e., enhancing overall dissociation). The crucial thing in this optimal photodissociation is in setting up the population in the electronic excited state and its further evolution to the dissociation limits. It is also verified that, under the action of the lasers, the excitation of the coupling mode gives rise to the increased dissociation probability of the upper channel. Similarly as the tuning mode is excited, the rate of the dissociation increases. It is also found that the convergence behaviour of GA is shown to be extremely good.

Bibliography

[1] M. Staniforth and V. G. Stavros, Proc. R. Soc. A **469**, 20130458 (2013).

[2] C. T. Middleton, Kimberly de La Harpe, C. Su, Y. K. Law, C. E. Crespo-Hernández, and B. Kohler, Annu. Rev. Phys. Chem. **60**, 217(2009).

[3] M. B. Robin, *Higher Excited State of Polyatomic Molecules*, Academic, New York, (1972).

[4] D. A. Blank, S. W. North, and Y. T. Lee, Chem. Phys. **187**, 35 (1994).

[5] A. L. Sobolewski, W. Domcke, C. Dedonder-Lardeux, and C. Jouvet, Phys. Chem. Chem. Phys. **4**, 1093 (2002).

[6] B. Cronin, M. G. D. Nix, R. H. Qadiri, and M. N. R. Ashfold, Phys. Chem. Chem. Phys. **6**, 5031 (2004).

[7] J. Wei, J. Riedel, A. Kuczmann, F. Renth, and F. Temps, Faraday Discuss. **127**, 267 (2004).

[8] H. Lippert, H. H. Ritze, I. V. Hertel, and W. Radloff, Chem. Phys. Chem. **5**, 1423 (2004).

[9] V. Vallet, Z. Lan, S. Mahapatra, A. L. Sobolewski, and W. Domcke, J. Chem. Phys. **123**, 144307 (2005).

[10] Z. Lan, A. Dupays, V. Vallet, S. Mahapatra, and W. Domcke, J. Photochem. Photobio. A. Chemistry. **190**, 177 (2007).

[11] Z. Lan and W. Domcke, Chem. Phys. **350**, 125 (2008).

[12] S. Faraji, M. Vazdar, V. Sivaranjana Reddy, M. Eckert-Maksic, H. Lischka, and H. Köppel, J. Chem. Phys. **135**, 15310 (2011).

[13] G. M. Roberts, C. A. Williams, H. Yu, A. S. Chatterley, J. D. Young, S. Ullrichb, and V. G. Stavros, Faraday Discuss. **163**, 95 (2013)

[14] M. Epshtein, A. Portnov, R. Kupfer, S. Rosenwaks, and I. Bar, J. Chem. Phys. **139**, 184201 (2013).

[15] S. P. Neville and G. A. Worth, J. Chem. Phys. **140**, 034317 (2014).

[16] G. Wu, S. P. Neville, O. Schalk, T. Sekikawa, M. N. R. Ashfold, G. A. Worth, and A. Stolow, J. Chem. Phys. **142**, 074302 (2015).

[17] K. Saita, M. G. D. Nix, and D. V. Shalashilin, Phys. Chem. Chem. Phys. **25**, 16227 (2013).

[18] D. V. Makhov, K. Saita, T. J. Martinez, and D. V. Shalashilin, Phys. Chem. Chem. Phys. **17**, 3316 (2015).

[19] H. Köppel, E. V. Gromov, and A. B. Trofimov, Chem. Phys. **35**, 304 (2004).

[20] A. L. Sobolewski and W. Domcke, J. Phys. Chem. A **105**, 9275 (2001).

[21] S. Shi and H. Rabitz, J. Chem. Phys. **92**, 364 (1990).

[22] W. Zhu, J. Botina, and H. Rabitz, J. Chem. Phys. **108**, 1953 (1998).

[23] C. C. Marston and G. G. Balint-Kurti, J. Chem. Phys. **91**, 3571 (1989).

[24] G. G. Balint-Kurti, C. L. Ward, and C. C. Marston, Comput.Phys. Comm. **67**, 285 (1991).

[25] G. G. Balint-Kurti, R. N. Dixon, and C. C. Marston, Int. Rev. Phys. Chem. **11**, 317 (1992).

[26] K. R. F. Somers, E. S. Kryachko, and A. Ceulemans, J. Phys. Chem. A **107**, 5427 (2003).

[27] K. Sunderman and R. de Vivie-Riedle, J. Chem. Phys. **110**, 1896 (1999).

[28] S. P. Shah and S. A. Rice, J. Chem. Phys. **113**, 6536 (2000).

[29] C. Woywod, W. Domcke, A. L. Sobolewski, and H. -J. Werner, J. Chem. Phys. **100**, 1400 (1994).

[30] J. C. Light, I. P. Hamilton, and V. J. Lill, J. Chem. Phys. **82**, 1400 (1985).

[31] M. D. Feit, J. A. Fleck, and Jr., A. Steiger, J. Comput. Phys. **47**, 412 (1982).

[32] S. Mahapatra and H. Köppel, J. Chem. Phys. **109**, 1721 (1998).

[33] S. Ghosal and S. Mahapatra, J. Phys. Chem. A, **109**, 1530 (2005).

[34] S. Mahapatra, N. Sathyamurthy, J. Chem. Soc., Faraday Trans. **97**, 9062 (1997).

[35] H. Köppel, W. Domcke, and L. S. Cederbaum, Adv. Chem. Phys. **57**, 59 (1984).

[36] U. Manthe and H. Köppel, J. Chem. Phys. 93, 345 **93**, 1658 (1990).

[37] U. Manthe, H. Köppel, and L. S. Cederbaum, J. Chem. Phys. **95**, 1708 (1991).

[38] T. Brixner and G. Gerber, Chem. Phys. Chem. **4**, 418 (2003).

[39] P. Neuernberger, G. Vogt, T. Brixner, and G. Gerber, Phys. Chem. Chem. Phys. **9**, 2470 (2007).

[40] R. S. Judson and H. Rabitz, Phys. Rev. Lett. **68**, 1500 (1992).

[41] S. Sharma, H. Singh, and G. G. Balint-Kurti, J. Chem. Phys. **132**, 064108 (2010).

Chapter 7

Control of photodissociation dynamics of pyrrole: An alternative over the conventional mechanism

As mentioned in chapter 6, the photodissociation (more specifically, N-H dissociation) dynamics of pyrrole is proven to be mediated predominantly via its optically dark $^1\pi\sigma^*$ ($^1A_2$) electronic excited state which is repulsive along the N-H stretch coordinate [1–17]. This state undergoes symmetry allowed crossings with optically bright excited $^1\pi\pi^*$ states as well as the electronic ground S_0 state [3]. The participation of $^1\pi\sigma^*$ ($^1A_2$) state of pyrrole in the photo-induced dynamics is evidenced by the formation of H atoms in the experiments carried out with 250 nm, 238 nm, 243.1 nm and 242-217 nm UV-radiations [2, 4, 12, 15]. It was concluded from the observation of a large kinetic isotope effect in these experiments that quantum tunneling plays a major role in the photodissociation dynamics at 250 nm excitation [11]. As studied in the previous chapter (i.e., Chap. 6), the photodissociation dynamics of initially prepared vibrational state in the $^1\pi\sigma^*$ ($^1A_2$) state with the aid of an optimally controlled laser pulses reveal that branching ratio of the dissociation products is dependent on the specified initial vibrational state under consideration, similar to that observed in field free

conditions [7]. It was found that vibrationally hot initial state opens up both upper and lower dissociation channels [cf., Fig. 6.3 for the nomenclature] by allowing the wavepacket (WP) to cross over the barrier present in the vicinity of the Franck-Condon (FC) region on the $^1\pi\sigma^*$ state [cf., Fig. 6.3(a)]. However, when the WP corresponding to the ground vibrational level of S_0 state (i.e., $|0,0\rangle$ packet) is launched on the $^1\pi\sigma^*$ ($^1A_2$) state, no branching ratio was found. In this case, the dynamics was found to be slow and dissociation was reported to occur via tunneling of the WP through the barrier of height, $\sim$0.40 eV, on the $^1\pi\sigma^*$ ($^1A_2$) state. In this situation the upper adiabatic dissociation channel was found to remain essentially closed [7, 11]. Therefore, it is clear that the vibrational excitation of an initially prepared $|0,0\rangle$ packet in the $^1\pi\sigma^*$ ($^1A_2$) is necessary in order to bring about the non-zero branching ratio of the dissociation products.

In this chapter, we have devised an alternative mechanistic route for controlling this photodissociation dynamics by constructing an optimally controlled laser pulse (of $\sim$ 2.2 ps time duration). The latter transfers the WP back and forth between the S_0 and $^1\pi\sigma^*$ states after its initial excitation to the $^1\pi\sigma^*$ state. In doing so the pulse makes use of electronic transitions due to nonadiabatic effects of CI in a cooperative manner. The pulse is optimized subsequently leading to an optimal shape of the pulse to achieve the desired goal. Such an optimal pulse is shown to efficiently yield the product branching ratio. Although the previous quantum control studies on photodissociation exist in this regard, their focus was limited to controlling the dynamics associated with excited surfaces with no barriers [18]. Here we explicitly consider controlling the photochemistry of $^1\pi\sigma^*$ ($^1A_2$) state that solely arises out of its repulsive character after the barrier. Thus our control studies may be useful in the case of excited state proton transfer/abstraction with barriers, which is often the case in large molecules.

A direct transition from the S_0 to the $^1\pi\sigma^*$ ($^1A_2$) state of pyrrole is understandably optically forbidden in first order. However, recent experiments carried out with 250 and 238 nm radiations directly probed the $^1\pi\sigma^*$ state and the interplay between barrier tunneling and barrier crossing dynamics was discussed [11]. Theoretically, the $^1\pi\sigma^*$ mixes with the optically allowed states and therefore the transition is justified and verified experimentally. Therefore, we considered the initial condition as the vertically placed $|0,0\rangle$ packet (an eigenstate of S_0) in the $^1\pi\sigma^*$ state. The transition dipole moment (TDM) in the present work is assumed to have a certain arbitrary value so that a pulse of moderately high intensity and sufficiently longer duration can, in fact, induce transition in the dipole forbidden situation. Also, in the recent past, multi-state and multi-mode dynamics of pyrrole has been extensively studied in field free conditions [10, 14].

In the following we present a control mechanism by designing optimal laser pulse(s) which efficiently transforms the slow tunneling dynamics into fast dynamics and monitors the passage of WP through CI and gives rise to a branching ratio of photoproducts. The well known optimal control theory (OCT) [19, 20] combined with vibronic coupling theory and time-dependent wavepacket propagation (TDWP) method is utilized to accomplish the task as described in Chapter no. 6. However, we present a brief review on the theoretical aspects to make it clear the differences in the parameter values used in this work.

7.1 Theory

7.1.1 Quantum dynamics and OCT

As in the previous chapter, in this study we have employed the 2×2 diabatic electronic Hamiltonian including a laser-molecule interaction term (in the dipole approximation) in the off-diagonal diabatic $S_0/^1\pi\sigma^*(^1A_2)$ electronic coupling. The nuclear dynamics on coupled states is studied by solving the time-dependent Schrödinger equation (TDSE) [cf., Eq. (6.4)]

After the initial excitation of a $|n_r, n_{Q_{11}}\rangle$ wavefunction of the S_0 state to the $^1\pi\sigma^*$ state the cost functional for the N-H dissociation process is defined by

$$J\left[\epsilon(t)\right] = \int_0^T \frac{\hbar}{\mu} Im\left[\Psi^*(r,t)\frac{\partial}{\partial r}\Psi(r,t)\right]_{r=r_d} dt - \alpha_0 \int_0^T \left[\epsilon(t)\right]^2 dt, \qquad (7.1)$$

The first term in the RHS of the above equation is the total dissociation probability (the time integrated flux of the WP reaching the dissociation asymptotes) which serves as an objective in J. The dissociative flux is calculated along an analysis line at the asymptotes at, $r_d = 11.976$ a.u., as shown in Fig. 6.3. Afterwards a sine type of damping function [29] is activated at, $r = 13.5$ a.u., to absorb the WP in order to prevent its reflection and wraparounds at the grid boundaries. The second term in the RHS (in Eq. 3) is the penalty constraint to lower the fluence of the pulse with electric field component $\epsilon(t)$ to avoid the undesirable physical processes (e.g. ionization) caused by high field strengths. The quantity α_0 is a penalty factor. The aim is to optimize (maximize) this field-dependent functional $J\left[\epsilon(t)\right]$ using genetic algorithm (GA, in particular micro-GA) based optimization methods [30–33], to arrive at the desired goal to validate the dissociation mechanism proposed.

The guess field in GA is taken as in Eq. (6.7). This amplitude is varied from 0 to 0.03 a.u. and the frequency is varied from 4173 cm^{-1} to 15146 cm^{-1} (range of 0.05 a.u.) to optimize the cost functional. The envelop function, $s(t)$, is defined same as in the previous chapter [cf., Eq. (2.102)]. A total time duration of 90000 a.u, ($\sim$ 2169 fs) is considered and a penalty factor α_0 value of 0.001 a.u. is considered here. Using GA, different possible combinations of the amplitude (ϵ), two time parameters (t_1 and t_2) and frequency (ω) are searched as described in Chapter 2. The calculation took 23 generations for the cost functional to reach convergence using values for the GA parameters as suggested in Ref. [37].

7.2 Results and discussion

In the field free dynamics of the $|0,0\rangle$ WP [cf., Fig. 6.2] launched on the $^1\pi\sigma^*$ ($^1A_2$) state, the average energy of the WP ($\sim$ 0.26 eV) is about sixty percent of the barrier height ($\sim$ 0.4 eV). Therefore the barrier crossing path and the upper adiabatic dissociation channel remains closed in this situation. Quantum tunneling is the only possible path for this WP to dissociate through $^1\pi\sigma^*$ ($^1A_2$)/S_0 CI. Using the semiclassical Wentzel-Kramers-Brillouin (WKB) formula a transmission probability of $\sim$ 0.6 is estimated for a choice of the barrier width of 0.1112 a_0. This reveals that about 60% of the WP on the $^1\pi\sigma^*$ state can tunnel through the barrier over a longer time period. Even after tunneling, the WP does not acquire enough energy to reach the upper adiabatic dissociation limit. The dissociation probability calculated along the flux line (as shown in Fig. 6.3) on the adiabatic asymptotes is plotted as a function of time in Fig. 7.1 and shown by the dashed line. It can be seen from the figure that in this situation the dissociation solely takes place on the lower adiabatic asymptote. Examination of time-dependence of diabatic and adiabatic electronic populations [cf., Fig. 6.5(b)] in this situation reveals that the diabatic populations essentially do not change in time while adiabatic populations exhibit a monotonic change in time. This implies that after an initial excitation, the WP remains on the $^1\pi\sigma^*$ diabat. The $^1\pi\sigma^*$ diabat asymptotically correlates to the lower adiabat. Therefore, the population of the latter grows and that of the upper adiabat depletes in time. The cumulative dissociation probability in conjunction with the population dynamics supports the inference that the dynamics of the $|0,0\rangle$ wavefunction is governed by the barrier tunneling followed by a passage through the $^1\pi\sigma^*$/ S_0 CI in the field free condition.

It is obvious from the above discussions that the barrier crossing is negligible in the dynamics of the $|0,0\rangle$ wavefunction in absence of a laser pulse. In this situation, vibrationally excited initial WPs have been shown to enhance the

barrier crossing dynamics in addition to the tunneling [7]. The mechanism proposed in the present work relies on a control pulse which initiates a sequence of events. A part of the WP initially excited to $^1\pi\sigma^*$ state is first dumped back to the S_0 state by the pulse. The latter creates a vibrationally hot WP on the S_0 state which spreads along r as well as Q_{11} and subsequently reaches the CI. The part of the WP remaining on the $^1\pi\sigma^*$ state simultaneously and relatively slowly tunnels through the barrier and reaches CI and interferes with the vibrationally hot S_0 WP components reaching there. The composite WP moves towards the lower adiabatic dissociation limit. Since the control pulse is active its pump component remains operational and the composite WP experiences an effective pump action of the pulse in the coordinate region beyond CI before it dissociates. This is because in this region, the carrier frequency ($\sim$ 8905 cm^{-1}) of the optimized pulse is near-resonant with the asymptotic energy gap ($\sim$ 8850-8920 cm^{-1}) at $r \approx 7.86$ a.u. The TDM has a nearly constant value of $\sim$0.1350 a.u. (calculated *ab intio*) in this asymptotic region. In that way the pumped components of the composite WP dissociate on the upper adiabatic channel and the remaining ones on the lower channel. This mechanism is further confirmed by switching off the laser-molecule interaction beyond CI. In such a situation the dissociation probability on the upper adiabatic channel becomes minimal ($\sim$ 0.1). This shows that the optimized pulse acquires the capability of producing photoproducts through the upper dissociation channel which is closed otherwise. This simultaneous dump and pump action of the control pulse remains on during entire course of the dynamics along with the nonadiabatic passage of the WP through CI.

An initial infrared pulse of frequency $\sim$ 4173 cm^{-1} is guessed based on the energy difference between $|0,0\rangle$ and $|1,1\rangle$ vibrational levels. This guess pulse is then optimized. The optimal pulse (shown as an insert in Fig. 7.1(a)) has a maximum amplitude of 0.0216 a.u.($\sim$ 14 TW/cm^2) with associated pulse shape

parameters, t_1 and t_2, values $\sim$ 585 fs and $\sim$ 1506 fs, respectively. The optimal pulse has a carrier frequency of $\sim$ 8905 cm^{-1} ($\sim$ 1200 nm) as obtained from the power spectrum (shown as an insert in Fig. 7.1(a)). As stated above, action of this pulse on the WP on the $^1\pi\sigma^*$ state transfers population to the vibrationally excited levels of S_0 which acquires nodal structure along r and also Q_{11} [cf., Figs. 7.1(b-c)]. Finally, a part of it reaches the dissociation asymptotes directly and a part of it is transferred back to the $^1\pi\sigma^*$ state by the pump component of the control pulse which remains on throughout the dynamics.

It can be seen from Figs. 7.1(d-e) that the WP component on the $^1\pi\sigma^*$ state also acquires nodal structure beyond the barrier at $r \approx 5.1$ a.u. This originates from WP components that arrive back to the $^1\pi\sigma^*$ state because of the pump action of the control pulse. These components possess enough energy to dissociate into both the asymptotes. The pump action appears to be more effective after the WP crosses the CI as explicitly confirmed by switching off the laser-molecule interactions at different regions of the coordinate space. The upper dissociation channel appears to be minor when this interaction is switched off beyond $r \approx 6.2$ a.u.

In order to understand the WP dynamics portrayed in Fig. 7.1(b-e) better, we examined one-dimensional cuts of the WP probability density along the coupling coordinate Q_{11} [cf., Figs. 7.2 and 7.3] at the two time scales of the WP snapshots [cf., Fig. 7.1(b-e)]. It is observed that in absence of the pulse the transferred WP on the S_0 diabatic state acquires a nearly symmetrical node at $Q_{11} = 0$. The diabatic coupling is an odd function of Q_{11} and since WP can return only via CI such a node appears in this situation. This is a clear signature of well known geometric phase effect [13]. In presence of the pulse the situation becomes quite irregular, the dumped WP on the S_0 diabat often develops non-symmetrical nodal structure away from $Q_{11} = 0$ because of laser-molecule interaction and interference effects as can be seen from Fig. 7.1(b-c). In absence of the pulse the

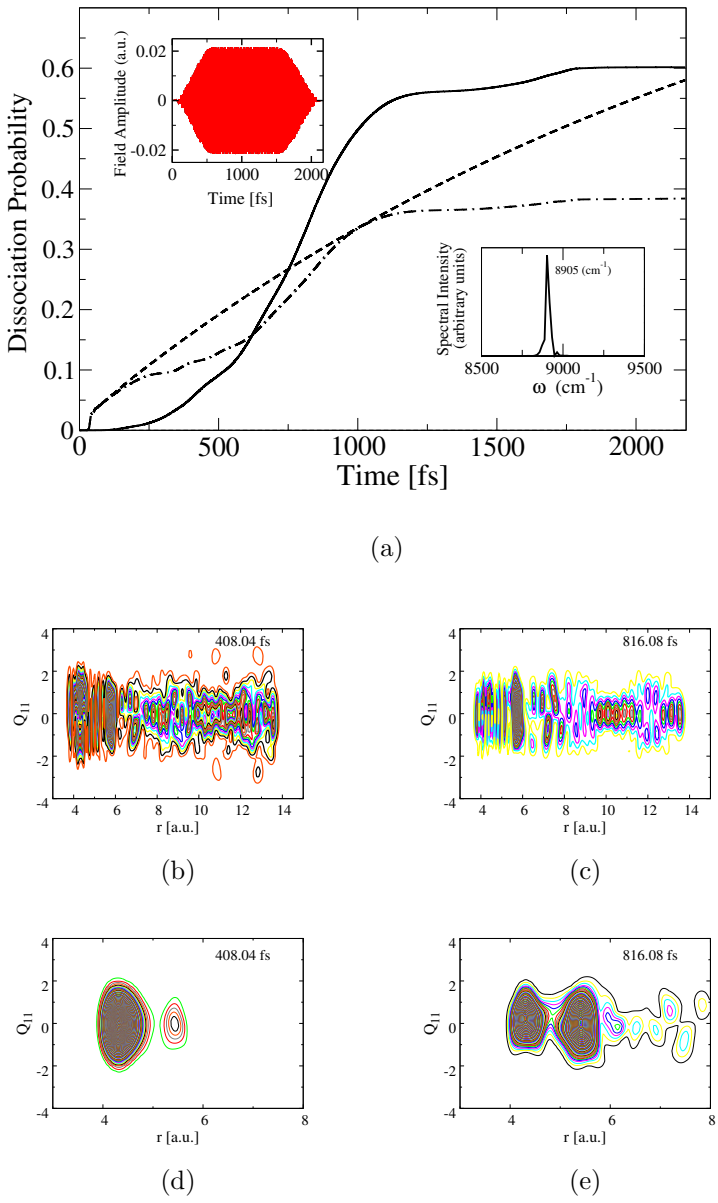

Figure 7.1: (a) Dissociation probabilities as functions of time. The dashed line represents the dissociation to the lower adiabatic asymptote in absence of the field. The dissociation to the lower and upper adiabats in presence of the field is shown by dot-dashed and solid lines, respectively. The optimized laser pulse in the time domain is shown as an insert at the upper left corner and its frequency domain structure is shown as an insert at the lower right corner. (b-e) Snapshot of the WP components evolving on the diabatic S_0 state (b-c) and diabatic $\pi\sigma^*$ state (d-e) at different times during the field driven dynamics (see text for details).

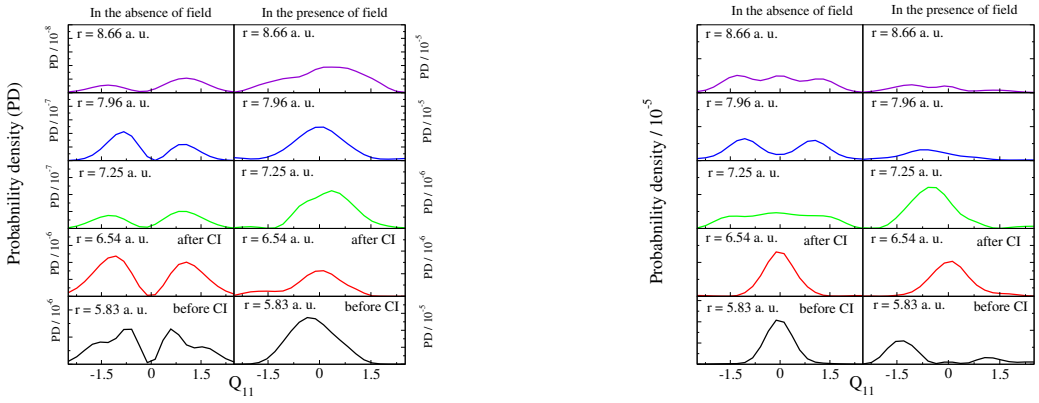

Figure 7.2: Probability density cuts along Q_{11} at different values of r, of both the ground diabatic (a) and excited diabatic packets (b). The snapshots are taken at 408.04 fs time for both in absence as well as in presence of the field.

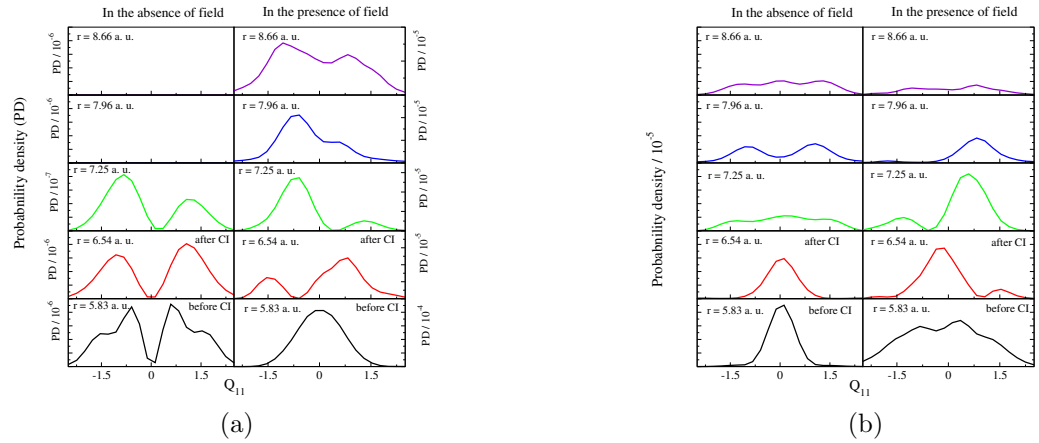

Figure 7.3: Same as the above figure but the snapshots are taken at 816.08 fs time.

$|0,0\rangle$ WP transferred to the $^1\pi\sigma^*$ diabat on the other hand does not acquire any node. This is because the WP component evolving on the $^1\pi\sigma^*$ diabat retains the overall vibronic symmetry. In presence of the pulse non-symmetrical nodal structure often appears [cf., Fig. 7.1(d-e)] because of interference with the WP components due to pump action of the pulse as stated above.

In contrast to the field free case, the laser driven dynamics yields dissociation products on both the adiabatic asymptotes. The dissociation probabilities calculated on the lower and upper adiabatic asymptotes are shown as dot-dashed and solid lines, respectively, in Fig. 7.1(a). It can be seen that, in this situation predominant dissociation takes place via upper adiabatic asymptote. Quantitatively, it is much different from the dissociation achieved by a vibrationally excited ($|1,1\rangle$) packet that reaches the upper adiabatic asymptote through the barrier crossing mechanism in the field free case [7]. In Fig. 7.4(a), the corresponding population dynamics driven by the optimal pulse is shown. It can be seen that the population of both the diabatic states changes in time. As time progresses both the diabatic $^1\pi\sigma^*$ and adiabatic upper state populations (A&C in Fig. 7.4(a), respectively) decrease and those of diabatic S_0 and adiabatic lower state (B&D in Fig. 7.4(a), respectively) increase. The maximum population transfer between the two electronic states occurs within ~ 1.0 ps. And by this time the dissociation probabilities of both the channels attain a peak value as can be seen from Fig. 7.1(a). At longer times the dissociation probabilities saturate at 60% and 40% on the upper and lower adiabatic asymptotes, respectively. This shows that almost entire population is driven to dissociation at the end of the pulse duration. It is worthwhile to point out that intramolecular vibrational relaxation (IVR) turns out to be insignificant ($< \sim 1.2\%$) in this case as confirmed by minimal overlap of the time evolved WP with the eigenvectors of the low-lying vibrational levels of the S_0 state at the end of the pulse duration.

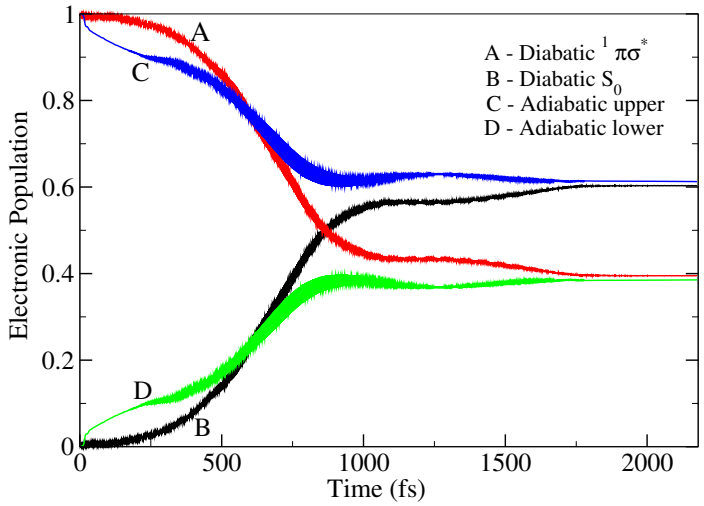

(a)

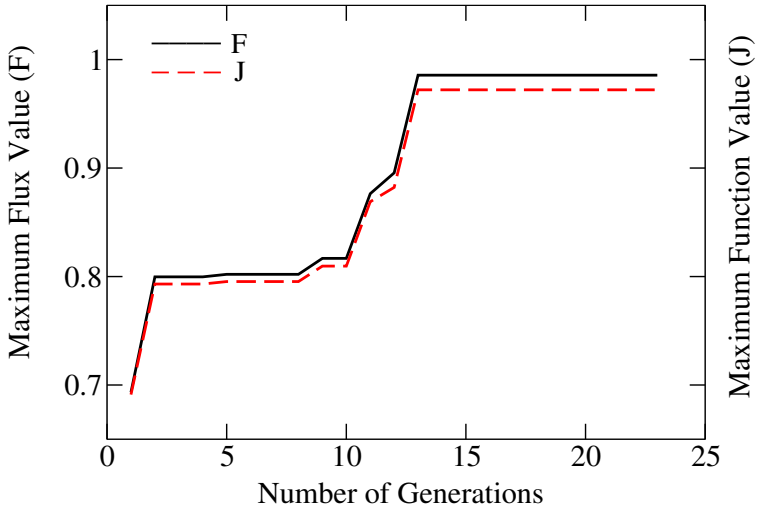

(b)

Figure 7.4: Population dynamics and convergence behaviour: (a) Time dependence of adiabatic and diabatic electronic populations in the field driven photodissociation dynamics of pyrrole. The line types are given in the legend and discussed in the text, (b) Convergence behaviour of cost functional (J) and total flux (F) with the number of generations shown by the dashed and solid lines, respectively.

The laser driven dynamics is much faster as compared to the field free case. An analysis of the average energy of the WP on the S_0 and $^1\pi\sigma^*$ state in presence of pulse reveals that the packet on both the states has components with sufficient energy to reach the dissociation limit during the entire course of dynamics. The average energies of these packets are shown in Fig. 7.5(a). The sudden drop in energy of the S_0 diabatic WP is due to the removal of high energy components of the WP by the damping function activated at the grid boundaries. As can be seen it causes rise of dissociation probability between 1–1.25 ps [cf., Fig. 7.1(a)]. The time-frequency analysis of the laser pulse using Husimi distribution [38] is shown in Fig. 4(b). As can be seen from the latter figure, the maximum contribution to the transition comes from the pulse in the frequency range $\sim$ 8850–8950 cm^{-1} between $\sim$ 500 to 1600 fs. This is on par with the population dynamics [cf., Fig. 7.4(a)] and the associated dissociation probabilities [cf., Fig. 7.1(a)].

Calculations are also carried out keeping the initial guess value of the frequency (i.e., $\sim$ 4173 cm^{-1}) fixed during optimization while varying the amplitude and time parameters. The results of these fixed frequency calculations are presented in Fig. 7.6. A comparative study of these results with the frequency optimized results reveals that, in the latter case dissociation probability of the upper channel is enhanced [cf., Fig. 7.1(a) versus Fig. 7.6(d)]. The underlying reason is attributed to the less effective electronic population transfer between the two diabatic states [cf., Fig. 7.6(e)] by the pulse in action and its relatively less energy, in the fixed frequency case as compared to the frequency optimized case.

Checks are also exercised by taking frequencies of the initial guess pulse close to the optimal result (i.e., either side of 8905 cm^{-1} with -100 cm^{-1} and +300 cm^{-1}) and performing fixed frequency calculations. This confirms that the control is robust, that is small variations in the optimal field parameters do not change the fidelity significantly. As can be seen from Fig. 7.8(a), a relatively

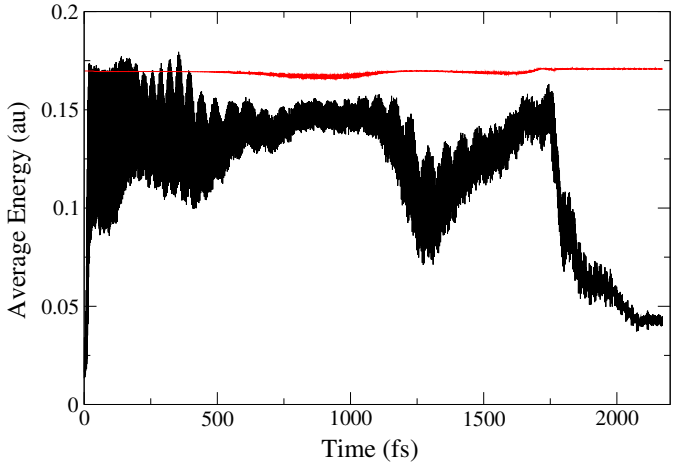

(a)

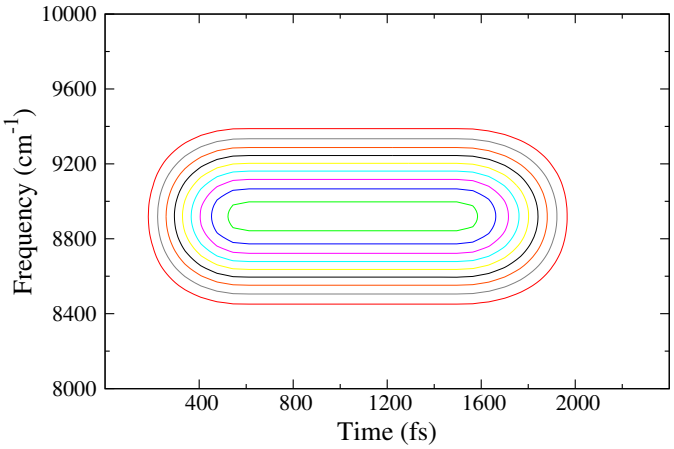

(b)

Figure 7.5: Average energies of diabatic packets and Husimi plot of the optimal field: (a) Average energy of the WP evolving on the S_0 (black line) and $\pi\sigma^*$ (red line) diabatic states as a function of time, (b) Husimi plot of the time-frequency characteristics of the optimally controlled laser pulse.

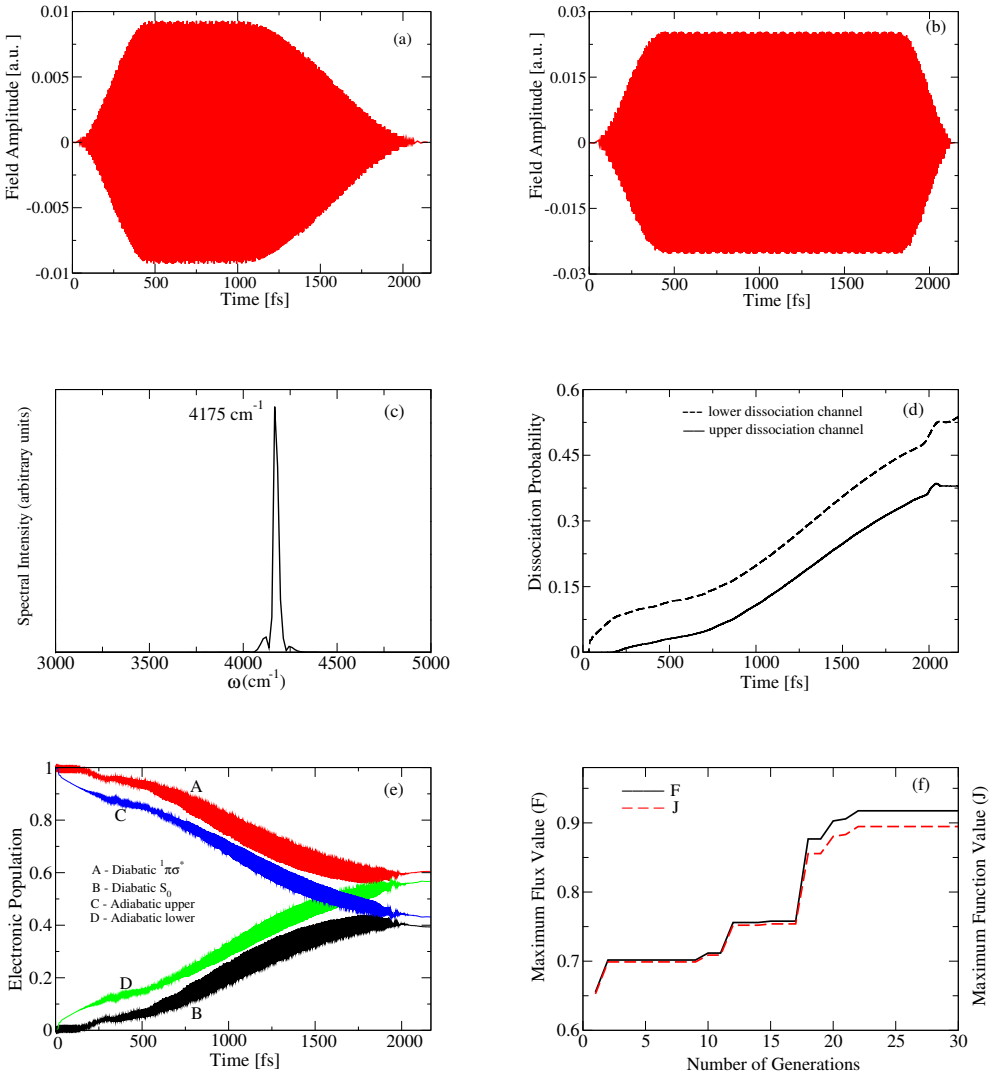

Figure 7.6: **Results of fixed frequency calculations**: figures (a) to (f) are initial guess field, optimal field, frequency spectrum, dissociation probability, diabatic-adiabatic population dynamics and convergence behaviour of cost functional (J) and total flux (F), respectively.

complex pulse (or rather a train of pulses) with variations in amplitude profile yields quantitatively somewhat different net dissociation probability (~ 0.8) [cf., Fig. 7.8(c)] compared to frequency optimized results (~ 1.0). However, the overall mechanism remains unaltered. It can also be seen from the frequency structure [cf., Fig. 7.8(b)] of this moderately complicated time-dependent field that the contributions to transitions between the two electronic states can come from three carrier frequencies depending upon their relative intensity, to effectively yield photoproducts. This is unlike the case of frequency optimized results where a single carrier frequency of the time-dependent field [cf., Fig. 7.1(a)] is involved in during the control dynamics. Therefore, the alternative control mechanism to photodissociation of pyrrole can be brought about not only by optimal pulses which have seemingly simple shape but by moderately complicated optimal pulses also. Hence the power of optimization lies in finding a special combination of amplitude, frequency and pulse shape parameters ($t1$ and $t2$) for a given initial guess, to achieve a successful control.

In order to further validate the dynamical control mechanism emerged above in the two states and two modes model, we extended the model by including two more relevant coupling modes of A_2 symmetry. These modes are designated as Q_{12} and Q_{10}. Following the work of Ref. [10], we constructed an effective coupling mode as, $Q_{eff} = \sum_c \frac{\lambda_c}{\lambda_{eff}} Q_c$. In this equation, λ_c, λ_{eff} are coupling constants of the individual coupling modes and the effective coupling mode, respectively. The definitions of these coupling coordinates are shown in Fig. 7.2 and the values of corresponding coupling constants and frequencies are presented in table 7.1. The results of this calculations are shown in Fig. 7.9. It can be seen from the time profile of the optimized field [shown as an insert in Fig. 7.9(a)], its corresponding frequency spectrum [shown as an insert in Fig. 7.9(a)] and the resulting dynamical outcomes, such as dissociation probabilities [cf., Fig. 7.9(a)] and populations [cf., Fig. 7.9(b)] that the mechanistic details of the dynamics

Table 7.1: Coupling modes belonging to A_2 symmetry, their respective frequencies (ω) and the corresponding linear coupling parameter (λ_c) values associated with $^1A_2(\pi\sigma^*)$-S_0 CI.

Mode	ω (eV)	λ_c (eV)
Q_{10}	0.1022	0.0430
Q_{11}	0.0830	0.1110
Q_{12}	0.0756	0.0350
Q_{eff}	0.1310	0.1240

remain same as discussed above in the case of frequency optimized calculations involving Q_{11} only [cf., Fig. 7.1(a) and Fig. 7.4(a)]. However, in this case the action of optimized pulse whose peak amplitude/carrier frequency (in the range $\sim$ 0.0145 a.u./10220 cm^{-1}) is lower/higher than that of the latter case ($\sim$ 0.0216 a.u./8095 cm^{-1}), is confined to a longer time duration ($\sim$ 241 fs - $\sim$ 1450 fs, obtained by its Husimi transform. The action of the optimized pulse in that duration is clearly reflected in the population dynamics [cf., Fig. 7.9(b)] and flux behaviour [cf., Fig. 7.9(a)]. It is clear from Figs. 7.9(a) and 7.9(b) that the relative increase in dissociation rate and rate of population transfer as compared to those shown in Figs. 7.1(a) and 7.4(a), is due to the inclusion of additional coupling modes, as expected. Nevertheless, the total dissociation probability remains almost same and an interpretation of these results follow same line of arguments as of those shown in Figs. 7.1(a) and 7.4(a). IVR is minimal in this case also. Therefore, in this sense, the theoretical model captured most of the essential photodynamical features of the pyrrole molecule.

The convergence behaviour set up by the GA with the number of generations evolved is shown in Fig. 7.4(b). The plot(s) shows the maximum flux (F), and cost functional (J) values are more or less comparable and keep increasing in steps until a constant value is reached for the final generations.

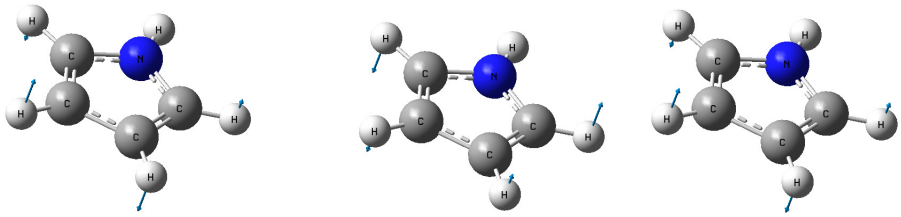

(a) (b) (c)

Figure 7.7: **The definition of each coupling mode used in the calculations**: a) Q_{10} normal mode, b) Q_{11} normal mode and c) Q_{12} normal mode.

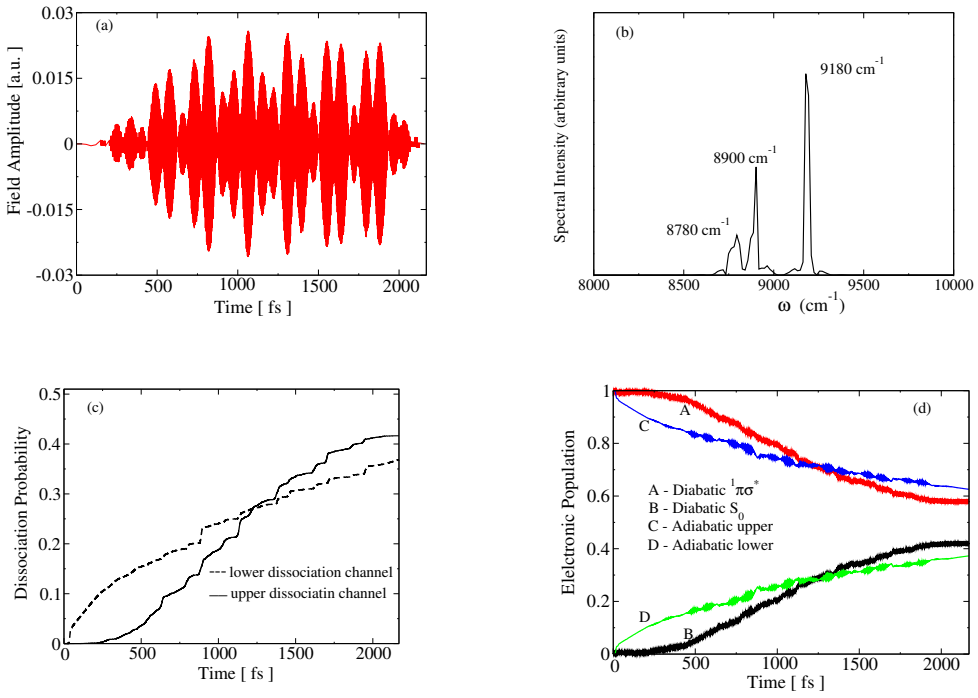

Figure 7.8: **Results of calculations by varying the frequency**: figures (a) to (d) are optimal field, frequency spectrum, time-integrated flux and diabatic-adiabatic population dynamics, respectively.

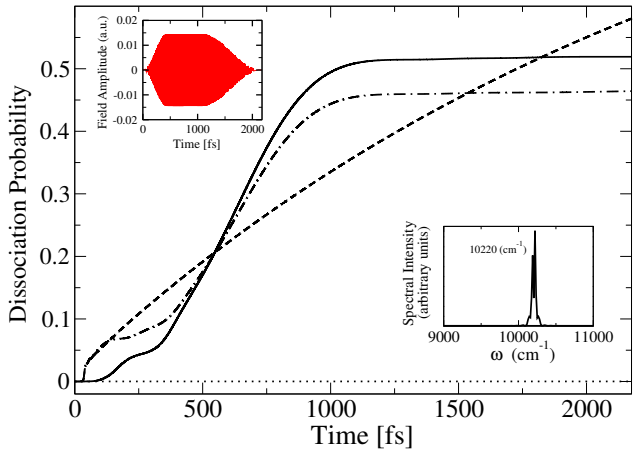

(a)

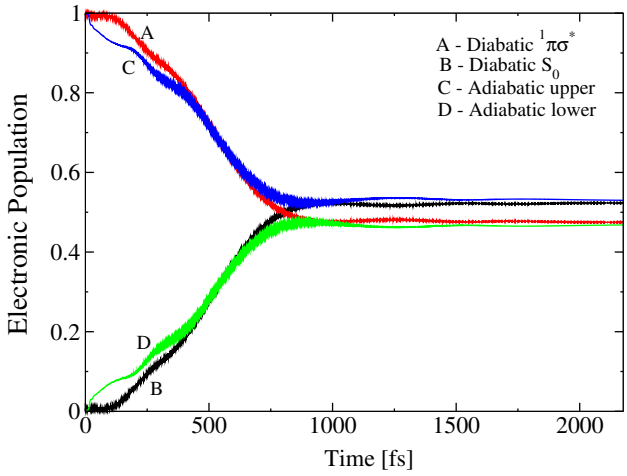

(b)

Figure 7.9: **Results of calculations with effective coupling mode**: (a) Dissociation probability as functions of time. The dashed line represents the dissociation to the lower adiabatic asymptote in absence of the field. The dissociation to the lower and upper adiabats in presence of the field is shown by dot-dashed and solid lines, respectively. The optimized laser pulse in the time domain is shown as an insert at the upper left corner and its frequency domain structure is shown as an insert at the lower right corner. (b) Time dependence of adiabatic and diabatic electronic populations in the field driven photodissociation dynamics of pyrrole. The line types are given in the legend follow same as that of Fig. 7.4(a).

7.3 Summarizing remarks

In summary, an alternative and efficient photodissociation mechanism of pyrrole on electronically coupled S_0-$^1\pi\sigma^*$ states is developed by applying optimally controlled pulse. The dissociation dynamics is governed by the designed pulse(s) that acts after the initial excitation of the ground vibrational wavefunction of the S_0 (adiabatic) state to the $^1\pi\sigma^*$ (adiabatic) state. After the initiation, the system dynamically evolves with the pulse. The control pulse dumps a fraction of WP components on the $^1\pi\sigma^*$ state to the S_0 state. These dumped WP components on the S_0 possess enough energy along the reaction coordinate (N-H stretch). A fast dynamics on the S_0 state in addition to slow tunneling of remaining WP components on the $^1\pi\sigma^*$ state follow thereafter. The WP components evolving on both the states reach the $^1\pi\sigma^*/S_0$ CI and dissociate into both the upper and lower adiabatic channels. The dissociation to the upper channel is mainly facilitated by the pump components of the control pulse (which remains on throughout the dynamics) after the packet crosses CI and this dissociation dominates at longer times.

An increase in the energy of the time evolved WP increases the dissociation probability of the upper channel. This is explicitly verified by utilizing control pulses with different energy. The barrier crossing path, which opens up the upper adiabatic asymptote in the field free case is closed for the $|0,0\rangle$ packet. With the aid of an optimally controlled laser pulse dissociation to the upper adiabatic asymptote is accomplished here through an alternative path. The optimized pulse has a smooth profile in time and is highly band-width limited. Such simple pulse shapes are experimentally realizable.

Bibliography

[1] M. B. Robin, *Higher Excited State of Polyatomic Molecules*, Academic, New York, (1972).

[2] D. A. Blank, S. W. North, and Y. T. Lee, Chem. Phys. **187**, 35 (1994).

[3] A. L. Sobolewski, W. Domcke, C. Dedonder-Lardeux, and C. Jouvet, Phys. Chem. Chem. Phys. **4**, 1093 (2002).

[4] B. Cronin, M. G. D. Nix, R. H. Qadiri, and M. N. R. Ashfold, Phys. Chem. Chem. Phys. **6**, 5031 (2004).

[5] J. Wei, J. Riedel, A. Kuczmann, F. Renth, and F. Temps, Faraday Discuss. **127**, 267 (2004).

[6] H. Lippert, H. H. Ritze, I. V. Hertel, and W. Radloff, Chem. Phys. Chem. **5**, 1423 (2004).

[7] V. Vallet, Z. Lan, S. Mahapatra, A. L. Sobolewski, and W. Domcke, J. Chem. Phys. **123**, 144307 (2005).

[8] Z. Lan, A. Dupays, V. Vallet, S. Mahapatra, and W. Domcke, J. Photochem. Photobio. A. Chemistry. **190**, 177 (2007).

[9] Z. Lan and W. Domcke, Chem. Phys. **350**, 125 (2008).

[10] S. Faraji, M. Vazdar, V. Sivaranjana Reddy, M. Eckert-Maksic, H. Lischka, and H. Köppel, J. Chem. Phys. **135**, 15310 (2011).

[11] G. M. Roberts, C. A. Williams, H. Yu, A. S. Chatterley, J. D. Young, S. Ullrichb, and V. G. Stavros, Faraday Discuss. **163**, 95 (2013)

[12] M. Epshtein, A. Portnov, R. Kupfer, S. Rosenwaks, and I. Bar, J. Chem. Phys. **139**, 184201 (2013).

[13] F. Bouakline, Chem. Phys. **442**, 31 (2014).

[14] S. P. Neville and G. A. Worth, J. Chem. Phys. **140**, 034317 (2014).

[15] G. Wu, S. P. Neville, O. Schalk, T. Sekikawa, M. N. R. Ashfold, G. A. Worth, and A. Stolow, J. Chem. Phys. **142**, 074302 (2015).

[16] K. Saita, M. G. D. Nix, and D. V. Shalashilin, Phys. Chem. Chem. Phys. **25**, 16227 (2013).

[17] D. V. Makhov, K. Saita, T. J. Martinez, and D. V. Shalashilin, Phys. Chem. Chem. Phys. **17**, 3316 (2015).

[18] M. Abe, Y. Ohtsuki, Y. Fujimura, Z. Lan and W. Domcke, J. Chem. Phys. **123**, 224316 (2006).

[19] S. Shi and H. Rabitz, J. Chem. Phys. **92**, 364 (1990).

[20] W. Zhu, J. Botina, and H. Rabitz, J. Chem. Phys. **108**, 1953 (1998).

[21] K. Sunderman and R. de Vivie-Riedle, J. Chem. Phys. **110**, 1896 (1999).

[22] S. P. Shah and S. A. Rice, J. Chem. Phys. **113**, 6536 (2000).

[23] J. C. Light, I. P. Hamilton, and V. J. Lill, J. Chem. Phys. **82**, 1400 (1985).

[24] M. D. Feit, J. A. Fleck, Jr., and A. Steiger, J. Comput. Phys. **47**, 412 (1982).

[25] S. Mahapatra and H. Köppel, J. Chem. Phys. **109**, 1721 (1998).

[26] S. Ghosal and S. Mahapatra, J. Phys. Chem. A **109**, 1530 (2005).

[27] C. C. Marston and G. G. Balint-Kurti, J. Chem. Phys. **91**, 3571 (1989).

[28] G. G. Balint-Kurti, C. L. Ward, and C. C. Marston, Comput. Phys. Comm. **67**, 285 (1991).

[29] S. Mahapatra, N. Sathyamurthy, J. Chem. Soc., Faraday Trans. **97**, 9062 (1997).

[30] T. Brixner and G. Gerber, Chem. Phys. Chem. **4**, 418 (2003).

[31] P. Neuernberger, G. Vogt, T. Brixner, and G. Gerber, Phys. Chem. Chem. Phys. **9**, 2470 (2007).

[32] R. S. Judson and H. Rabitz, Phys. Rev. Lett. **68**, 1500 (1992).

[33] K. Krishnakumar, "Intelligent Control and Adaptive Systems", Proc. SPIE **1196**, 289 (1989).

[34] H. Köppel, W. Domcke, and L. S. Cederbaum, Adv. Chem. Phys. **57**, 59 (1984).

[35] U. Manthe and H. Köppel, J. Chem. Phys. 93, 345 **93**, 1658 (1990).

[36] U. Manthe, H. Köppel, and L. S. Cederbaum, J. Chem. Phys. **95**, 1708 (1991).

[37] S. Sharma, H. Singh, and G. G. Balint-Kurti, J. Chem. Phys. **132**, 064108 (2010).

[38] M. D. Davidovića, M. D. Davidovićb, and V. Vojisavljevicc, Acta. Phys. Polon. A **116**, 675 (2009).

Chapter 8

Summary and Future directions

In this thesis we have employed optimal control theory (OCT) for theoretical design of laser pulses for controlling quantum dynamics in order to achieve a prescribed dynamical goals. For this purpose, the OCT is combined with the time-dependent Schrödinger equation (TDSE) that governs the quantum dynamics under the action of such pulses. The problem of designing a suitable laser pulse(s) that achieves the maximum of a desired goal(s), is phrased as an optimization of light field dependent "cost functional" in OCT. The cost functional contains not only an objective term which is a measure of the extent of desired goal that is achieved and may also incorporate penalty term as a constraint on field intensity limits in order to minimize the laser fluence. This optimization problem is solved using two different optimization techniques- the conjugate gradient (CG) method and genetic algorithm (GA). We have designed both IR and UV-laser pulses for controlling quantum dynamics in for the processes that occur in single electronic surface as well as multiple electronic surfaces that involve nonadiabatic interaction.

The work in this thesis is about designing optimal laser pulses and examining the associated control mechanisms for controlling state selective (vibrational/electronic) population transfer, isomerization and photodissociation dynamics. The so designed optimal laser pulses and the resulting control

mechanisms are analysed using tools such as time-amplitude profile of pulse and its frequency spectrum and monitoring wavepacket (WP) evolution, population dynamics of different quantum states, etc., respectively. The quantum control dynamics studied in the present work include both within the Born-Oppenheimer (BO) approximation (adiabatic) and beyond BO (nonadiabatic). The molecular systems of interest considered in this work for the control tasks range from simple diatomic to relatively complex polyatomic molecules. The quantum dynamics of the molecular system during its control is treated with TDSE within the semiclassical dipole approximation. As mentioned above, this dynamical evolution taking as a constraint is combined with the numerical pulse shaping technique, OCT. Moreover, nonadiabatic quantum dynamics is treated using diabatic representation. Split-operator (SO)technique together with fast Fourier transforms (FFT) is used for time propagation of laser-driven quantum mechanical system.

Within the realm of quantum computing the use of quantum states as qubits is inevitable. This suggests the importance of preparation of coherent quantum states, for instance by using laser pulses. In this regard, we have designed infrared laser pulses using OCT in combination with conjugate gradient method. The optimal pulses are designed to perform coherent excitation that lead to selective population transfer between vibrational states of the diatomic molecule, HCl. Specifically, the control of fundamental and overtone transitions of a vibration are considered. We have also examined that the effect of variation of penalty factor on the control outcomes. During the optimization, the smooth switch on and off of laser pulses are ensured by Gaussian envelope function. The optimally controlled vibrational states could be used as qubits and the pulses as logic gates.

Our results indicate the possibility of designing an effective pulse(s) that can perform selective transitions of HCl molecule from a given molecular quantum state to the desired target state. We were able to achieve this with almost

100% transition probability for all the transitions studied. The optimal pulses obtained are found to be simple in time and frequency domain and are highly experimentally feasible. Peak amplitudes of all the optimally designed pulses are found to be within the experimentally realizable bounds. We have also demonstrated that a) for each pulse duration considered with decrease in the value of the penalty factor α_0, the field amplitude increases; b) As we increase the pulse duration for a particular α_0 for all the transitions, the amplitude of field decreases. Moreover, the insights of the control studies of HCl are useful as it acts as a prototype for other halides that participate in H-abstraction reactions which are plenty, in chemistry.

We have applied OCT to design laser pulses to promote chemical reactions in electronic ground state with the aid of electronic excited states as a mediator. The idea behind involving excited states is to surmount any barrier obstructing the reaction to occur in the ground state. This can be achieved by a process of pumping and a time-delayed dumping between the two electronic states. Moreover, a) the advancements in UV-Pulse shaping technology over corresponding IR technology and, b) relatively stronger transitions between electronic states than between vibrational states of a molecule, in general act as motivation for this electronic control.

Within the BO approximation, a controlled initiation of isomerization reaction (H-transfer) in the electronic ground state of malonaldehyde molecule is studied. The optimal initiation of H-transfer in malonaldehyde is achieved by the application of strong and short optimal UV-laser pulses designed using OCT in combination with CG method. This control mechanism, where we used the excited electronic potential as a mediator to initiate H-transfer from one oxygen to the other in the electronic ground state of the malonaldehyde, achieves product configuration about 90%. The role of electronic excited state, a harmonic surface, is to provide positive momentum to the Franck-Condon WP by virtue

of its steepness. By the momentum gained from the electronic excited state, the WP after a time-delayed ($\sim$ 10 fs) dumping, moves toward the product well with associated spreading and dephasing in time.

The results of the study show that the control dynamical outcomes within the Condon approximation for the transition dipole moment versus its more realistic value calculated *ab initio* found good agreement. Product configuration is achieved in good yields. The use of electronic excited states to control chemical reactions in ground state is both conceptually novel and simple and experimentally implementable. In this regard, optimization using the CG method along with the pulse shaping features gives results that allow for the possibility of experimental implementation of designed optimal pulses.

In an effort to study the control of nonadiabatic molecular dynamics (beyond BO), we have also applied OCT with GA optimization to design optimal UV-laser pulses for controlling H-transfer of malonaldehyde involving coupled electronic states in two dimensions (involving a tuning coordinate and a coupling coordinate). The objective here is, as above, to control isomerization reaction in the ground electronic state. For this purpose, we have designed optimal UV-laser pulse using OCT for maximizing the product isomer by its continuous effective pump followed by dump operation between the electronic states while there is nonadiabatic interaction due to the conical intersection (CI) between the excited states. The control mechanism operating here is quite different from the simple pump-dump scheme explored in one dimensional case. But the idea of using excited electronic states as mediators to control isomerization in ground state remains same. Using the designed optimal pulse we have successfully achieved a product isomer about 45% in this nonadiabatic scenario.

The results show that the simple optimal pulses can be designed for controlling isomerization involving multiple electronic states interacting nonadiabatically. In such a scenario, the product isomer is achieved in good yields.

The GA-based optimization technique is found to exhibit good convergence behaviour and yields simple pulses.

We have also applied OCT to design optimal pulses for effective control of photodissociation dynamics of pyrrole occuring on coupled S_0 and $^1\pi\sigma^*$ ($^1A_2$) electronic states. In this respect, at first, we have performed the initial vibrational state dependent photodissociation dynamics of pyrrole, in the presence of UV-laser pulses, via $^1\pi\sigma^*$ ($^1A_2$)/ S_0 conical Intersection (CI). The variation in the branching ratio between the two asymptotic channels for various initial conditions of the system is observed implicitly. The associated control mechanism(s) is examined. This leads to mode-specific control of the photodissociation on $^1\pi\sigma^*$ state.

We have further investigated, with the aid of an optimally designed control pulse, an efficient alternative control mechanism of $^1\pi\sigma^*$-photodissociation to widely known mode-specific control mechanism. For this we have carried out a first principles quantum dynamics study of N-H photodissociation of pyrrole on the S_0 and $^1\pi\sigma^*$ ($^1A_2$) coupled electronic states with optimally designed UV-laser pulse. A new route of photodissociation of pyrrole as compared to conventional barrier crossing mechanism, based on electronically coupled states was suggested. This path opens up electronic transitions, under the influence of a continuous action of pump-dump laser pulse, efficiently populating both the upper and lower adiabatic dissociation channels.

Our results show that excellent control outcomes are achieved in both the above cases i.e, barrier crossing mechanism by vibrational excitation as well as new alternative mechanism. Given the high experimental relevance of $^1\pi\sigma^*$-photochemistry in the recent past, the simple optimal pulses obtained in both cases by the use of GA based optimization worth an experimental implementation. The alternative control mechanism suggested is found out to be robust and is explicitly checked by performing frequency shift (-100 cm^{-1} and

+300 cm^{-1}) calculations close to the optimal result and calculations involving additional coupling modes. These calculations give rise both qualitatively and quantitatively similar results confirming robustness of the mechanism.

Future Directions:

1. As far as preparation of coherent vibrational states are concerned, it would be interesting to see the maintenance of coherence when the effect of molecular environment (e.g. a thermal bath of harmonic oscillators) is concerned. In such a situtation controlling decoherence should be addressed based on density matrix based approach.

2. It would be interesting to consider further the nonadiabatic interaction between the ground electronic state and the excited electronic states of malonaldehyde with realistic transition dipole moments and explore the possibility of H-transfer control using shaped laser pulses in the presence of multiple CIs. For this, first of all a relevant coupling mode must be identified and then obtain the potential energies as functions of it.

3. In the case of pyrrole, further extensions of the control work can be made by including the optically bright $^1\pi\pi^*$ state and carry out the calculations. Furthermore, calculating dressed state potentials and interpretation of the alternative mechanism in terms of non-resonant dynamic stark effect could give additional insights of the control dynamics.

4. With the expertise gained from the work of this thesis, it is natural to deal with problems involving multi-states and multi modes. In this regard a problem that we have in mind in near future is the control of quantum yield of fluorescence from S_2 state of Hexafluorobenzene in the presence of CIs with S_1 along the totally symmetric vibrational modes. OCT-MCTDH package is used to treat this multi-mode and multi-state problem.

Appendix A

Finding the leading error term in the split-operator method

Consider the left hand side of the the Eq. (2.134) and expand as shown below (here we drop the overhead hat symbol on operators for simplicity),

$$\begin{aligned} e^{\frac{-i\hat{H}}{\hbar}dt} &= e^{\frac{-i(T+V)dt}{\hbar}} = 1 - i(T+V)\frac{dt}{\hbar} \\ &\quad + \frac{(-i)^2(T+V)^2dt^2}{2\hbar^2} + \frac{(-i)^3(T+V)^3dt^3}{3!\hbar^3} + \cdots \\ &= 1 - i(T+V)\frac{dt}{\hbar} - \frac{(T^2+V^2+TV+VT)dt^2}{2\hbar^2} \\ &\quad + i\frac{(T^3+TVT+T^2V+TV^2+VT^2+V^2T+VTV+V^3)dt^3}{3!\hbar^3} \\ &\quad + \cdots \end{aligned} \tag{A.1}$$

Now consider the right hand side of the equation and expand it as shown below,

$$\begin{aligned} e^{-iVdt/2\hbar}e^{-iTdt/\hbar}e^{-iVdt/2\hbar} &= \left[1 - iV\frac{dt}{2\hbar} + \frac{(-iVdt)^2}{8\hbar^2} + \cdots\right]\left[1 - iT\frac{dt}{\hbar} + \frac{(-iTdt)^2}{2\hbar^2} + \cdots\right] \\ &\quad \times \left[1 - iV\frac{dt}{2\hbar} + \frac{(-iVdt)^2}{8\hbar^2} + \cdots\right] \\ &= 1 - i(T+V)\frac{dt}{\hbar} - \frac{(T^2+V^2+TV+VT)dt^2}{2\hbar^2} \\ &\quad + i\left(\frac{V^3}{6} + \frac{T^3}{6} + \frac{VTV}{4} + \frac{V^2T}{8} + \frac{VT^2}{4} + \frac{T^2V}{4} + \frac{TV^2}{8}\right)\frac{dt^3}{\hbar^3} \\ &\quad + \cdots \end{aligned} \tag{A.2}$$

Comparing the exact expression, Eq. (A.1), with the approximation, Eq. (A.4) the leading error term is obtained as follows,

$$\text{Error} = i\frac{dt^3}{\hbar^3}\left(\frac{T\,[V,T]}{12} + \frac{[T,V]\,T}{12} + \frac{[T,V]\,V}{24} + \frac{V\,[V,T]}{24}\right) \tag{A.3}$$

$$= i\frac{dt^3}{\hbar^3}\left(\frac{[T,[V,T]}{12} + \frac{[V,[V,T]}{24}\right). \tag{A.4}$$

Appendix B

Derivation of pulse design equations

The cost functional reads as (for simplicity in all the expression below we drop the vector aspects (i.e., bold form notation) of the dipole moment μ and ϵ its conjugate as well):

$$J[\epsilon(t)] = \lim_{T\to\infty} \langle\psi(T)|\hat{O}|\psi(T)\rangle - \alpha_0 \int_0^T |\epsilon(t)|^2 dt - 2Re\left[\int_0^T \langle\chi(t)|\frac{\partial}{\partial t} + i\hat{H}|\psi(t)\rangle\right] \tag{B.1}$$

where

$$\hat{H} = \begin{pmatrix} \hat{H}_e & -hat\mu\epsilon^*(t) \\ -\hat{\mu}\epsilon(t) & \hat{H}_g \end{pmatrix} \tag{B.2}$$

and

$$\psi = \begin{pmatrix} \psi_e \\ \psi_g \end{pmatrix} \quad ; \quad \chi = \begin{pmatrix} \chi_e \\ \chi_g \end{pmatrix} \tag{B.3}$$

As long as ψ satisfies the TDSE the second term in the right hand side of Eq. (B.1) will vanish for any χ. The role of this term as a constraint is to deconstrain ψ and ϵ. This will remove the complicated dependence of the former on the latter. Applying the integration by parts to the second term, we obtain the Eq. (B.1) as

$$J = \lim_{T\to\infty} \langle\psi(T)|\hat{O}|\psi(T)\rangle - 2Re\langle\chi|\psi\rangle|_0^T + 2Re\int_0^T dt\left\{\langle\chi(t)|\frac{H}{i\hbar}|\psi(t)\rangle + \langle\chi|\psi\rangle\right\} - \lambda\int_0^T dt|\epsilon(t)|^2. \tag{B.4}$$

For a stationary point, the variation of the functional, J, with respect to $\psi(t)$, $\psi(T)$, $\epsilon(t)$ and $\epsilon^*(t)$ can be taken independently and made them to be zero:

$$\frac{\delta J}{\delta \psi(t)} = 0 \qquad \frac{\delta J}{\delta \psi(T)} = 0 \qquad \frac{\delta J}{\delta \epsilon(t)} = 0 \qquad \frac{\delta J}{\delta \epsilon^*(t)} = 0. \tag{B.5}$$

The variation of J

$$\begin{aligned}
\delta J &= \lim_{T\to\infty} 2Re\langle\psi(T)|\hat{O}|\delta\psi(T)\rangle - 2Re\langle\chi(T)|\delta\psi(T)\rangle \\
&+ 2Re\int_0^T dt\left\{\left\langle \frac{H}{-i\hbar}\chi(t)\right|\left.\delta\psi(t)\right\rangle + \langle\dot{\chi}(t)|\delta\psi(t)\rangle\right\} \\
&+ 2Re\int_0^T dt\left\{\left\langle \chi(t)\right|\left.\frac{1}{i\hbar}\frac{\delta H}{\delta\epsilon^*(t)}\right|\psi(t)\right\rangle\delta\epsilon^*(t) + \left\langle \chi(t)\right|\left.\frac{1}{i\hbar}\frac{\delta H}{\delta\epsilon(t)}\right|\psi(t)\right\rangle\delta\epsilon(t)\right\} \\
&- \lambda\int_0^T dt\epsilon(t)\delta\epsilon^*(t) - \lambda\int_0^T dt\epsilon^*(t)\delta\epsilon(t).
\end{aligned} \tag{B.6}$$

Let us rearrange the terms and use complex conjugate of the term proportional to $\delta\epsilon^*(t)$ in Eq. (B.6):

$$\begin{aligned}
\delta J &= \lim_{T\to\infty} 2Re\{\langle\psi(T)|\hat{O} - \langle\chi(T)|\}|\delta\psi(T)\rangle \\
&+ 2Re\int_0^T dt\left\{\left\langle \frac{H}{-i\hbar}\chi(t)\right| + \langle\dot{\chi}(t)|\right\}|\delta\psi(t)\rangle \\
&+ 2Re\int_0^T dt\left\{\left\langle \chi(t)\right|\left.\frac{1}{i\hbar}\frac{\delta H}{\delta\epsilon^*(t)}\right|\psi(t)\right\rangle + \left\langle \psi(t)\right|\left.\frac{1}{i\hbar}\frac{\delta H}{\delta\epsilon^*(t)}\right|\chi(t)\right\rangle \\
&- \lambda\int_0^T dt\epsilon(t)\Bigg\}\delta\epsilon^*(t) - \lambda\int_0^T dt\epsilon^*(t)\delta\epsilon(t).
\end{aligned} \tag{B.7}$$

where [from Eq. (B.2)],

$$\frac{\partial H}{\partial\epsilon^*} = \begin{pmatrix} 0 & -\mu \\ 0 & 0 \end{pmatrix}, \qquad \frac{\partial H}{\partial\epsilon} = \begin{pmatrix} 0 & 0 \\ -\mu & 0 \end{pmatrix}. \tag{B.8}$$

From the first, second and third terms of Eq. (B.7) the following equations

are straightforward with the above mentioned requirements in Eq. (B.5):

$$\frac{\partial J}{\partial \psi(t)} = 0 \Rightarrow i\frac{\partial \chi(t)}{\partial t} = \hat{H}\chi(t), \tag{B.9}$$

$$\frac{\partial J}{\partial \psi(T)} = 0 \Rightarrow \quad \chi(T) = \hat{O}\psi(T), \tag{B.10}$$

$$\frac{\partial J}{\partial \epsilon^*(t)} = 0 \Rightarrow \epsilon(t) = \frac{i}{\alpha_0}[\langle \chi_e(t)|\hat{\mu}|\psi_g(t)\rangle - \langle \psi_e(t)|\hat{\mu}|\chi_g(t)\rangle. \tag{B.11}$$

For a physically meaningful solution it is required that

$$\begin{aligned} i\hbar\frac{\partial \psi(t)}{\partial t} &= H\psi(t), \\ \psi(x,0) &= \psi_0(x). \end{aligned} \tag{B.12}$$

The Eq. (B.12) can also be obtained from the requirement that $\frac{\delta J}{\delta \psi(T)} = 0$.